Dynamics and Self-assembly of Single and Multi-component Polymeric Fluids: A Mesoscopic Computational Study

A Dissertation Presented for the

Doctor of Philosophy

Degree

The University of Tennessee, Knoxville

Mouge Mohagheghi
May 2016

Copyright © 2016 by Mouge Mohagheghi
All rights reserved.

Dedication

I would like to dedicate this dissertation to my supportive parents, especially my mother, Manijeh Firouzi who sacrificed so much to give me a better life.

Acknowledgements

I am greatly indebted to my advisor, Prof. Bamin Khomami, for his mentorship, timely advice, and support during my doctoral studies. His thoughtful comments and suggestions during our weekly meetings were extremely useful and enhanced my productivity. I truly appreciate his patience in teaching me the research fundamentals and inspiring courage, honesty, and cleverness in pursuing opportunities. I am thankful for his expert guidance in revising the manuscripts that I prepared during my research. Without his direction and time, the research achievements in this dissertation would not have been possible. He has been supportive of my career decisions, and his counsel was extremely informative and beneficial.

I extend my thanks to Prof. Mark Dadmun, Prof. Stephen Paddison, and Prof. Steven Abel for their acceptance to serve on my committee and their critical questions, comments, and support during the preparation of this dissertation. Also, I appreciate the staff of Chemical and Biomolecular Engineering Department - Rita Gray, Amy Brewer, Jennifer Wolfenbarger, Amber Tipton, and Deborah Liewellyn for their kind support. Special thanks to Dr. Dibyendu Mukherjee and Dr. Nansheng Liu for their thoughtful recommendations during the early stages of my graduate study.. I express my gratitude to my senior colleagues, Arash Abedijaberi, Mahdy Malekzadeh, Travis Russell, Bo Zhang, and my current officemates Hanieh Niroomand, Amir Saadat, Hadi Nafar, Tyler Bennett and Michelle Aranha, and post-doctoral researcher, Dr. Xianggui Ye for their support, cooperation in sharing computer resources, and contributing to a pleasant working atmosphere.

Special thanks to Gerald Ragghianti (system administrator of the Newton HPC cluster at the University of Tennessee, Knoxville) for his cooperation and technical assistance with parallel computing resources.

I gratefully acknowledge the financial support of my graduate studies at the University of Tennessee from NSF through grant EPS-1004083 and from the departmental first-year graduate fellowship.

I express my sincere thanks to my family and close friends for their love and constant support. They always encouraged me to achieve my goals, and were always next me whenever I needed help.

Abstract

The focus of this dissertation is on the development of computational models to elucidate the underlying physics of single- and multi- component polymeric fluids in equilibrium and non-equilibrium settings.

I have utilized a combination of a dissipative particle dynamics methodology and an entanglement network analysis algorithm, the so-called "Z1" code, to examine the relaxation mechanisms, their corresponding time scales and single chain dynamics of moderately entangled, linear, monodisperse polymer melts undergoing simple shear flow. In so doing, not only the fidelity of the DPD methodology for entangled polymeric melts at equilibrium and under flow has been examined for the first time, but also, the intricate relationship between single chain dynamics and chain relaxation mechanisms are elaborated. Specifically, it is shown that three main time scales, τ_R (Rouse), τ_d (disengagement), and τ_{rot} (rotation) are the dominant relaxation mechanisms at three distinct flow regimes.

In turn, the molecular origin of shear banding in unidirectional flow of entangled polymeric melts is investigated for the first time. It is revealed that the temporal evolution of shear banding is a very sensitive function of the time scale over which the deformation rate is imposed. It is demonstrated that the stress overshoot locally inhomogeneous chain deformation and thus spatially inhomogeneous chain disentanglement. Furthermore, the localized jump in entanglement density results in a considerable jump in first normal stress

and viscosity leading to the incipient shear banding. The stability of the incipient shear banded structures is studied via interfacial stability analyses.

Finally, we applied a 3D self-consistent-field theory simulations to determine the equilibrium morphologies formed by ABC triblock copolymer melts confined between two parallel plates. The main goal is the determination of conditions under which the perpendicular lamella and cylinder is stabilized; since these structures play a central role in many nanotechnology applications. To this end, the chain architecture, surface energy, and film thickness are varied to find the rational process conditions to stabilize the aforementioned morphologies. Specifically, it is shown that the perpendicular lamella and cylinder morphology is stabilized if both confined walls attract the middle block and the surface energy is large.

Table of Contents

Chapter 1 Introduction 1
1.1 Accurate Modeling of Highly Entangled Polymeric Flows 2
1.1.1 Shear Rate Dependent Viscosity 7
1.1.2 Relaxation Time Scales and Mechanisms 8
1.1.3 Flow-induced Chain Disentanglement 9
1.2 Flow Phenomenon: "Shear Banding" 9
1.2.1 Shear Banding 10
1.2.2 Stress Relaxation 11
1.2.3 Interfacial Stability of Viscoelastic Stratified Flows 11
1.3 Self-assembly of Block Copolymers 12
1.3.1 Macrophase and Microphase Separation 14
1.3.2 Phase Diagram 15
1.3.3 Confinement Effect 16

Chapter 2 Flow-Microstructure Coupling in Entangled Polymeric Melts 18
2.1 Introduction 18
2.2 Methodology 21
2.2.1 Polymer Chain Model 24
2.2.2 Topological constraint 24
2.2.3 Simulation Details and Units 28
2.3 Results and Discussions 30
2.3.1 Equilibrium Scaling 32
2.4 Simple Shear Flow 35
2.5 Conclusion 48

Chapter 3 Molecularly Universal Criterion for Shear Banding: Formation of Local Inhomogeneity Mechanism 50
3.1 Introduction 50
3.2 Background 52
3.3 Simulation Technique 57
3.4 Results and Discussion 57
3.4.1 Continuum Observation of Shear Banding Existence 58
3.4.2 Free - Energy Analysis 62
3.4.3 Molecularly based Criteria for Formation of Localized Inhomogeneity 63
3.4.4 Formation of Localized Inhomogeneity: Mathematical Description 66
3.4.5 Effect of Deformation Ramping Rate on Shear Banding Occurrence 69
3.5 Conclusion 74

Chapter 4 Molecular Processes Leading to shear Banding 76
4.1 Introduction..... 76
4.2 Local Process of Inhomogeneity Formation: Number of Entanglement Gradient . 77
4.3 Inhomogeneous Chain Deformation and Disentanglement 82
4.4 Stability of Shear Banded Structures 89

Chapter 5 Elucidating the Morphological Complexities of Linear Symmetric Triblock Polymer Thin Films 91
5.1 Introduction..... 91
5.2 Self-Consistent-Field theory 94
5.3 Parameter Selection 99
5.4 ABC Triblock Copolymer Bulk Phase Self-assembly..... 99
5.5 ABC Triblock Lamella Thin Film Morphology 102
5.5.1 AB diblock lamella Thin Film Morphology 103
5.5.2 Directed Self-assembly with Weak Surface Interaction 106
5.5.3 Directed Self-assembly with Strong Surface Interaction..... 109
5.6 ABC Tetragonal Cylinder Thin Film Morphology..... 112
5.6.1 Directed Self-assembly with Neutral Wall 115
5.6.2 Directed Self-assembly with Strong Surface Interaction..... 116
5.7 Conclusion 117

Chapter 6 Conclusions..... 118
6.1 Entangled Polymeric Flow Behavior and Shear Banding Mechanism..... 118
6.2 Block Copolymer Directed Self-assembly..... 123

List of References……...……**125**

Vita……..**138**

List of Tables

Table 2-1. The examined parameters at equilibrium for N=250. 28
Table 2-2. R_{min} and L_{max} at various *Wi* and Equilibrium with aij = 200 for N= 250. 28
Table 2-3. Simulation parameters and specifications. 30
Table 3-1.Calculated free energy curvatures at the origin and strain unit γ corresponding to stress overshoot as well as anisotropic fraction λ obtained from the area under the figure 3-6 curves for different step-strain simulations. Shear banding exists if equation-(3.2) becomes negative. 68
Table 3-2. Calculated free energy curvatures at the origin and strain unit γ corresponding to stress overshoot as well as anisotropic fraction λ obtained from the area under the figure 3-8 curves for different start-up simulations. Shear banding exists if equation-(3.2) becomes negative. 74
Table 4-1. Depth, elasticity and viscosity ratios between the slow and fast bands for different step-strain simulations. The ratios are defined as ε = dmore viscous /dless viscous , EL = N1more elastic/N1less elastic and R = ηmore viscous /ηless viscous. Results are consistent with interfacial stability analysis. 90
Table 5-1. Molecular Parameters for Prototypical Diblock Experiments.([a,b]Data taken from references 139 and 140, respectively.) 105
Table 5-2.Summary of parameters used for thin film SCFT calculations of AB diblocks. Effective film thicknesses (d) used for parallel and perpendicular orientations; correspond to optimal film thicknesses..... 105
Table 5-3. Molecular Parameters for Prototypical Triblock Experiments. ([a,b]Data taken from references 141 and 142, respectively.) 114

List of Figures

Figure 1-1. Schematic presentation of shear banding in unidirectional flow. 10
Figure 1-2. Bulk phase diagram of diblock copolymer melt [22]..... 16
Figure 2-1. (a) Radial distribution function in the case of N=250 at different amplitudes of conservative force, a. The arrow shows the distance rmin. (b) Probability distribution function of bond-length (L) for different values of a. The arrow shows L_{max}. 26
Figure 2-2. (a) Radial distribution function for N=250 at different *Wi*. The arrow shows the distance rmin. (b) Probability distribution function of bond-length (L) for different shear rates. The arrow shows L_{max}. In these simulations, aij = 200..... 27
Figure 2-3.Execution time vs number of beads per chain. The execution time is reported in second per DPD time unit, τ. The computational speedup as a function of number of cores is shown in the inset, demonstrating the performance improvement via strong parallelization..... 31
Figure 2-4. Predicted radius of gyration and longest relaxation time as a function of chain length at equilibrium. The radius of gyration shows the effective exponent of 0.5. The τ_{d0}/N^3 holds the scaling of 0.3 and the cross-over occurs at around N = 400 (Z_k =27). 32
Figure 2-5. Diffusion coefficient as a function of chain length. The proper scaling limit is reached and the values are reported in the DPD units. 36
Figure 2-6. Autocorrelation function of unit end-to-end vector vs time at different *Wi* along with their fits for N =250. The fit for *Wi* = 0.1 is the summation of three exponential and the ones for *Wi* = 30 follows the equation 2.8. The autocorrelation function for *Wi* =10000 is shown in the inset..... 38
Figure 2-7. The longest relaxation time of dense melts with N = 200, 250 and 400 beads/chain as a function of *Wi*……..38
Figure 2-8. The rotational timescale of dense melts with N = 200, 250 and 400 beads/chain as a function of *Wi*……..39
Figure 2-9. Ratios of the rotation to the disengagement times for the melt of entangled systems, N = 200, 250 and 400 beads/chain as a function of *Wi*……39
Figure 2-10. Average number of entanglements per chain as a function of *Wi* for different chain length, N = 200, 250 and 400 beads/chain……40
Figure 2-11. Average orientation angle vs *Wi* for different chain length, N = 200, 250 and 400 beads/chain……..41
Figure 2-12. Mean fractional extension as a function of Wi for different chain length, N= 200, 250 and 400 beads/chain…….……41
Figure 2-13. Chain orientation angle and fractional extensions a function of time for N =250 beads/chain at *Wi*=100……..43
Figure 2-14. (a) The Kuhn length normalized by its equilibrium value, b_0 as a function of *Wi*. (b) The chain end-to-end distance normalized by the equilibrium value as a function of *Wi*……....44
Figure 2-15. Tube diameter, a versus *Wi* calculated via formulae d = < L >/< Z_k > for N=250 and 400 beads/chain……...47

Figure 2-16. Steady shear stress as a function of Weissenburg number, *Wi*. Rouse time, τ_R is estimated via $\tau_d/\tau_R = 3\langle Z\rangle$. This figure appeared in a previous publication [113]. It has been also included to facilitate the discussion. 47
Figure 2-17. The probability distribution of magnitude of end-to-end vector vs Ree at various *Wi* values for N = 250 beads/chain……48
Figure 3-1. (a) Steady shear stress and (b) viscosity as a function of *Wi* for different chain length, i.e. N=250 and 400 beads per chain. Rouse relaxation time, τ_R is determined via $\tau_R = \tau_d/3Z$. This figure appeared in a previous publication [113]. It has been also included to facilitate the discussion. 59
Figure 3-2. Shear stress evolution as a function of strain for different chain length and *Wi*. No stress-overshoot emerges for *Wi*=1, N=250 shown in the inset. 60
Figure 3-3. Shear stress and velocity profile temporal evolution for (a) steady shear banding at *Wi*=30, N=250, (b) steady shear banding at *Wi*=40, N=400 and (c) transient shear banding at *Wi*=1000, N=400. Time is scaled by the disengagement time at the applied shear rate. This figure appeared in a previous publication [113]. It has been also included to facilitate the discussion……61
Figure 3-4. Free energy change per unit volume for different chain length and *Wi*..... 63
Figure 3-5. Configuration snapshots of a randomly chosen single chain at various incremental times at *Wi* = 40, N=400. 64
Figure 3-6. Primitive path segmental orientation distribution function at various *Wi* and chain length 68
Figure 3-7.(a) Shear stress evolution as a function of strain and velocity profiles at various strain units shown in the figure inset and (b) free energy vs strain for different ramp-time simulations. 72
Figure 3-8. Primitive path segmental orientation distribution at various ramp times 73
Figure 3-9. Average number of entanglements (a) as a function of time and (b) along the velocity gradient direction Y, at different ramp times. Y is scaled by the simulation box length, H. 73
Figure 4-1. (a) Stress and velocity profiles of step-strain at *Wi* = 30, (b) Step-strain entanglement distribution in X-Y plane, (c) Contour plot of number of entanglements at ramp-speed =20 τd. The dashed lines indicate the interface between the adjacent regions. $\Delta Z/\Delta Y > 3$ and < 2 for step strain and ramp-speed =20 τ_d. 80
Figure 4-2. Number of entanglement points in the X-Z plane in (a) lower region (future fast band) (b) middle region (future slow band) (c) upper region (future fast band).81
Figure 4-3. Plots of normalized chain end-to-end distance and orientation angle vs velocity gradient direction, Y for a) steady shear banding at *Wi*=30, N=250, b) steady shear banding at *Wi*=40, N=400 and c) transient shear banding at *Wi*=1000, N=400. L is the chain contour length and θ_0 is the orientation angle at equilibrium, i.e. 45°. 84
Figure 4-4. Average entanglement density as a function of velocity gradient direction, Y at various *Wi* and chain length. Y is normalized by the box side size, H. 85
Figure 4-5. (a−d) Entanglement probability distribution function at different times for *Wi* = 40, N=400. The red and dashed blue lines, respectively, show the regions of the flow that are eventually occupied by the slow and fast bands; $\Delta Z = \langle Z\rangle_{\text{slow band}} - \langle Z\rangle_{\text{fast band}}$. 87

Figure 4-6. Temporal evolution of first normal stress for (a) steady shear banding at Wi=30, N=250, (b) steady shear banding at *Wi*=40, N=400 and c) transient shear banding at *Wi*=1000, N=400. In the case of transient shear banding (c), the difference between the first normal stress in the slow and fast bands disappears at the steady state and hold its outmost value during the stress relaxation as shown by arrows. Time is normalized by the disengagement time at the applied shear rate……88
Figure 5-1. Bulk phase diagram of linear ABC triblock terpolymer melt as a function of middle block volume fraction and interaction parameters while keeping the end blocks' volume fractions identical, $f_A = f_C$. In the case $\chi_{AB}/\chi_{AC} = 1$, $\chi_{AB}N = \chi_{BC}N = \chi_{AC}N = 35$ and when $\chi_{AB}/\chi_{AC} = 3$, $\chi_{AB}N = \chi_{BC}N = 60$ and $\chi_{AC}N = 20$. The red, green and blue colors are assigned to A, B and C blocks, respectively……101
Figure 5-2. Equilibrium lamellar morphology of AB diblock copolymer melt confined between (a) two neutral substrates, (b) two homogenous surfaces: both surfaces prefer B segments, (c) Heterogeneous surfaces: bottom substrate favors B block while top surface is neutral to both blocks. A and B blocks are depicted by red and blue colors, respectively……..104
Figure 5-3. Excess free energy per unit area as a function of film thickness (d) for neutral wall. solid line: Perpendicular morphology, dashed curves: Parallel morphologies with 0.5, 1, 1.5,2 lamella layers from left to right respectively……108
Figure 5-4. Minimum energy difference (ε) vs. wall potential (|HB|)……..…108
Figure 5-5. Density profile of triblock films. (a) C|| morphology in which Red-blue domains represent A-C repeated morphology at d < 3.2 Rg, (b) Metastable C|| at larger film thicknesses, (c) Stable perpendicular morphology showing the presence of all three A-B-C components in the middle of the film, (d) Metastable PL with parallel configuration in the bulk, (e) density profile for the A segments (regions where CA > 0.7). A, B and C blocks are depicted by red, green and blue respectively……110
Figure 5-6. Excess free energy per unit area as a function of film thickness (d) for wall potential, HB= -20. solid curve: A and C blocks are present in the center of the film, dashed line: all three A-B-C blocks form perpendicular lamella in the center of the film……...111
Figure 5-7. Influence of confinement, surface field and film thickness on linear triblock terpolymer morphologies. Both walls attract the middle block B while the end blocks' volume fractions are identical, fA = fC and interaction parameters are the same, $\chi_{AB}N = \chi_{BC}N = \chi_{AC}N = 35$. The green rectangles demonstrate the metastable structures at certain film thicknesses……113
Figure 5-8. (a) Arrangement I: Cylinders represents minor A and C domains have elliptical cross sections. The system is translationally invariant in the y direction. n shows the number of layers in the z direction. In this arrangement; the same minor blocks (A or C) occupy the same row……..…114
Figure 5-8. (b) Arrangement II: Cylinders represents minor A and C domains have elliptical cross sections. The system is translationally invariant in the y direction. n shows the number of layers in the z direction. In this arrangement; both minor blocks (A and C) occupy the same row……114

Figure 5-9. Excess free energy per unit area as a function of film thickness (d) for the neutral wall. solid line: Perpendicular morphology, dashed curves: Parallel morphologies labeled with the number of layers and type of arrangement……..115
Figure 5-10. Excess free energy per unit area as a function of film thickness (d) for strong wall potential, HB= -35.0. solid line: Perpendicular morphology, dashed curves: Parallel morphologies labeled with the number of layers and type of arrangement……..116

Chapter 1

Introduction

Both experimental and theoretical research in fluid dynamics and rheology have played a significant role in the advancement of science, engineering, and their technological applications in the past several decades. Two broad classes of fluids: Newtonian and non-Newtonian liquids are of paramount interest to fluid dynamics researchers due to their wide applications in polymer processing industry, petroleum industry, food industry, and pharmaceutical industry, and in biological processes.

Non-Newtonian fluids, commonly classified as complex fluids (fluids whose microstructural evolution under a variety of flow situations is nontrivial) behave significantly different from simple fluids. For instance, non-Newtonian fluids have a shear-rate-dependent viscosity as opposed to the constant Newtonian viscosity. Examples include fiber suspension, gels, emulsions, colloids, surfactants, liquid crystalline polymers, and polymer liquids. In addition, many of the interesting flow phenomena that are absent in Newtonian flows such as rod-climbing, extrudate swell, tubeless siphon, and shear thickening occur in polymeric flows and have been discussed at length in different standard text books on the subject (Bird and Larson [1, 2]). The suggested common point in all of the related work is that the interesting behavior exhibited by complex fluids can be attributed to the intricate dependence of macroscopic rheological properties on the flow-induced microstructure evolution. Therefore, studying the non-linear flow-microstructure coupling and the corresponding macroscopic rheological response as well as

morphological development is vital to further develop a knowledge-based design and processing of complex fluids that determine the quality of the end product.

This dissertation focuses on three major parts:

1) To establish a comprehensive understanding of the rheological behavior of linear polymer chains in entangled polymeric melts at equilibrium and in unidirectional shear flow via Dissipative Particle Dynamics (DPD) method.

2) To investigate the molecular mechanism of shear banding, a non-linear flow phenomenon that occurs in high-molecular weight polymeric flows.

3) To provide process strategies to direct desired self-assemblies in nanolithography, namely perpendicular lamella and cylinders required by the semi-conductor industry via Self-Consistent-Field Theory (SCFT).

The progress toward these goals will be presented in the following chapters of this dissertation.

1.1 Accurate Modeling of Highly Entangled Polymeric Flows

As mentioned earlier, under external forces, the microstructure of a complex fluid significantly changes from its equilibrium configuration. This property allows one to tailor materials for specific applications. This is of particular interest to both the polymer processing industry and rheology community as well as to bio-related applications that are based on naturally occurring macromolecules, such as DNA, etc.

Polymers, in general, are large macromolecules composed of repeating structural units. Depending on the flow type (shear or extensional or a combination of both) and flow

strength, the polymer molecules stretch and orient and thereby undergo a large number of conformational changes. These conformational changes of the polymer chains/molecules within a fluid element at the microscopic level contribute on average to the macroscopic quantities such as the stress experienced by that fluid element under flow. Numerous experimental techniques have been used to determine the microstructural information of a molecule. Specifically, fluorescence video microscopy allows direct observation of molecular configuration changes in the flow. Optical methods such as birefringence and light scattering provide information about mean orientation and conformation of the molecules. Nuclear magnetic resonance (NMR) and neutron scattering methods provide information regarding the conformational distribution function.

In contrast to Newtonian fluids, the stress in polymeric fluids depends on the history of flow deformation and these fluids exhibit a spectrum of relaxation times. Hence, polymeric fluids are viscoelastic in nature with a fading memory. This means that once they are perturbed by flow from their original equilibrium configuration, they tend to relax to the original configuration. Thus, they are partly elastic and the time scale associated with the macromolecular configurational changes is closely related to the longest time constant in the relaxation spectrum, which corresponds to the polymeric chain end-to-end motion. Depending on the polymer concentration, these fluids can be classified into 3 categories – dilute solutions, concentrated solution, and melt. Dilute solutions find application in polymer-induced turbulent drag reduction, DNA separation, etc.. Concentrated solutions and melts are used in a variety of polymer processing operations such as coating, molding, extrusion, etc.

Polymer molecules move independently in dilute solutions, however in highly concentrated solutions and melts, their dynamics are inter-molecularly dependent due to the presence of "entanglement" (Entanglement is considered as the topological constraints from surrounding chains which restricts the polymer chain motion). It has proven to be a difficult challenge for rheologists to model the realistic motion of polymer chain and predict the flow rheological response in entangled fluids. Only very few molecular-based constitutive models describing the stress-strain relationship are currently available to allow one to perform continuum-level flow simulations under varied flow kinematic conditions. Therefore, accurate flow simulations are essential tools to model and predict the fluid rheological behavior correctly.

Continuum level models are frequently used, but are among the less descriptive computational methods to model polymeric fluids. These models are based on continuum mechanics, network (e.g., *Geisekus* model) and kinetic theories (e.g., *Oldroyd-B* model for dilute solution and *reptation* model for entangled melts and concentrated solutions). They are useful in qualitative prediction of the flow behavior, however, they are not perfect in quantitative prediction at high flow strength which typically occurs in processing settings. In what follows, we focus on the entangled polymeric melts dynamics.

The novel idea of reptation by de Gennes [3], that an entangled polymer chain experiences snake-like diffusion through contorted tubes formed by the surrounding chain-like molecules, was translated into an elegant theory (tube theory) and a corresponding constitutive equation by Doi and Edwards a decade later [4]. The original tube theory is largely in agreement with experiments on linear viscoelasticity; however, it demonstrated

certain discrepancies with experimental observations including excessive shear thinning, no overshoot in the first normal stress, and incorrect scalings of viscosity and stress relaxation moduli. Therefore, tube theory was extensively refined over the next three decades. Improvements included its prediction of experimental measurements where contour-length fluctuation, chain stretching, and convective constraint release (CCR) were incorporated into the original theory [5, 6]. Today Rolie–Poly [7], one of the most advanced tube-based theory models, is viewed as the most accurate description of entangled polymeric liquid micro-structural and dynamical response to external stimuli. This is despite the fact that several key concepts in the theory including the tube field, precise definition of an entanglement and its contribution to stress, and statistical behavior of the chain at different length scales, specifically, on the tube diameter length scale, remain open questions. Overall, the major problem associated with the above constitutive equations has been the use of a closure approximation and other approximations based on physical arguments to obtain a closed-form constitutive equation. Also, there is no exact analytic solution for the configurational probability distribution function in the kinetic theory models, thus making it impossible to accurately determine the interplay between the fluid microstructure and bulk flow behavior.

To overcome the limitation of continuum-level models, particle-based mesoscale flow simulations are primary candidates. They offer guideline and/or insights for better process control and design which result in improved product quality and cost-effective operations. They also allow the elucidation of the underlying mechanisms of several flow phenomena such as nucleation, shear banding, wall-slip, etc.. More importantly, they provide the

configurational probability distribution function which is absent in kinetic theory models, thus making it impossible to determine the interplay between the fluid microstructure and bulk flow behavior. Hence, developing memory and CPU efficient algorithms could pave the way to accurate predictions of flow phenomena and the underlying mechanisms. The most detailed description of polymer molecules is the atomistic level description, i.e., molecular dynamics (MD) simulation, which forms the lowest level of the multi-scale modeling pyramid. It is useful only for simulations of short time and length scales; thus, a tremendous amount of computational resources is required to model realistic polymers. In order to capture the larger scale phenomena while maintaining a computationally feasible scheme, coarse-grained modeling is a viable alternative. Following this approach, the polymer molecule can be modeled as a Kramers chain (freely jointed bead-rod chain) or bead spring chain where the spring force-law is derived based on a force-extension relationship at equilibrium. Brownian dynamics (BD) and DPD are coarse-grained simulation techniques that allow accurate prediction of the fluid microstructure and flow behavior correctly and are consistent with experimental observations. In a BD simulation, the solvent degrees of freedom are removed completely, but their effect is taken into account through long-range dynamic correlations in the stochastic displacements of the beads. BD allows accurate representation of polymer solution dynamics, however, the computational cost of exploiting such a method in highly entangled solutions should be considered. For colloidal suspensions, the advanced “accelerated BD” algorithm that utilizes the Ewald sum technique developed by Brady and co-workers [8, 9] scales as $O(NlogN)$ where N is the total number of particles in a simulation box. In other recent

studies, an efficient BD algorithm [10, 11] of a semi-dilute polymer solution demonstrated the CPU time scales as $O(N^{1.8})$ and at best as $O(NlogN)$. On the other hand, DPD scales linearly with system size, thus the simulation computational cost is considerably reduced. Specifically, DPD can be applied to polymer melt systems while the most efficient BD models have been developed for dilute and semi-dilute solutions. To this end, we have developed and applied parallel DPD to entangled linear polymer melt flows to investigate single chain dynamics, mechanisms involved in stress relaxation and flow-induced chain network dynamics. DPD is completely discussed in the following chapter and some of the major properties of the entangled fluids are briefly discussed in the following subsections.

1.1.1 Shear Rate Dependent Viscosity

As the shear rate is increased, the viscosity of certain type of fluids called pseudo-plastic (shear-thinning) fluids decreases, while it increases for another class of fluids dubbed dilatant or shear-thickening fluids; most polymeric fluids are shear thinning. The Shear-thinning property in polymeric melts is associated with the chain alignment in the direction of the flow streamlines, and this in turn reduces the friction between different layers. Examples of shear-thinning fluids include molten high density polyethylene, poly-acrylamide in water, etc. At low shear rates, the viscosity of viscoelastic fluids approaches a constant value, defined as zero shear viscosity. In general, viscosity η scales with the non-dimensional shear rate (Weissenburg number, Wi) as $Wi^{-\beta}$ (β is a positive value). When the power-law exponent magnitude becomes larger than 1, rapid shear thinning is observed.

In fact, this phenomenon leads to a non-monotonic shear stress versus shear rate flow curve. This non-linear behavior is completely discussed in Chapter 3.

1.1.2 Relaxation Time Scales and Mechanisms

Unlike dilute solutions where their dynamics can be described by the Rouse or Zimm model [12, 13] and the corresponding time scale of the chain motion is the Rouse time τ_R, the relaxation in the entangled polymeric fluids is more complicated. Thus, single molecule visualization experiments have been utilized to study relaxation mechanisms of individual chains in entangled polymeric fluids. Specifically, Robertson and Smith [14] have found three distinct time scales in their experiments. The shortest time scale corresponded to the Rouse time, the longest one was associated with the disengagement time of tube-based theories, and the intermediate time scale was speculated to be a second reptative process. The primary limitation of these experiments is that the small number of molecules can be effectively tracked. To date, only a few Non-Equilibrium Molecular Dynamics (NEMD) simulations [15, 16] of moderately entangled polyethylene liquids have shown the remarkable dynamical response at high strain rates, i.e. the existence of chain rotation and retraction cycles which gives rise to a characteristic time scale that is much larger than the reptation time scale of the liquid. In Chapter 2, we have thoroughly investigated the chain dynamics and it is shown that three major relaxation mechanisms and three distinct flow regimes exists.

1.1.3 Flow-induced Chain Disentanglement

Chain dynamics in concentrated solutions and melts is commonly compared to polymer dynamics in a fixed network. Though all the polymer chains move simultaneously, it can be argued based on the reptation concept that one-dimensional diffusion along the tube is the dominant mode of motion. That is an arbitrary test chain gradually disengages from the tube-like region around its backbone made by topological constraints. As shear rate increases, the number of entanglements per chain decreases. This is mainly due to the flow alignment of the chains as well as the onset of chain stretch. When the flow enters the nonlinear viscoelastic regime, the polymer liquid experiences a substantial decrease in the entanglement density, which leads to the occurrence of chain rotation/retraction cycle. The chain end-to-end probability distribution function widens with increasing shear rate, confirming the existence of large configurational diversity in viscoelastic fluids. The disentanglement behavior is fully discussed in Chapter 2.

1.2 Flow Phenomenon: "Shear Banding"

The broad and complicated relaxation spectrum in entangled polymeric fluids give rise to several interesting flow phenomena which are absent in Newtonian flows such as shear banding, wall-slip, rod-climbing, etc. [2, 17].

1.2.1 Shear Banding

In simple shear flow, fluid velocity is in one direction (e.g. x), and depends linearly on the coordinate in the orthogonal direction: $V_x = \dot{\gamma} y$. In this case $\dot{\gamma}$ is the shear rate, and this is considered to be one of the simplest rheology experiments to perform. The simple shear data are used routinely to calibrate and verify theories of polymer dynamics; including tube theories or constitutive equations derived from them. In practice, a simple shear is obtained in couette or cone-and-plate geometries (in the limit of small gap). However, generally there is no guarantee that the liquid will flow with a uniform velocity profile—sometimes it can shear band, i.e., separate into fast and slow flowing regions (large and small shear rates, respectively) as shown in Figure 1-1. In Chapters 3 and 4 of this dissertation, the molecular origin and mechanism leading to shear banding is discussed. Two primary concepts related to the formation of shear banded structures are elucidated in the following subsections.

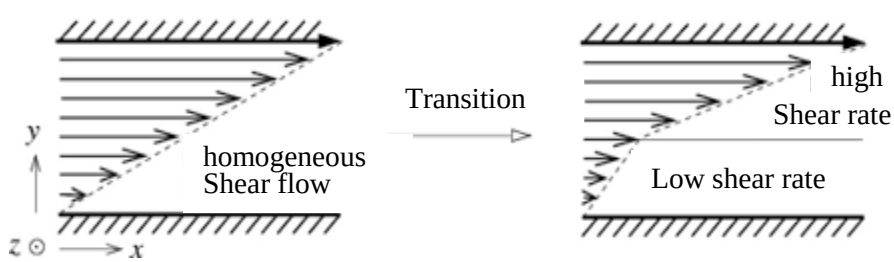

Figure 1-1. Schematic presentation of shear banding in unidirectional flow.

1.2.2 Stress Relaxation

Unlike Newtonian liquids, stress relaxation is a common occurrence in viscoelastic liquids. Upon start-up or step-strain experiments, above a critical shear rate, stress-overshoot appears due to the affine deformation of the chains at strains around 2. Prior to the stress-overshoot, chains are stretched and oriented with respect to the flow direction. In turn, the stresses (shear stress and first normal stress) in the viscoelastic fluids start to decay until shear viscosity and normal stress attain a steady value. This is due to the previously mentioned fading memory-like behavior that determines the viscoelastic property of the polymeric fluids. The decay time is comparable to the material relaxation time. Moreover, the polymer chains mainly relax their stress in two steps; in the first step, tension is relaxed by segmental stretch relaxation, a very fast process; and in the second step, chains relax their orientation.

1.2.3 Interfacial Stability of Viscoelastic Stratified Flows

Superposed layers of viscoelastic fluids flowing down an inclined plane or in pressure or drag driven channels are prone to interfacial instability even in the limit of zero Reynolds number (Re). Interfacial instabilities manifest themselves in the form of long, intermediate, and short-wavelength travelling waves at the interface of adjacent layers. These interfacial waves are similar in nature to surface waves on a body of water. They can occur at vanishingly small Reynolds numbers and are due to viscosity, density, and elasticity

differences in the respective layers. In the limit of vanishing Re and negligible interfacial tension, the parameter space that determines the interfacial stability of stratified flows consists of viscosity, elasticity and depth ratio (the ratio between the height of more viscous to less viscous layer). Specifically, in this class of flows two general roles exist: [18-21] (1) when the less viscous fluid is thin compared to the more viscous fluid, the interface is stable, i.e. the so-called "thin layer effect" [20]; and (2) when the more elastic layer is the majority component, elasticity stratification is stabilizing [18]. Therefore, one has to determine the relative importance of viscosity and elasticity stratification on the overall stability of the interface. If the interface is stable with respect to interfacial perturbations, then a smooth multilayer flow will coexist. Otherwise, perturbations grow leading to interfacial mixing and generally loss of desired properties.

1.3 Self-assembly of Block Copolymers

Polymers formed by linking together N monomers of one chemical type are referred to as homopolymers, where N is the polymerization index or degree of polymerization. A polymer that is produced by linking two or more chemically distinct monomers is referred to as a copolymer. For example, SBR (styrene-butadiene rubber) is an important synthetic rubber material that is produced by a mixture of styrene monomers and 1,3-butadiene monomers. Such polymers are classified as random or statistical copolymer because there is a statistical distribution associated with the sequence of styrene and butadiene monomers incorporated into the polymer chain. A second important type of copolymer is a block

polymer (BP) in which monomers of a given type are grouped into polymerized sequences or “block”, along a polymer chain such as $[PS\text{-}P2VP\text{-}PEO]_3$ (poly (styrene-2vinylpyridine-ethylene oxide).

Generally, size and shape of domains and the overall morphology of BPs can be controlled by judiciously manipulating the molecular weight and composition of the blocks. To this end, BPs with length scales ranging from 5–100 nm [22] allow the creation of well-controlled nanostructures that can target a wide range of applications—from nanofabrication [23-26] to membranes [27-29] to photonic crystals [30-32] and organic photovoltaics.

Among the plethora of BP applications, one that is rapidly approaching commercialization is microelectronic manufacturing. Traditional optical nanolithography with 30 nm feature size, cannot meet the growing demand for smaller feature sizes with increased surface/volume ratio. This technology gap is driving the need for a viable alternative. Highly controllable, uniform, and inexpensive templates based on block copolymers (BCPs) present such an alternative [33]. Moreover, there is a similar impetus in the magnetic recording industry to make smaller, denser, and more regular patterns leading to enhanced quality with increased information storage density.

An impressive array of experimental research [34-37], including pioneering studies by Nealey [38-40] and Ross et al.[41, 42], has shown that directed self-assembly techniques can be used to create the required morphologies with long-range lateral order for microelectronic and magnetic recording applications. Specifically, external fields such as electric and hydrodynamic, patterned substrates, and confinement, as well as epitaxy and

solvent annealing, have been successfully used to manipulate the size and orientation of nanodomains [43-51].

In addition, rational design of self-assembled structures considering the large parameter space involved with BP thin films is a critical step in translating bench-top synthesis protocols to large-scale fabrication techniques. To this end, simulation tools such as SCFT, Monte Carlo (MC) simulations and DPD have been extensively used to examine bulk morphology development as a function of individual block properties, i.e., to examine a morphology phase diagram.

1.3.1 Macrophase and Microphase Separation

When two homopolymers, e.g. A and B, are blended in the melt state or cast from common solvent, their chemical differences are normally sufficient to induce a liquid-liquid phase separation. This is a macrophase separation because, given sufficient time, the emerging A-rich and B-rich phases will coarsen to macroscopic length scales. The driving force for the phase coarsening is the interfacial free energy associated with the interfaces separating two phases. In contrast to a blend of two homopolymers, a pure molten block copolymer fluid such as AB diblock copolymer or ABC triblock copolymer cannot exhibit macrophase separation. Such a fluid is a one component system in which the chemical bonds linking dissimilar blocks prevent A and B segments of the same copolymer from being separated over macroscopic distances. However, in such fluids an ordering phenomenon known as microphase separation is possible. At a local ~ 1nm level, the

dissimilar blocks in a copolymer melt are driven to phase separate by the same microscopic interactions that produce macrophase separation in an A-B homopolymer alloy. However, unlike the homopolymer blend, A-rich and B-rich domains created by local phase separation of a copolymer melt cannot coarsen to length scales exceeding the extended chain length of a copolymer, ~ 100-1000 nm, since this would cleave the bonds connecting the blocks. Thus, BCPs segregate into microphases.

1.3.2 Phase Diagram

As with any thermodynamic system, there is a competition between entropy and enthalpy, which derives the minimization of a free energy. At high temperatures when entropy dominates, the polymer melt is highly disordered and the distribution of A and B even fluctuates around mean zero. Below a certain transition temperature the polymer melt orders. The ordering results in the formation of a periodic distribution of A and B blocks (for example in the case of AB diblock copolymer), and many exotic geometries have been observed in experiments. Below the transition temperature, however, the monomer segments will segregate and form regular, periodic structures. That is, the A and B segments of each copolymer chain will come together and display macroscopic order. Some of the common shapes that have been observed experimentally are lines (lamellar), hexagonal cylinders, and stacked balls (body centered cubic, BCC). Each geometry possesses different physical characteristics, and thus the ability to readily switch between the phases could allow fabrication of materials with tunable properties. The various phases

of a block copolymer melt can be succinctly described by a phase diagram. The two parameters that define the phase diagram in the case of AB diblocks are the Flory parameter, which is a measure of the strength of interactions between monomers (alike and different) and the bulk volume fraction of monomer A. The typical phase diagram for diblock copolymer melt is shown in Figure 1-2.

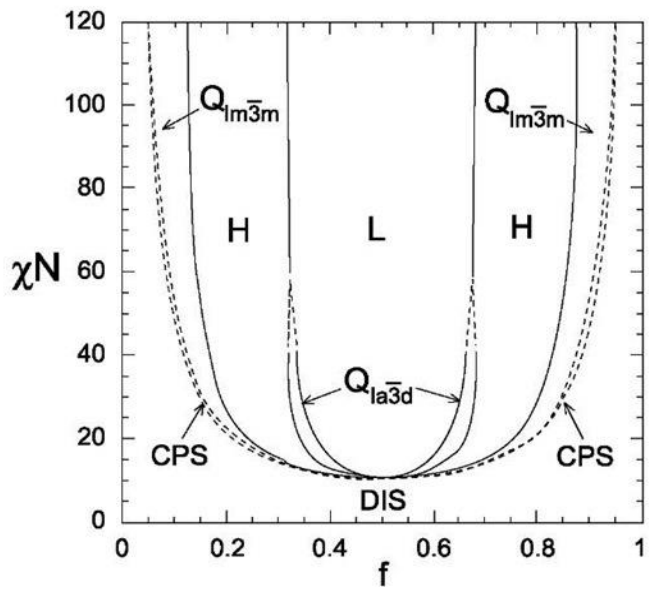

Figure 1-2. Bulk phase diagram of diblock copolymer melt [22].

1.3.3 Confinement Effect

One of the techniques to direct the block copolymer self-assembly is to confine the block copolymer solution or melt. In general, the geometrical constraint induces enthalpic (interaction with surface) and entropic (the block segments can either bridge or loop or exhibit a mixture of both) effects. Examples include the regular patterns formed by BCPs used in optoelectronics device fabrication when the BCP solution is spun cast on the

substrate or in chip fabrication while the BCP is confined in a well. Film thickness and surface chemistry both influence the morphology as well as its orientation. The confinement effect is fully studied in Chapters 4 and 5.

Chapter 2

Flow-Microstructure Coupling in Entangled Polymeric Melts

This Chapter is based on the submitted manuscript.

"Elucidating the Flow-Microstructure Coupling in Highly Entangled Polymer Melts: Part I. Single Chain Dynamics in Shear Flows," M. Mohagheghi and B. Khomami, *Journal of Rheology*, Revision submitted on 26-Feb-2016, JOR-15-280R.

2.1 Introduction

Accurate modeling and simulation of flow-microstructure coupling in entangled polymeric fluids is of great interest to many fields of science and engineering. Despite decades of investigation, a number of uncertainties regarding the essential physics required to make hi-fidelity predictions of flow dynamics in this class of fluids still exist. In fact, quantitative description of fast flows of entangled polymeric fluids even in relatively simple flow kinematics has proven to be a difficult challenge for rheologists.

The basic foundation for modeling of entangled polymer melts originates from an idea proposed by de Gennes [3], that an entangled polymer chain experiences snake-like diffusion through contorted tubes formed by the surrounding chain-like molecules. The physical constraints of these tubes mandate that chain motion parallel to the polymer backbone be greater than the motion perpendicular to it. This novel physical picture was translated into an elegant theory and a corresponding constitutive equation by Doi and

Edwards a decade later [4]. The original tube theory predictions are largely in agreement with experiments in the linear viscoelastic regime, however, at intermediate to high strain rates, a number of important discrepancies exist with experimental observations and theoretical predictions in unidirectional shear flow. These include excessive shear thinning, no overshoot in first normal stress, and incorrect scaling of viscosity and stress relaxation moduli with molecular weight. The failure of the original Doi-Edwards model to quantitatively describe the fluid response at high strain rates is mainly due to the fact that all of the relevant physical processes have not been self-consistently included in the constitutive equation. Therefore, tube theory based models of entangled polymeric fluids have been extensively refined over the past three decades to improve their prediction of rheological measurements particularly at high strain rates, i.e., contour-length fluctuation and CCR have been incorporated into the original "tube theory" —see Ref. [5, 52] for a current state of the art of reptation theory based models.

Despite tube theory's notable success, several key concepts including the tube field, precise definition of an entanglement and its contribution to stress remain open questions. To this end, single molecule visualization experiments have been utilized to study relaxation mechanisms of individual chains in entangled polymeric fluids. Specifically, Robertson and Smith [14] used optical tweezers to measure the intermolecular forces acting on a single DNA chain by the surrounding entangled molecules, and found three distinct timescales: the short timescale was determined as close to the theoretical value of the Rouse time, the long timescale was associated with the disengagement time of reptation theory,

and the intermediate timescale was speculated to be a second reptative process that was correlated with the dynamics of the effective reptation of tube under shear.

Despite the numerous successes of single-chain microscopy to date, experimentation alone cannot resolve all of the outstanding issues that perplex rheologists at high *Wi*. The primary limitation of these experiments is the small number of molecules that can be effectively tracked simultaneously, which is especially true of dense polymer melts. Atomistic or coarse-grained mesoscopic simulation of entangled polymeric liquids offers a complementary perspective of individual chain dynamics under flow. In particular, slip-link simulations [53, 54] with full-chain spatial coupling have been successful in accurately predicting the linear and nonlinear shear rheology as well as single-chain dynamics of fluids composed of entangled polymeric chains. However, the accuracy of the predictions, particularly for very fast flows, strongly depends on the assumed constraint renewal/release frequency. Moreover, recent atomistic NEMD simulations [15, 16] of moderately-entangled polyethylene liquids have shown that a remarkable dynamical response occurs at high strain rates in shear flows; i.e., the polymeric liquid experiences a dramatic decrease in the number of chain entanglements, which leads to a network of highly-stretched chains that form effective tube-like structures through which neighboring chains experience anisotropic diffusion. This ultimately leads to chain rotation and retraction cycles, which give rise to characteristic timescales that are much longer than the reptation time of the liquid.

Motivated by these exciting new findings particularly in regard to existence and magnitude of a third scale, we have performed detailed analysis of flow-microstructure

coupling in planar Couette flow of monodisperse entangled polymer melts with equilibrium entanglement densities of 13, 17 and 27 via DPD simulations. The main objective of this study is twofold: 1) to demonstrate the fidelity and computational efficiency of DPD in simulating flow of entangled polymeric melts, and 2) to elucidate the intricate coupling between single chain dynamics and relaxation mechanisms, i.e., distinct time scales, in shear flows of entangled polymeric fluids.

2.2 Methodology

DPD is a general mesoscopic simulation method, wherein the fluid is represented by a set of discrete coarse-grained particles that carry momentum and move according to Newton's law of motion. Hoogerbrugge and Koelman [55] originally developed DPD as a generalization of lattice gas automata method for the simulation of fluid motion. In their DPD algorithm, all particles were allowed to move freely and all particle-particle interactions were taken into consideration to ensure conservation of momentum and mass. On the other hand, energy is not conserved in DPD, thus this technique is generally used to simulate isothermal conditions. Also in the first generation DPD algorithms, a clear connection between the system temperature and model parameters was not established. This shortcoming was remedied by Espanol and Warren [56] who derived the Fokker-Planck equation that corresponded to the original DPD equations [55]. Specifically, the equilibrium solution of the aforementioned Fokker-Planck equation was used to demonstrate that the Gibbs canonical ensemble is realized only through proper enforcement

of the fluctuation-dissipation theorem. This in turn resulted in a clear description of temperature (see below for more detail).

For polymeric liquids, the thermodynamic and hydrodynamics interaction of a polymer chain with its surrounding is explicitly accounted for via a detailed force balance on each particle in the chain. Specifically, the fluid is represented by a set of N particles of mass m located in a 3D periodic simulation box. These coarse-grained particles interact with each other within a cut-off distance r_c, through conservative F^C, random F^R, and dissipative F^D forces.

The conservative force is independent of dissipative and random forces and it takes the form,

$$\begin{cases} F_{ij}^{C} = a_{ij}\left(1-\dfrac{r_{ij}}{r_c}\right)\vec{e}_{ij} & , \ r_{ij} \le r_c \\ 0 & , \ r_{ij} > r_c \end{cases} \tag{2.1}$$

where $\vec{r}_{ij} = \vec{r}_i - \vec{r}_j$, $\left|\vec{r}_{ij}\right| = r_{ij}$, $\vec{e}_{ij} = \vec{r}_{ij}/r_{ij}$. The variable a_{ij} describes the repulsion between particles i and j, and thus produces excluded volume interactions. The dissipative and random forces are expressed as,

$$F_{ij}^{D} = -\gamma\omega^{D}\left(r_{ij}\right)\left(\vec{v}_{ij}.\vec{e}_{ij}\right)\vec{e}_{ij} \quad , \quad F_{ij}^{R} = \sigma\zeta_{ij}\omega^{R}\left(r_{ij}\right)\vec{e}_{ij} \tag{2.2}$$

with γ and σ the friction parameter and amplitude of thermal noise, respectively. $\vec{v}_{ij} = \vec{v}_i - \vec{v}_j$, $\zeta_{ij}(t)$ is a Gaussian random variable with $< \zeta_{ij}(t) > = 0$ and $< \zeta_{ij}(t)\, \zeta_{kl}(t') > = (\delta_{ik}\, \delta_{jl} + \delta_{il}\, \delta_{jk})\, \delta(t-t')$; ω^D and ω^R are weighting functions. Evidently, the dissipative force slows particles by decreasing their kinetic energy. This decrease is in turn compensated by the

random forces that arises as a consequence of thermal fluctuations. Hence, the force parameters are related as shown below.

$$\sigma^2 = 2\gamma k_B \mathrm{T} \qquad , \qquad \omega^{\mathrm{D}} = (\omega^{\mathrm{R}})^2 \tag{2.3}$$

Where $\omega^{\mathrm{R}} = (1 - \frac{\mathrm{r_{ij}}}{\mathrm{r_c}})$, has the same functionality as the conservative force weighting function.

The Velocity-Verlet algorithm [57] is used to advance particle positions and velocities in time. Specifically,

$$\mathrm{r_i}(\mathrm{t} + \Delta\mathrm{t}) = \mathrm{r_i}(\mathrm{t}) + \Delta\mathrm{t}\mathrm{V_i}(\mathrm{t}) + \frac{1}{2}(\Delta\mathrm{t})^2\mathrm{f_i}(\mathrm{t}),$$

$$\widetilde{\mathrm{V}}_{\mathrm{i}}(\mathrm{t} + \Delta\mathrm{t}) = \mathrm{V_i}(\mathrm{t}) + \lambda\Delta\mathrm{t}\mathrm{f_i}(\mathrm{t}),$$

$$\mathrm{f_i}(\mathrm{t} + \Delta\mathrm{t}) = \mathrm{f_i}\big(\mathrm{r}(\mathrm{t} + \Delta\mathrm{t}), \tilde{\mathrm{v}}(\mathrm{t} + \Delta\mathrm{t})\big),$$

$$\mathrm{V_i}(\mathrm{t} + \Delta\mathrm{t}) = \mathrm{V_i}(\mathrm{t}) + \tfrac{1}{2}\Delta\mathrm{t}\big(\mathrm{f_i}(\mathrm{t}) + \mathrm{f_i}(\mathrm{t} + \Delta\mathrm{t})\big). \tag{2.4}$$

The adjustable parameter λ is used in the second step of the algorithm to predict the mid-step velocity $\tilde{\mathrm{v}}$ and the actual velocity is corrected afterwards in the last step. In this algorithm (compared to Euler-type approach used in DPD), the force is still updated once per iteration (after the second step), thus there is virtually no increase in computational cost while stability and accuracy are enhanced. All physical measurements that depend on coordinate differences are also taken after the second step; the temperature is measured after the last step. Motivated by the original Verlet algorithm [57], we have chosen $\lambda = 0.5$. This parameter choice allows for good control of the system temperature, i.e., temperature deviation from its specified value is < 3% with the noise amplitude $\sigma = 3$ and $\Delta t = 0.012$.

2.2.1 Polymer Chain Model

The beads of a linear polymer chain are connected via harmonic springs $\overrightarrow{F_i^S} = \sum_j k(r_{eq} - r_{ij})\overrightarrow{e_{ij}}$, i.e., where the sum is performed for all particles j to which particle i is connected. r_{eq} is the equilibrium bond length and is chosen to correspond closely to the first maximum of the radial distribution function. The spring constant $k=2a_{ij}$, is set in order to satisfy the topological constraint explained in detail in the next section. Moreover, a small bending potential [58] was added between three consecutive beads to increase the entanglement density. The bending potential is taken as $U_{bend} = K_b\,(1 + \cos\theta)$. The bending constant $K_b = 2.0$ and θ is the angle between the three consecutive beads. This type of potential results in an attractive force between the neighboring beads and a repulsive force between beads with distance 2 along the backbone.

2.2.2 Topological constraint

Chain crossings must be prevented in the entangled systems to ensure topological constraints are met. There are three predominant methods for enforcing this constraint in mesoscopic simulations. Specifically, Kumar and Larson [59] prevented the passage of two springs through each other by incorporating a spring-spring repulsion force into BD simulations of flexible polymers, thus the topological integrity of polymer molecules were maintained. Padding and Briels [60] introduced the uncrossability constraint through the TWENTANGLEMENT calculations into a coarse-grained DPD model to avoid unphysical bond crossings. The central idea of TWENTANGLEMENT algorithm is to consider the

bonds as elastic bands which can get entangled, the bond crossing or 'entanglement' is being explicitly detected via a geometrical examination. Thereafter, bond crossing is prevented by introducing an attractive force between the connected beads pushing back the entangled bonds to their respective sides. It is also possible to prevent chain crossing by tuning the conservative force and enforcing a simple geometric constraint. This computationally efficient and highly accurate method was developed by Nikunen et al. [61] and verified at equilibrium. Specifically, they have shown that if the geometric constraint,

$$\sqrt{2}\, r_{min} > L_{max} \tag{2.5}$$

is satisfied, bonds cannot cross each other. r_{min} and L_{max} refer respectively to the diameter of each bead and the longest distance between the center of mass of connected beads. The aforementioned geometrical condition can be met if a proper level of coarse graining is complemented by a reasonable description of bond stretching (choice of spring constant, k).

We have used the methodology of Nikunen et al. [61] at both equilibrium and under simple shear flow. First, we demonstrate the effect of a_{ij} and k on Eq. (2.5) at equilibrium in Figure 2-1 and report the r_{min} and L_{max} values in Table 2-1, the a_{ij} and the spring constant are varied while keeping the ratio constant, $k/a_{ij} = 2$. Our results are consistent with Nikunen at al.. Secondly, we investigate the flow effect on r_{min} and L_{max} values with a_{ij} = 200 and k = 400. The summary r_{min} and L_{max} values as a function of *Wi* are shown in Table 2-2 in DPD units. Moreover, r_{min} and L_{max} are taken respectively from the radial distribution function and bond-length distribution as labeled in Figure 2-1 and 2-2.

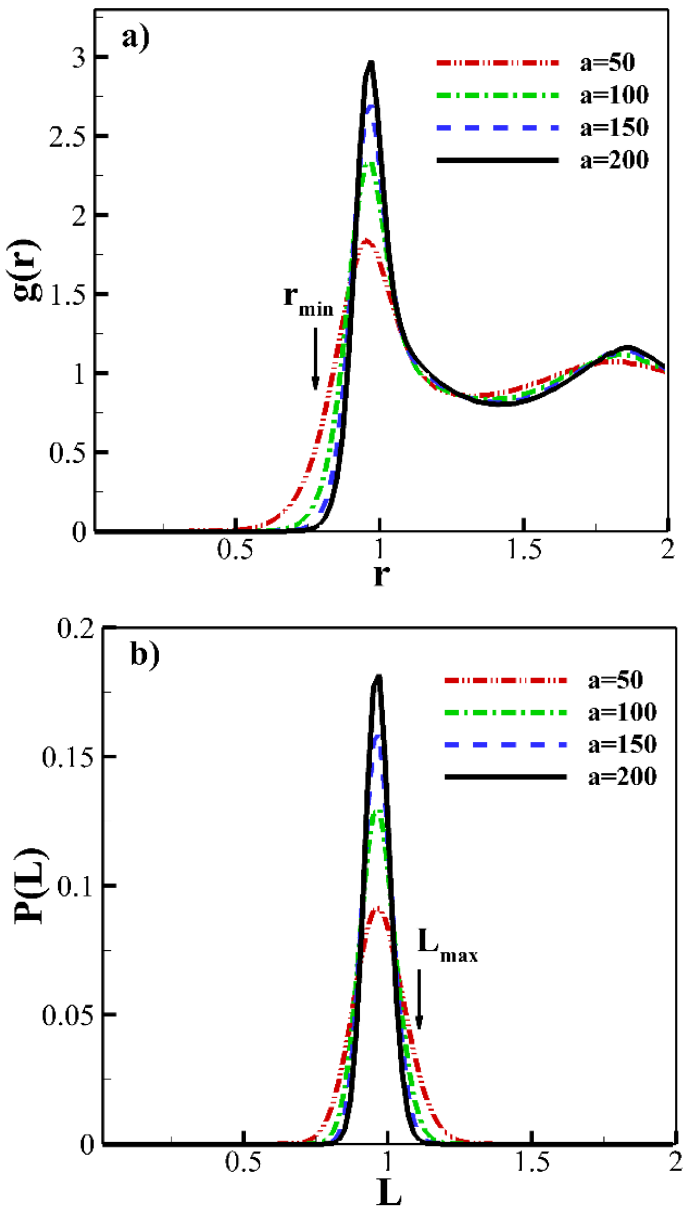

Figure 2-1. (a) Radial distribution function in the case of N = 250 at different amplitudes of conservative force, a. The arrow shows the distance r_{min}. (b) Probability distribution function of bond-length (L) for different values of a. The arrow shows L_{max}.

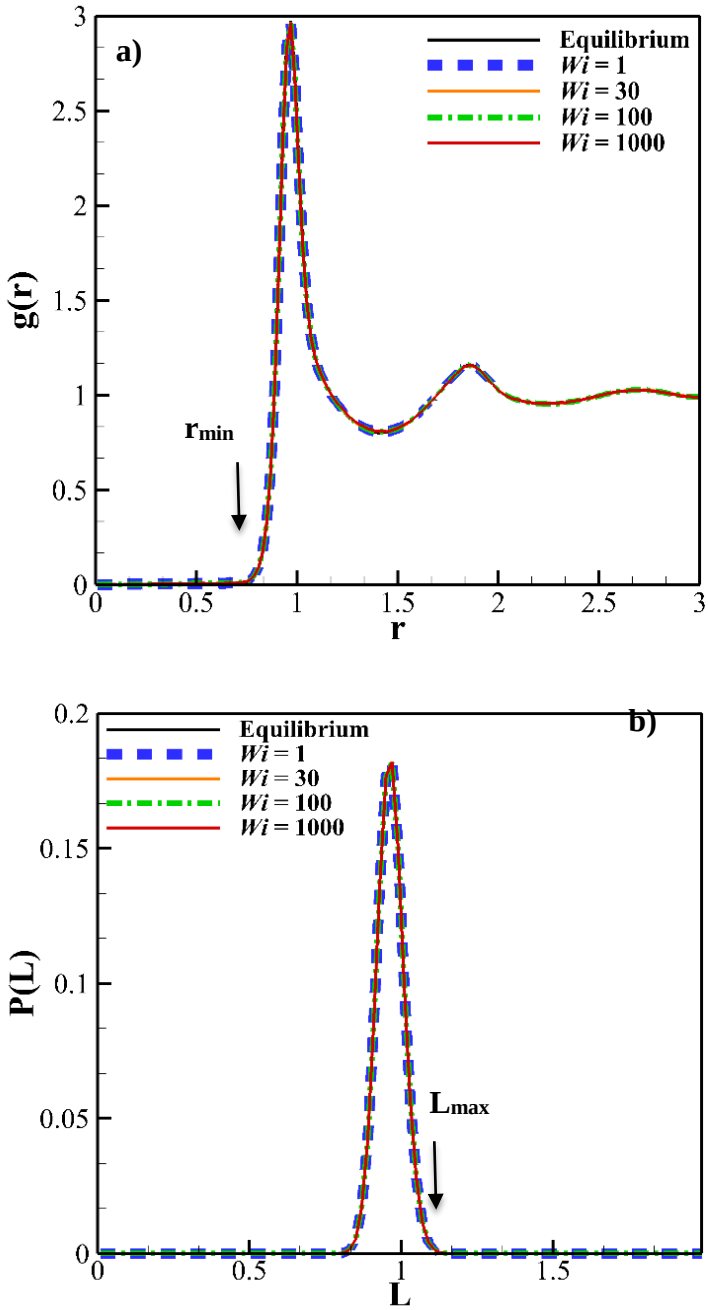

Figure 2-2. (a) Radial distribution function for N = 250 at different *Wi*. The arrow shows the distance r_{min}. (b) Probability distribution function of bond-length (L) for different shear rates. The arrow shows L_{max}. In these simulations, aij = 200.

Table 2-1. The examined parameters at equilibrium for N=250.

a	**50**	**100**	**150**	**200**
k	100	200	300	400
$\mathbf{r_{min}}$	0.58	0.69	0.75	0.771
$\mathbf{L_{max}}$	1.11	1.07	1.062	1.05

Table 2-2. r_{min} and L_{max} at various *Wi* and Equilibrium with aij = 200 for N= 250.

Wi	**Equilibrium**	**1**	**30**	**100**	**1000**
$\mathbf{r_{min}}$	0.771	0.77	0.77	0.77	0.76
$\mathbf{L_{max}}$	1.05	1.05	1.05	1.05	1.054

It should be mentioned that we chose an operative criterion over which r_{min} and L_{max} values are determined. The operative criterion for both equilibrium and non-equilibrium settings in our calculations is 3%.

2.2.3 Simulation Details and Units

Mass m, length r_c are chosen as the base units and are set to one. Rather than specifying the time unit, as Groot [62] and Hoogerbrugge [55], we have chosen to work with energy units such that $k_BT = 1$.

The aforementioned DPD simulation algorithm has been used to study entangled polymeric melts at equilibrium and in planar Couette flow in conjunction with Lees-Edwards boundary condition. The fidelity of DPD in predicting correct behavior and scaling at equilibrium and under shear flow is examined first. In turn, the flow-

microstructure coupling of entangled polymeric fluids is extensively studied with a particular focus on single chain dynamics and relaxation mechanisms. Specifically, we have focused our attention on moderately entangled systems, i.e., N = 200, 250 and 400 beads per chain with 1250, 705 and 1374 chains respectively in a canonical ensemble (NVT). The corresponding average entanglement densities at equilibrium for the aforementioned systems are: $<Z_k>$ = 13 (N=200), 17 (N=250) and 27 (N=400). Entanglement or topological constraint made by surrounding chains is considered here as the persistent contact between the primitive paths of neighboring chains. It should be noted that the entanglement network analysis was carried out using the Z1 code developed by Kröger et al. [63-65].We have focused our attention on these entanglements densities as they are close to the lower range of experimental entanglement densities.

Various simulation box sizes were used to avoid box size artifact and to study the effect of finite box size on the flow-microstructure coupling. However, most of the results reported in this thesis are from a simulation box with an aspect ratio of 2:1:1 with a larger dimension in the flow direction, *x*. Normal dimensions to the flow direction are twice the average equilibrium chain end-to-end distance; this box size is sufficient to avoid box size effect. The Velocity-Verlet algorithm [57] is used to integrate the equations of motion and the stress tensor is calculated based on the generalized formulation developed by Thompson et al. [66] where many-body potential is also considered in the stress equation. To achieve steady state velocities, shear and first normal stresses, simulations up to 10 times the disengagement time of the system have been performed. Considering the large size of the simulation box, accurate temporal ensemble averages were obtained over 0.1 τ_d.

In what follows, the disengagement time of the system, at equilibrium as well as under flow conditions are shown respectively as τ_{d0} and τ_d. The force parameter amplitudes as well as other DPD simulation specifications are summarized in Table 2-3.

Table 2-3. Simulation parameters and specifications.

Quantity	Value	Unit
Δt	0.012	$\sqrt{mr_c^2/kT}$
a	200.0	kT/r_c
σ	3.0	$(kT^3m/r_c^2)^{1/4}$
γ	4.5	$(mkT/r_c^2)^{1/2}$
ρ	1.0	r_c^{-3}
k (spring constant)	400.0	kT/r_c^2
V (N=200) : box volume	100.0 × 50.0 × 50.0	r_c^3
V (N=250) : box volume	100.0 × 42.0 × 42.0	r_c^3
V (N=400) : box volume	130.0 × 65.0 × 65.0	r_c^3

2.3 Results and Discussions

Although DPD has been used to simulate entangled polymeric fluids, its application has been limited to equilibrium settings. To this end, the first goal of this chapter is to demonstrate the fidelity and computational efficiency of DPD in modeling flow of entangled polymeric melts. Henceforth, the chains response to the flow, the intricate flow-microstructure coupling and existing characteristic time scales are extensively examined.

The execution time of DPD algorithm (wall-time) is demonstrated in Figure 2-3 as a function of number of beads per chain. The tests were performed on an "intel Xeon E5530" in a cube box with sides equal to twice the chain end to end distance, i.e $L = 2R_{ee} = 2bN^{1/2}$. The execution time is expressed in unit of s/τ and scales as $N^{1.4941.}$ The scaling is consistent

with a particle based model. The execution time should scale linearly with the total number of particles in the box while the number density is kept the same. Hence CPU-time increases with time ~ L^3 ~ $N^{1.5}$. This scaling is commonly observed in NEMD and DPD simulations, however, in our implementation, DPD calculations are at least order of magnitude faster than NEMD simulations (the comparison between the two methods is based on NEMD simulations of an entangled polyethylene melt, i.e., $C_{700}H_{1402}$). Moreover, the computational speedup gained from parallelization is shown in the inset of Figure 2-3 for N=250. It is clear that the performance improvement made by MPI (Message Passing Interface) programming makes the simulation times manageable.

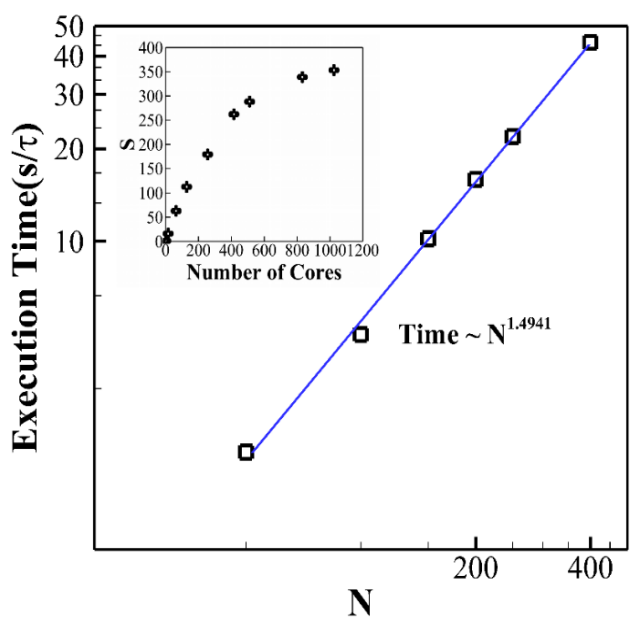

Figure 2-3.Execution time vs number of beads per chain. The execution time is reported in second per DPD time unit, τ. The computational speedup as a function of number of cores is shown in the inset, demonstrating the performance improvement via strong parallelization.

2.3.1 Equilibrium Scaling

Here, we briefly report the result of equilibrium simulations of entangled polymer melts and in turn compare them with reptation theory, as well as, existing simulation results and experimental observations.

Radius of Gyration: It is defined as $R_g^2 = \frac{1}{N}\sum_{i=1}^{N}(\vec{r}_i - \vec{r}_{cm})^2$, where $\vec{r}_{cm} = \frac{1}{N}\sum_{i=1}^{N}\vec{r}_i$. In a polymer melt, one would expect $< R_g > \alpha\ N^{1/2}$. As shown in Figure 2-4, the proper scaling behavior is reproduced. Previous studies using both realistic soft potentials [67] and hard potentials exhibit the same scaling [68].

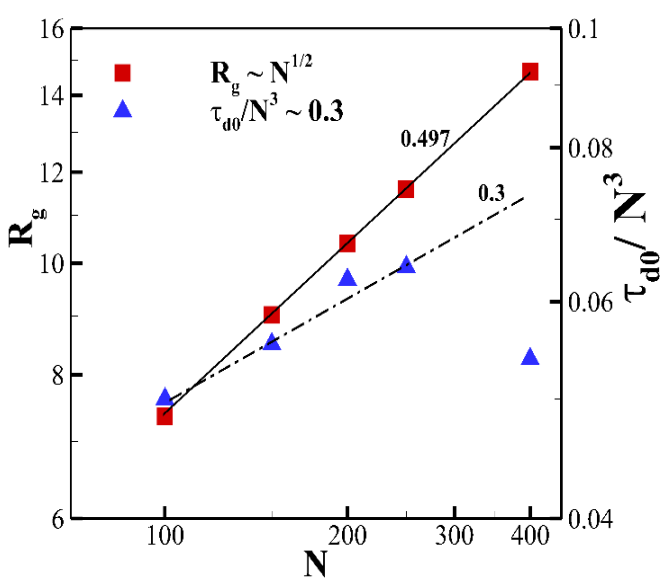

Figure 2-4. Predicted radius of gyration and longest relaxation time as a function of chain length at equilibrium. The radius of gyration shows the effective exponent of 0.5. The τ_{d0}/N^3 holds the scaling of 0.3 and the cross-over occurs at around N = 400 (Z_k =27).

Relaxation Time: The longest relaxation time of the system at equilibrium or the disengagement time depends on the molecular weight, and the Doi-Edwards tube model predicts the scaling of τ_{d0} α N^3. This prediction assumes only one mechanism for the relaxation, i.e., one dimensional diffusion along the primitive path. On the other hand, τ_{d0} α $N^{3.4}$ has been observed in the entangled regime in both experimental [69, 70]and computational [71] studies. The major reason for a larger exponent than 3 for finite N is contour-length fluctuation which is not accounted for in the original DE model.

To examine our simulation scaling behavior, we have measured the unit end-to-end auto-correlation function and fit it with an exponential function, i.e. $< \vec{u}(t).\vec{u}(0) >$ α a exp(-t/τ_{d0}). In the Doi-Edwards tube model, the time correlation of end-to-end vector is given by the sum of a series of odd exponential terms. Consistent with our findings, Nafar et al. [16] have shown that if the auto-correlation function is fitted by either one, two or three exponential terms, the predicted disengagement time is unchanged. Here, calculated results of τ_{d0} are depicted in Figure 2-4 versus N. The effective exponent for τ_{d0} is 3.3 from N=100 to 250 (τ_{d0} α $N^{3.3}$). However, a deviation from this exponent is observed at N=400. This crossover behavior has also been observed in other studies [70, 71] and it is attributed to the fact that at considerable entanglement density, contour-length fluctuation (a very fast mechanism) becomes less important, thus crossover occurs and the DE exponent of 3 is finally realized. It should be noted that in our simulation, the entanglement density at which the crossover occurs is 27; this cross over in experimental studies is observed when N/N_e ~ $O(10^2)$.

Diffusion: The motion of the polymer chain center-of-mass is described by a diffusion coefficient as,

$$D = \lim_{t\to\infty} \frac{1}{6t} < (\vec{r}_{cm}(t) - \vec{r}_{cm}(0))^2 > \tag{2.6}$$

The scaling of D with molecular weight has been extensively studied [68, 72]. Our results, depicted in Figure 2-5 demonstrate the scaling of $D \alpha N^{-2.069}$. This scaling is consistent with the simulations results of Kremer and coworkers [68, 73] as well as Padding and Briels [74] and Nikunen et al. [61]. Moreover, Pearson et al. [72] have experimentally demonstrated that over a broad range M_W, i.e., 600 to 12000 (g/mol), $D = 1.65\ M_W^{-1.98}$.

Overall, the correct scaling behavior at equilibrium confirm that excluded volume interaction and hydrodynamic correlations are accurately included in our DPD simulation algorithm.

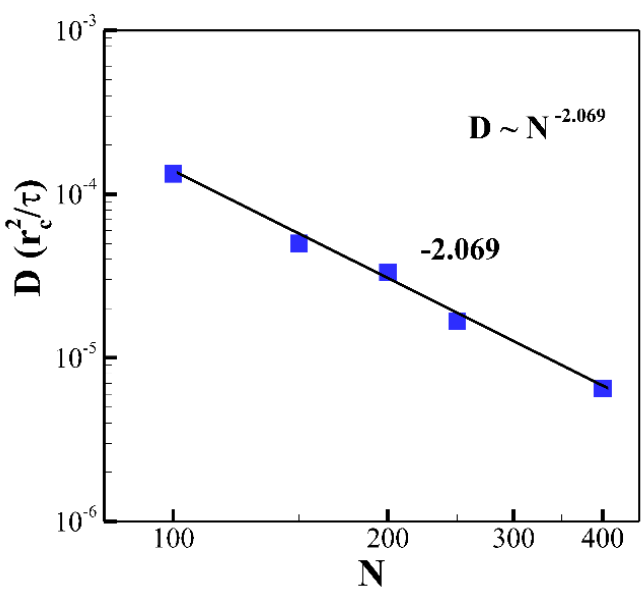

Figure 2-5. Diffusion coefficient as a function of chain length. The proper scaling limit is reached and the values are reported in the DPD units.

2.4 Simple Shear Flow

Although theories for chain liquids perform well at low field strength, their descriptions of the rheological behavior tend to break down once the field strength drives the fluid substantially into the nonlinear viscoelastic regime [2, 6, 75]. Unfortunately, procedures used to substantially reduce the number of degrees of freedom of the molecular-mesoscopic scale description, result in characteristic evolution equations for variables such as the conformation tensor or the extra stress tensor which change on macroscopic length and time scales but ignore the atomistic/mesoscopic-scale dynamics. This readily explains why these bulk-averaged theories often break down in the nonlinear viscoelastic regime where the timescales of the flow can become smaller than those associated with the time evolution of the macroscopic variables. Fortunately, recent united atom NEMD simulations of entangled (approximately ten kinks per chain at equilibrium determined based on Kröger's Z1 code) polymeric melts [15, 16], namely, $C_{400}H_{802}$ has provided significant new insight into flow-microstructure coupling of this class of fluids in simple shear, including a very intriguing new chain relaxation mechanism at high deformation rates, i.e., rotation/retraction dubbed "vorticity excursions". To this end, we have performed extensive DPD simulations of plane Couette flow of moderately entangled linear polymeric melts, i.e., with 200, 250 and 400 beads per chain, with equilibrium entanglements densities (kinks per chain determined via the Z1 code) of 13, 17 and 26 kinks per chain, respectively. The simulation results are in turn used to critically examine single chain dynamics and flow-microstructure coupling of moderately entangled polymeric melts in simple shear

flow. Moreover, our simulation technique allows examination of shear banding in this class of fluids which is the subject of the following chapter.

As noted earlier the disengagement time of the system, τ_d, is calculated by using the autocorrelation function of unit end-to-end vector. At equilibrium this time correlation function is equal to 1 at t = 0 and it gradually decays monotonically to zero at sufficiently long time. However, in simple shear flow of the N=250 fluid, at *Wi* > 10 the end-to-end autocorrelation function initially decreases, becomes negative, and in turn goes through a sequence of oscillations before returning to zero in ~ two time periods of the oscillation cycle (see Figure 2-6 on polymer relaxation behavior at different *Wi*). The aforementioned negative value is a clear indication of vorticity excursions. Hence, to analyze these autocorrelation functions, we have employed a single exponential function with an embedded cosine dependence to fit the disengagement and vorticity excursion time scales, i.e.,

$$< \vec{u}(t).\vec{u}(0) > \alpha\ c\ \exp(-t/\tau_d)\ \cos(-2\pi t/\tau_{rot}) \qquad (2.7)$$

The disengagement time and the rotation/retraction time scales as a function *Wi* for all of the entangled melts studied are displayed in Figure 2-7. For *Wi* ≤ 10, this time scale does not change substantially from its equilibrium value. However, for *Wi* > 10, all systems show an evident drop. The drop in τ_d (see Fig. 2-7) follows a power-law behavior with slope of -0.66, -0.64 and -0.65 for N = 200, 250 and 400 beads, respectively. NEMD simulation of Nafar et al. [76] for a polymer melt with a lower entanglement density (10 kinks per chain at equilibrium) also show a power-law behavior but with a slope of -0.73. The reduction in the rotation/retraction time scale shown in Figure 2-8 also obeys a power-

law behavior with slopes of -0.69 (N=200), -0.72 (N=250), -0.69 (N=400), -0.78 (NEMD [76]). The minor difference between NEMD and DPD simulations results for the aforementioned time scales is largely due the fact that the polymer chains used in the DPD simulations have a slight bending potential (to enhance entanglement density), thus their decorrelation times are longer than the flexible chains used in the NEMD simulations.

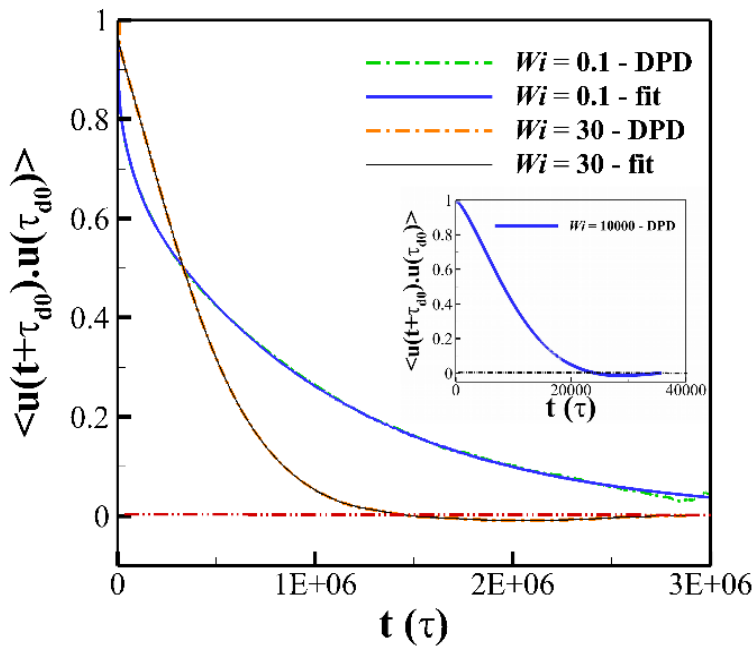

Figure 2-6. Autocorrelation function of unit end-to-end vector vs time at different *Wi* along with their fits for N =250. The fit for *Wi* = 0.1 is the summation of three exponential and the ones for *Wi* = 30 follows the equation 2.8. The autocorrelation function for *Wi* =10000 is shown in the inset.

The ratio of rotation/retraction relaxation time to the disengagement time is shown in Figure 2-9. The largest value (~10) is observed at *Wi* < 100 and the ratio decreases gradually to ~5 as the flow strength is increased. The *Wi* at which chain rotation/retraction

begins to occur is a function of the chain length and consequently the number of entanglements per chain. This is a direct consequence of the variation of number entanglements with *Wi*. Specifically, the entanglement density decreases as the flow strength is enhanced (see Figure 2-10). The onset of the rapid decrease in entanglement density is commensurate with the onset of vorticity excursion. At this *Wi* (O(10)) a network of highly-stretched chains give rise to dilated tube-like structures through which chains experience rotation/retraction.

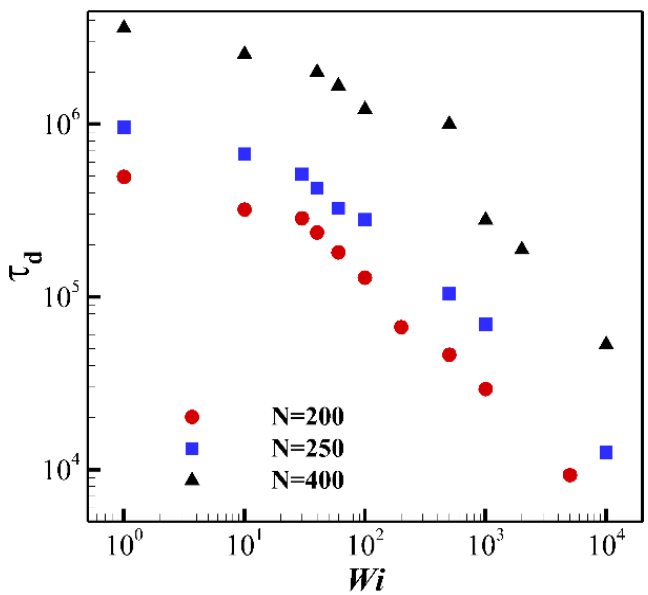

Figure 2-7. The longest relaxation time of dense melts with N = 200, 250 and 400 beads/chain as a function of *Wi*.

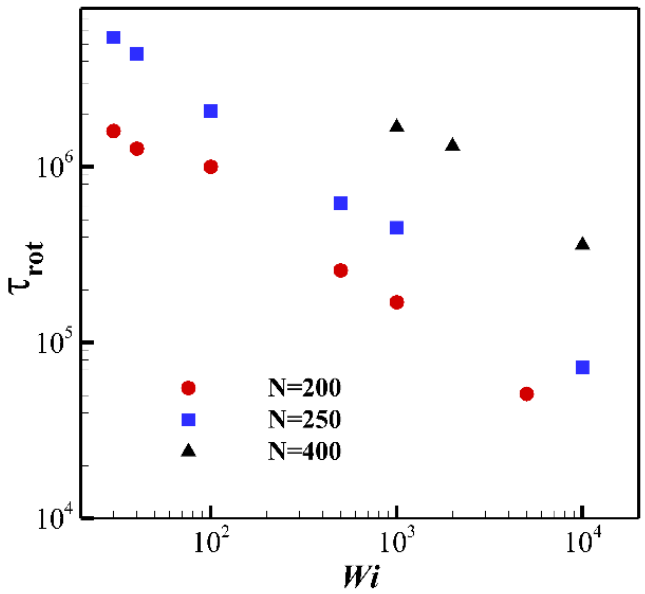

Figure 2-8. The rotational timescale of dense melts with N = 200, 250 and 400 beads/chain as a function of *Wi*.

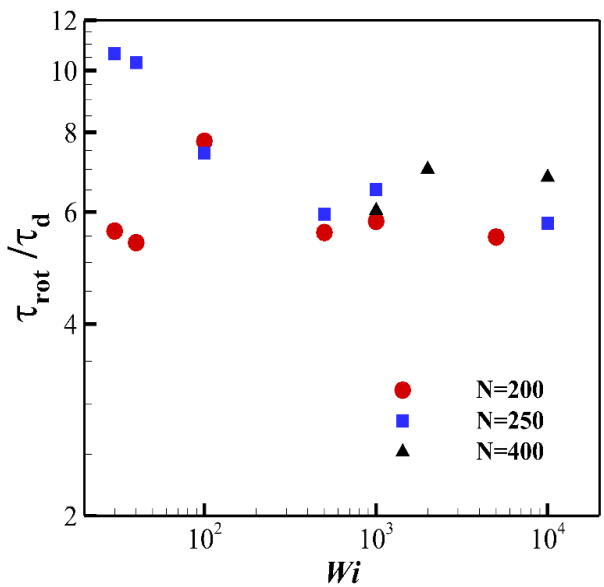

Figure 2-9. Ratios of the rotation to the disengagement times for the melt of entangled systems, N = 200, 250 and 400 beads/chain as a function of *Wi*.

Evidently, the *Wi* at which rotation/retraction begins to occur progressively increases as the number of entanglements per chains is increased. To this end, the interconnection between flow induced disentanglement and onset of rotation/retraction cycle is further scrutinized via examination of single chain dynamics and the entangled network topology.

The ensemble average number of entanglements per chain $< Z_k >$ as a function of *Wi* is depicted in Figure 2-10 (the entanglement density at *Wi*=1 and equilibrium are identical). As the shear rate is progressively increased, the flow enters the nonlinear viscoelastic regime (*Wi* >10), and $< Z_k >$ decreases slightly in response to the flow field. This is mainly due to the flow alignment of the chains as well as onset of chain stretch (See Figure 2-11 and 2-12 for the chain orientation angle and its mean fractional extension as a function of *Wi*). Simultaneously, the rotation/retraction frequency increases as the network becomes less entangled and ultimately loses its structure at very large *Wi*.

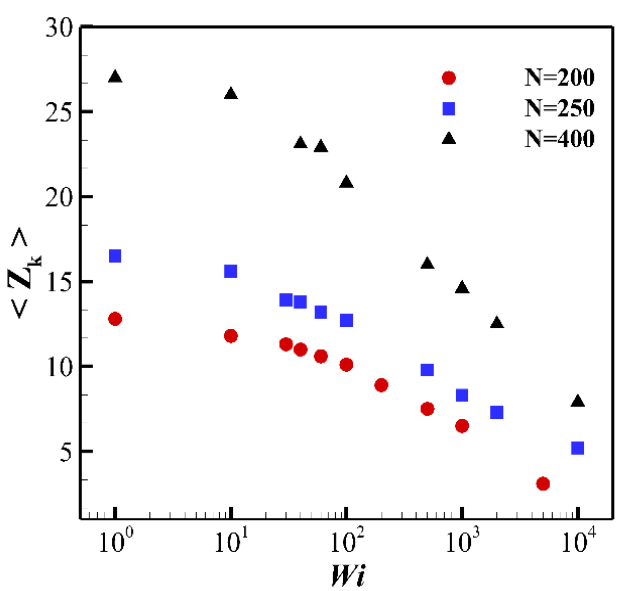

Figure 2-10. Average number of entanglements per chain as a function of *Wi* for different chain length, N = 200, 250 and 400 beads/chain.

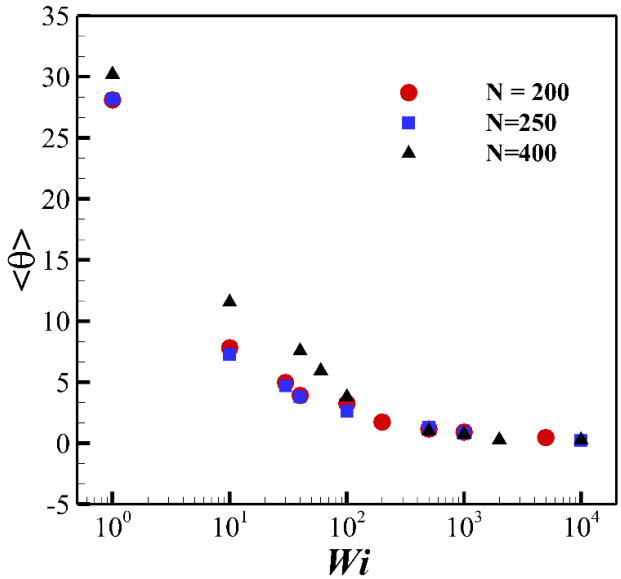

Figure 2-11. Average orientation angle vs *Wi* for different chain length, N = 200, 250 and 400 beads/chain.

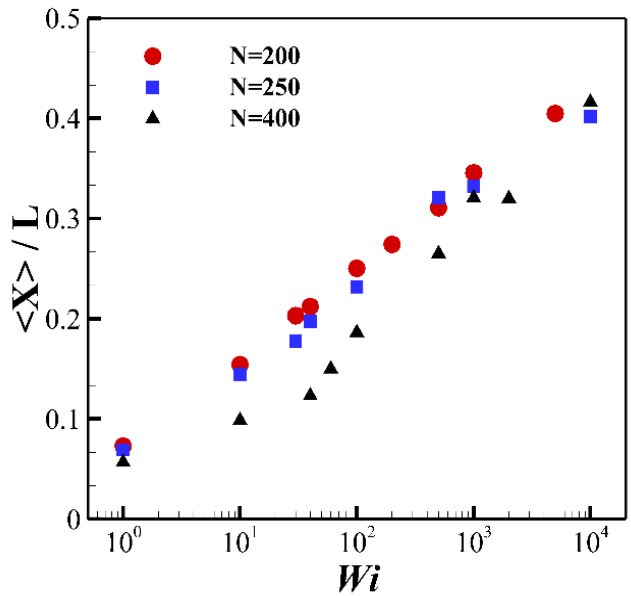

Figure 2-12. Mean fractional extension as a function of *Wi* for different chain length, N= 200, 250 and 400 beads/chain.

As mentioned earlier, entanglement or the persistent contact between the primitive paths of neighboring chains was detected by Z1 code. Z1 code determines the shortest path between the two ends of a chain via an optimization process while passing through the obstacles made by surrounding chains. Thus, the three dimensional primitive path <L> and the number of contacts or in their (Kröger et al.) terminology "kinks" $<Z_k>$ along this path is identified. In turn, the number of kinks per chain is related to the theoretical expression, $<Z> = <L>^2 / R^2$ in a non-trivial manner. At equilibrium, Everaers [77] has offered an explanation for the factor of two difference between $<Z_k>$ and <Z>, i.e., $<Z_k> \approx 2 <Z>$. Although our primitive path analyses at equilibrium are consistent with Everaers' finding, the entanglement density cannot be determined based on $<Z> = <L>^2 / R^2$ in non-equilibrium settings since the assumptions under which this relation is derived breaks down, i.e., the chains primitive paths do not obey Gaussian statistics. Therefore, we have used $<Z_k>$ as a measure of the entanglement density in our simulations.

Figure 2-11 demonstrates the orientation angle of end-to-end vector with respect to the flow direction (in the flow-gradient plane) θ as a function of *Wi*. The orientation angle is calculated from the order tensor $S = \frac{1}{2} < 3\vec{u}\,\vec{u} - I >$ where $\vec{u}$ denotes the chain unit end-to-end vector. Specifically, θ is defined as the angle formed between the flow direction and the eigenvector corresponding to the largest eigenvalue of the order tensor. At *Wi* > 10, the steep drop in the orientation angle from its limiting equilibrium value of 45° indicates significant chain alignment. As also evidenced from Figure 2-13 in which the single chain orientation angel at *Wi* =100 for N=250 is shown, the chain rotation and retraction is cyclical. During a typical cycle, the chain retracts from a highly stretched configuration to

a packed coil structure while the chain orientation angle is remained constant. At the minimum point of the period (as the chain begin to assume a coil structure), the orientation of the chain flips quickly as the chain ends pass each other at an instant, after which the chain quickly expands once more to a highly stretched configuration. Overall, the chain rotation/retraction cycle exists at *Wi* > 10 where the chain network is still moderately entangled, i.e., the rotation relaxation mechanism plays a significant role in the topological rearrangement even at moderate *Wi*.

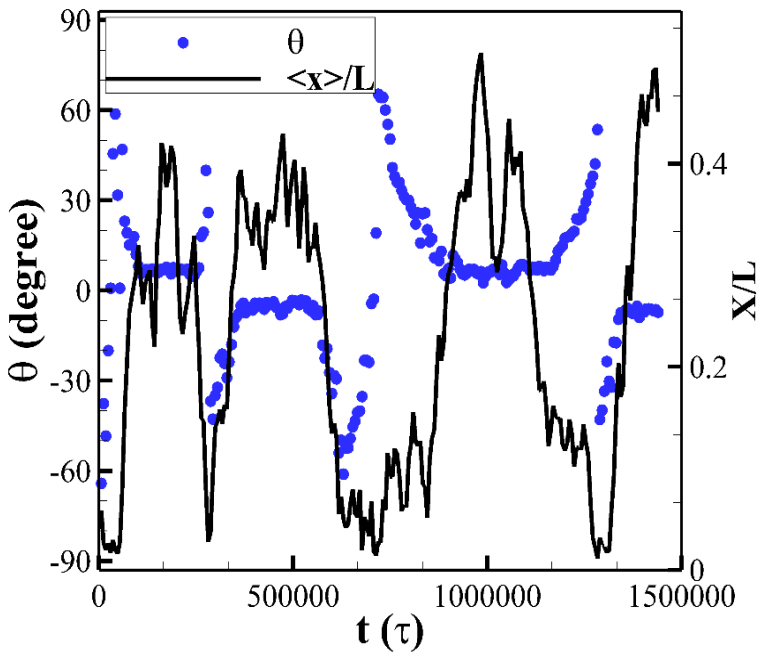

Figure 2-13. Chain orientation angle and fractional extensions a function of time for N =250 beads/chain at *Wi* = 100.

The mean extension <X>/L where L is the contour length and <X> is the mean end-to-end distance projected along the flow direction is shown in Figure 2-12. The onset of chain stretch occurs at *Wi* > 10 which roughly corresponds to a Rouse based Weissenburg

number, Wi_R > 0.5 where the Rouse time is estimated as follows: $\tau_R = {}^{\tau_d}/_{3 < Z >}$ (see Figure 2-14-(a,b)).At large *Wi* > 1000, chains have stretched on average 30% of their contour length and at a very high Wi= 10,000, the average chain extension exceeds 40% (<X>/L > 0.4; see Figure 2-12).

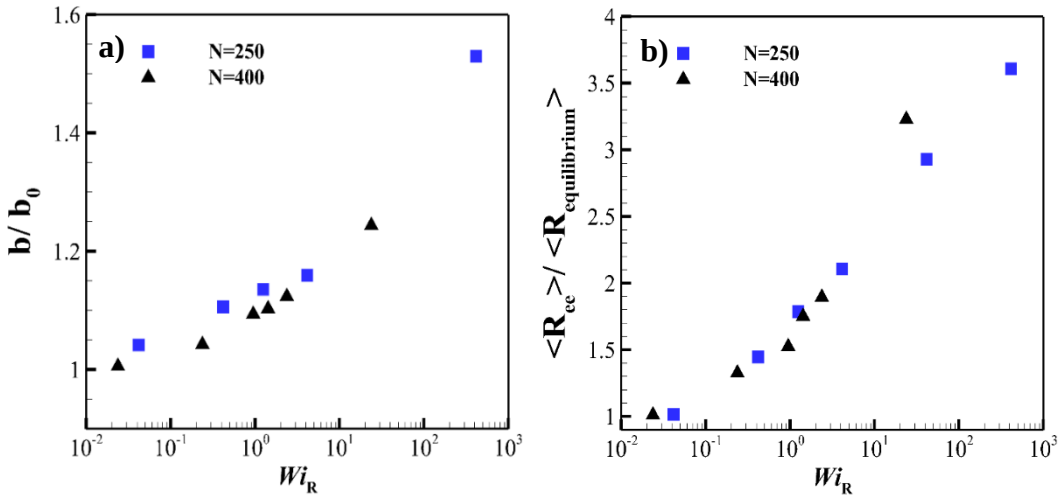

Figure 2-14. (a) The Kuhn length normalized by its equilibrium value, b_0 as a function of *Wi*. (b) The chain end-to-end distance normalized by the equilibrium value as a function of *Wi*.

The co-existence of aligned and extended chains with collapsed chains resulting from the rotation/retraction cycle indicates tube dilation. The length scale of dilated tubes can be examined via monitoring the average tube diameter, a, as a function of *Wi* (see Figure 2-15). To this end, the Kuhn length, b, of chains of various length, i.e., N=250 and 400 is computed based on the length along the backbone of the chain where orientation correlation is lost, i.e., the persistence length, P where b=2P. Persistent length is commonly determined

via the expression, $< \acute{u}(s).\acute{u}(0) > = \exp(-s/p)$ where s is the distance between the two points on the chain contour and $\acute{u}(s)$ is the tangent vector at position s along the chain. Following this procedure, b is determined to be 3.435 and 3.396 (r_c) for N = 250 and 400 beads/chain, respectively. The discrepancy between the calculated Kuhn length is ~ 1% showing the uncertainty in the computation of this quantity. In turn, the average tube diameter, d is related to the Kuhn step. Specifically, it is assumed to be twice the Kuhn length. The tube diameter starts growing substantially at $Wi \geq 100$ for N= 250 and eventually reaches ~8 Kuhn length at Wi=10,000. Hence, at very large strain rates, the characteristic motion of the chains becomes essentially that of single chain in a theta solvent. It should also be noted that onset of significant increase in the tube diameter for N=400 is delayed to $Wi \geq 1000$. Clearly, the onset condition is a strong function of entanglement density as a function of Wi.

A clear connection between individual chain dynamics and macroscopic response of the fluid, namely, stress exists. For example, the steady shear stress versus Wi (see Figure 2-16) can be divided into three distinct regions each with their own dominant chain dynamics. Specifically, the initial increase in the stress from its equilibrium value in region I where $\dot{\gamma} \leq \tau_d^{-1}$ corresponding to Wi<10, is predominantly due to the rapid chain flow alignment. Clearly in this regime the dominant chain relaxation mechanism is reptation as corroborated by the Gaussian distribution function of magnitude of end-to-end vector as depicted in Figure 2-17. As deformation rate increases, and one enters regime II, $\tau_d^{-1} \leq \dot{\gamma} \leq \tau_R^{-1}$, traditionally referred to as the CCR regime, significant chain orientation, and onset of chain extension gives rise to flow induced chain disentanglement leading to dilated tubes

in which vorticity excursions are executed by the chains. As shown by earlier continuum level computational studies [78-81] as well as our molecular investigation, in the CCR regime the complex chain dynamics described in details above give rise to nearly constant stress. As expected the probability distribution function of end-to-end vector in this regime significantly widens as a result of multitude of configuration that exist during a vorticity excursion cycle with a commensurate broadening of the relaxation spectrum. In region III, i.e., $\dot{\gamma} \geq \tau_R^{-1}$ chain stretch is enhanced considerably and vorticity excursions occur at a much higher frequency leading to further widening of the end-to-end distribution function and appearance of a peak for highly stretched chains ($Wi \geq 1000$). Simultaneously, a peak corresponding to chain sizes smaller than the equilibrium R_g of the molecule appear indicating the existence of highly compact configuration. The observations of the two peaks in the probability distribution function are a clear signature of rapid vorticity excursions. This also emphasizes that the entanglement network has essentially been destroyed (see Figure 2-10) and the chain dynamics is very similar to that of a single chain in a theta solvent.

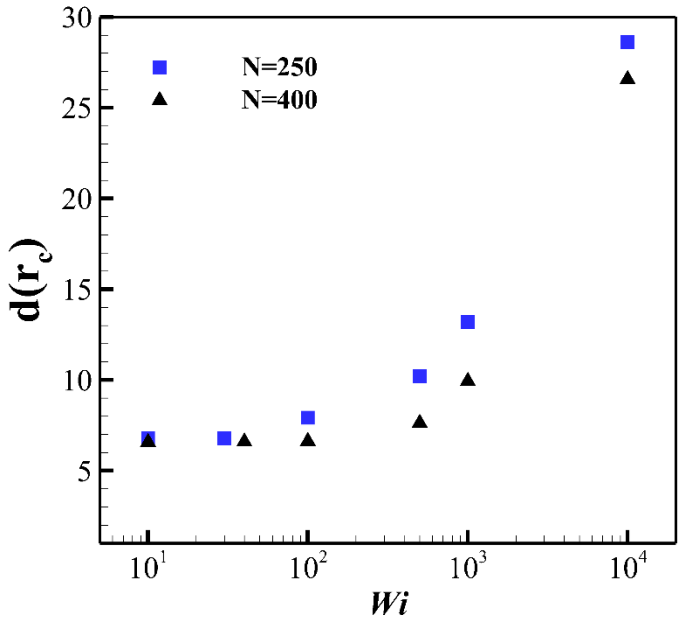

Figure 2-15. Tube diameter, a versus *Wi* calculated via formulae d = < L >/< Z_k > for N=250 and 400 beads/chain.

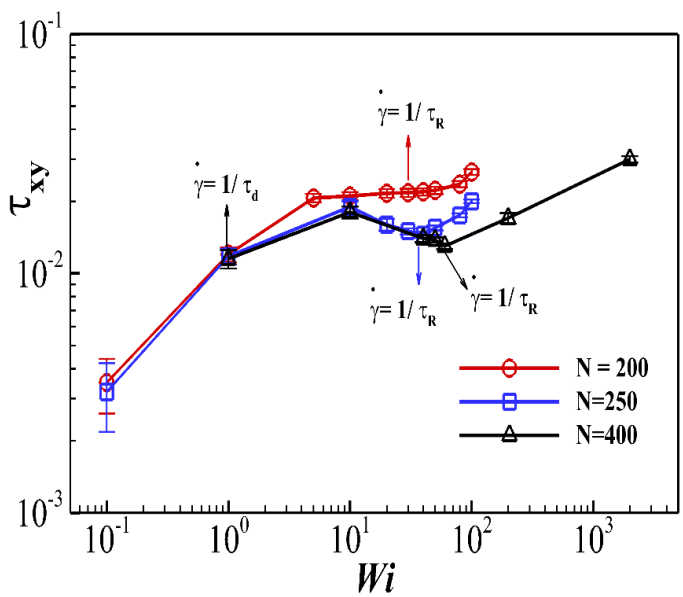

Figure 2-16. Steady shear stress as a function of Weissenburg number, *Wi*. Rouse time, τ_R is estimated via τ_d/τ_R= 3<Z>.1000, N=400. Time is scaled by the disengagement time at the applied shear rate. This figure appeared in a previous publication [113]. It has been also included to facilitate the discussion.

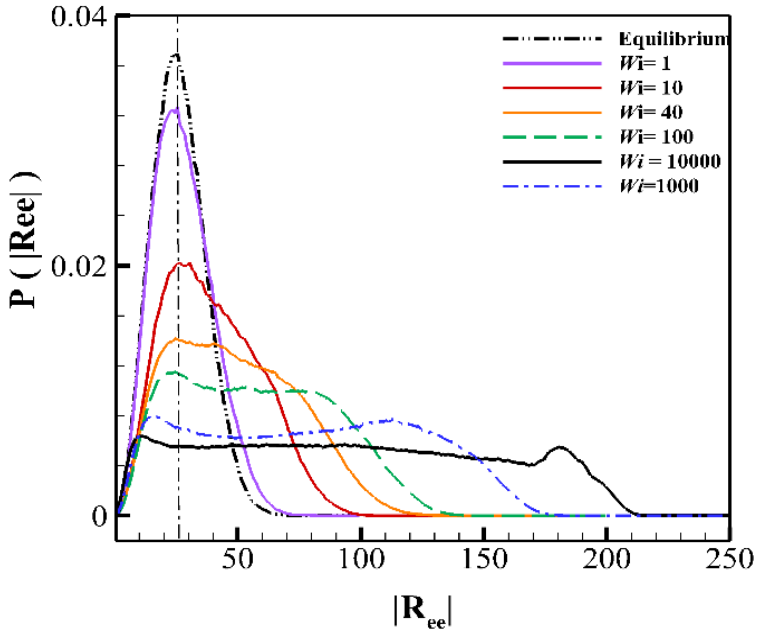

Figure 2-17. The probability distribution of magnitude of end-to-end vector vs R_{ee} at various *Wi* values for N = 250 beads/chain.

2.4 Conclusion

Overall, our DPD results presented in this part are in great consistency with NEMD simulations of Nafar et al. [16] and Baig et al. [15]. This is for the first time that DPD fidelity under steady flow in the entangled regimes ($\langle Z_k \rangle \geq 13$) has been gauged. In addition, the detailed single chain dynamics and relaxation mechanisms in the polymer melt with varying flow strength has been scrutinized. Thus, the flow-microstructure coupling is now clear. It has been shown that three different flow regions exist along their relaxation mechanism. For weak flows in the proximity of linear viscoelastic regime, $\dot{\gamma} \leq$

τ_d^{-1}, the reptation is the dominant relaxation mechanism. As *Wi* increases, at $\tau_d^{-1} \leq \dot{\gamma} \leq \tau_R^{-1}$, the flow enters the non-linear viscoelastic regime, significant chain alignment and the onset of chain extension lead to the flow-induced chain disentanglement. Moreover, as the chain disentanglement occurs, the tubes are dilated and thus vorticity excursion, i.e. significant segment reorientation can be performed, however, the tumbling frequency is small. The relaxation spectrum becomes broad as various mentioned chain dynamics are available. The last region, $\tau_R^{-1} \leq \dot{\gamma}$, appears at large *Wi* where the entanglement network essentially collapses, chains don't experience the resistance from the surroundings and the shear flow becomes similar to the dilute polymer solution in theta solvent. Both stretch and orientation take place effectively, thus the Rouse-like relaxation mechanism is more realistic. The configuration diversity observed in the flow confirms that the chain motion is free.

The realization of relation between single chain dynamics and relaxation mechanisms as well as existence of various regimes in the entangled polymers under flow equips us to investigate the inhomogeneous *shear banding* phenomenon with resolution. The shear banding molecular investigation is fully discussed in Chapters 3 and 4.

Chapter 3

Molecularly Universal Criterion for Shear Banding: Formation of Local Inhomogeneity Mechanism

This Chapter is based on the submitted papers.

"Elucidating the Flow-Microstructure Coupling in Highly Entangled Polymer Melts: Part II. Molecular Mechanism of Shear Banding," M. Mohagheghi and B. Khomami, *Journal of Rheology*, invited paper, JOR-15-327-SB.

"Molecularly Based Criteria for shear Banding in Transient Entangled Polymeric Fluids," M. Mohagheghi, B. Khomami, *PRE*, Revision submitted on 23-Feb-2016, LM15163.

3.1 Introduction

In this chapter, the second in a series of articles describing the flow physics of highly entangled polymeric melts, hi-fidelity DPD simulations described and benchmarked thoroughly in our preceding chapter is used to analyze the "formation of localized inhomogeneity", the prerequisite for "shear banding" phenomenon. Our primary goal is to gain insight into the physical origin of shear banding in entangled polymeric fluids by investigation the molecular processes that lead to this intriguing phenomenon. To this end, fundamental understanding of flow microstructure coupling described in the preceding chapter [82] is an essential first step in establishing the intricate relationship between flow induced chain disentanglement, chain relaxation mechanisms and formation of local inhomogeneities, believe to be a key ingredient for development of shear banded structures.

To achieve this objective, extensive analysis including evaluating the free energy of the system has been performed.

In the former chapter, we elucidated the flow-microstructure coupling in polymeric fluids with average entanglement densities $<Z_k> \geq 13$ and demonstrated that three prevalent relaxation mechanisms, namely, reptation, vorticity excursion, and Rouse are the predominant mechanism of macromolecular relaxation in the three distinct flow regimes. Specifically, it was demonstrated that in relatively weak flows, $\dot{\gamma} \leq \tau_d^{-1}$, reptation is the dominant relaxation mechanism. As *Wi* ($Wi = \dot{\gamma}\tau_d$) increases, i.e., $\tau_d^{-1} \leq \dot{\gamma} \leq \tau_R^{-1}$, and the flow enters the non-linear viscoelastic regime, significant chain alignment and the onset of chain stretch lead to the flow-induced chain disentanglement. Moreover, as the chain disentanglement occurs, the "tubes" are dilated enabling efficient vorticity excursion, allowing significant chain segmental reorientation to occur, although the frequency associated with these excursions is small. This additional relaxation mechanism leads to significant broadening of the relaxation spectrum in this region. The last region, $\tau_R^{-1} \leq \dot{\gamma}$, appears at large *Wi* where the entanglement network is nearly collapsed; hence, chains don't experience significant constraints from the surrounding chains and the flow becomes similar to a semi dilute/dilute solution in theta solvent. Both stretch and orientation take place effectively, thus Rouse-like chain dynamics is dominant.

In the present and following chapter, we have conducted a thorough study of the shear banding phenomenology in entangled polymer melts. Specifically in this chapter, we have performed a series of step-strain simulations with different entanglement densities $<Z> \geq 17$ as well as start-up simulations at a specific shear rate (N=250 at *Wi*=30) by adjusting

the time taken for the deformation rate to achieve its steady value. Basically, three different ramp-time were chosen to examine the importance of chain stretch and orientational relaxation on the onset of shear banding. To this end, the intricate relation between chain segmental stretch, stress and orientation relaxation, presence of stress overshoot and formation of local inhomogeneities in the entanglement network and shear banding is identified. Specifically, our detailed analyses have revealed that if chain orientation has ample time to relax before the stress reaches its steady state value, inhomogeneities would not occur and shear banding is obviated.

In turn, in the following chapter, we elucidate the consecutive steps leading to shear banding, i.e. the development of spatially inhomogeneous chain disentanglement as a result of local inhomogeneous deformation. Moreover, an explanation for the stability of steady and transient shear banded flows is proposed based on the well-known interfacial stability mechanism of stratified polymeric fluids. Overall, these studies (presented in Chapters 3 and 4) have provided a clear picture of shear banding and have paved the way for a more comprehensive understanding of shear banding in inhomogeneous shear flows such as flow of polymer melts in tubes and capillaries.

To place into context our work in this vast area of research, a brief overview of the pertinent experimental and theoretical studies is provided in the next section.

3.2 Background

In 1979, Doi and Edwards predicted the possibility of flow instability in the steady shear flow of entangled polymeric melts modeled with their original tube-based

constitutive equation. In the original tube-model, a stress maximum appears at the shear rate in the vicinity of the inverse of the reptation time, τ_d^{-1} and the subsequent decreases in the shear stress value lead to a non-monotonic relation between shear stress and shear rate. They suggested that the non-monotonic behavior of the shear stress flow curve will lead to an inhomogeneous deformation state where bands with distinct deformation rates could coexist.

Shear banding in complex fluids was first observed in worm-like micelles [83-85]. Specifically, Cates demonstrated that the predictions of analysis are consistent with shear banding observed in wormlike surfactant solutions [83, 86, 87]. Specifically, he demonstrated that his proposed constitutive equation for worm-like micelles leads to a flow instability in the region of non-monotonic shear stress shear rate regime that evolves into a shear banded flow [85] at stresses and shear rates observed experimentally.

Experimental results of entangled polymer solutions showed discrepancies with the DE theory specifically in large deformation rates and in response to a step strain. Osaki and Kurata [88] and Vrentas and Graessley [89] observed stress relaxation occurring much faster than the one predicted by DE theory in the entangled polymers $Z \geq 60$, later this anomalous relaxation was called “type C” relaxation [88, 89]. On the other hand, in 1983, Marrucci and Grizzuti (MG) [90] analyzed the possibility of formation of inhomogeneities/instabilities via a free energy analysis derived based on the Doi-Edwards tube-model to explain the discrepancy between the stress measurements by experiments [88, 89] and DE prediction. They showed that an inflection point in the free energy exists and will likely result in an elastic instability. They qualitatively argued that the

aforementioned instability will persist unless significant orientation relaxation occurs. Further, they suggested that on some relatively small length scale, this elastic instability would cause inhomogeneous deformation leading to shear banding. Morrison and Larson [91] assessed MG theory by using monodisperse and bi-disperse Polystyrene solutions at different concentrations and pointed out that MG theory is qualitatively correct in the prediction of strain inhomogeneities. Later, Venerus and coworkers [92, 93] studied step strain experiments and concluded that many of the anomalous "type C" responses could be explained by experimental conditions such as wall slip, imperfect step strain history or transducer compliance; however, a number of observed anomalous responses could not be described by experimental conditions and may be caused by some other factors not clearly identifiable from their experiments.

Eventually, in 2006, Tapadia and Wang [94] witnessed the existence of shear banding in entangled polymeric fluids by flow visualizations in a cone-and–plate rheometer via Particle Tracking Velocimetry (PTV). Specifically, they observed that upon step-strain start-up, the steady velocity profile was non-linear in the gap between the cone and plate when the fluid was sheared in the stress plateau region. Further, numerous experiments also showed the existence of this inhomogeneous behavior in different types of flows in well entangled polymeric fluids (molecular weight Mw ~ $1 - 2 \times 10^6$ g/mol) and DNA solutions with number of entanglement Z ≥ 40 [95-101]. Examples include, steady and transient shear band formation and velocity recoil during start-up [94, 96, 99, 102], transient shear banding in large amplitude oscillatory shear (LAOS) [98, 103], inhomogeneous response including negative velocity recoil after step strain performed at

high shear rates [95, 104]. Tapadia and Wang ascribed shear banding to “cohesive failure” or “elastic yielding”. On the other hand, Sui and McKenna [105] argued that the aforementioned non-linear behavior is a flow instability and is caused by surface distortion, either by edge fracture or elastic spiral ripples in the free surface. It should be noted that the meniscus in Wang’s cone-and-plate experiments was wrapped with transparent film to avoid the edge fracture.

The most prevalent yet highly controversial theoretical basis offered to rationalize the occurrence of shear banding in entangled polymeric fluids is the *non-monotonic constitutive* relation between shear stress and shear rate as originally proposed by Doi and Edwards. However, the same criterion i.e., “mechanical instability” defined by the negative slope of shear stress constitutive relation, cannot explain the occurrence of transient shear banding on the monotonic part of the curve. Therefore, Olmsted et al., have carried out continuum level stability simulations of worm-like micelles and polymer solutions [106-110] to find an explanation for the inhomogeneous behavior of the flow. In the context of transient shear banding in polymer solutions, they have utilized the diffusive Rolie-Poly model [7, 106] and demonstrated that these fluids are dynamically unstable, i.e., the instantaneous constitutive curve at any transient time is non-monotonic. This does not imply a direct connection to a steady state non-monotonic flow curve. In worm-like micelles [108] where the diffusive Johnson-Segalman model was used with the two-fluid approach coupled to concentration, shear banding was only observed in the negative slope region of shear stress versus shear rate, i.e., a “mechanical instability”. However, they have also suggested that the shear-induced demixing (SID) instability broadens the instability

window to the regions where the flow is monotonic and, that can render the flow to be inhomogeneous. On the other hand, Cromer et al. [111] have demonstrated that *steady shear banding* with a realistic *monotonic constitutive curve* can be realized only if a proper coupling of polymer stress to polymer concentration is enforced. Though nearly identical stress constitutive relation is used in the aforementioned linear stability analyses, there are apparent discrepancies between their conclusions. This is due to the fact that the results are very sensitive to the assumed rate of CCR and there is no consensus yet on precise CCR implementation. Also, the choice of local perturbations defined in the form of stress gradient, noisy initial conditions or concentration fluctuations affect the calculations and result. Thus, linear stability predictions based on the most advanced constitutive equations are not conclusive and require additional molecular level information before accurately addressing flow instability and shear banding in the entangled polymeric flows. To this end, development of atomistic or coarse-grained simulation models is essential in determining the critical condition for the onset of shear banding.

In fact, a recent study by Cao and Likhtman [112] has demonstrated the utility of NEMD simulations in predicting shear banding in planar Couette flow of entangled mono-disperse polymeric melts, modeled as bead-spring chains. The fluid on average has ten entanglement per chain at equilibrium and shows a non-monotonic relation between shear stress and shear rate. Both transient and steady shear banding were observed in the simulations and each corresponds respectively to the monotonic and non-monotonic parts of the flow curve.

Although to date shear banding in entangled polymeric melts has been documented in two molecular simulation including our recent work [113] and in many experiments, the molecular origin of this intriguing phenomenon is not fully understood. To this end, our main goal in this study is to elucidate the molecular origin of inhomogeneities in this class of fluids and its relation to shear banding. Motivated by MG theory, the effect of deformation rate ramp-time on segmental/stress and orientation relaxation and formation of local inhomogeneities in the entangled network and its relation to shear banding has been thoroughly examined.

3.3 Simulation Technique

The simulation methodology employed in this study, DPD, the details of the simulation technique, i.e., specification of forces, box size, etc. is identical to the previous chapter. Therefore, we refer the reader to Section 2.2 of Chapter 2 for more details.

3.4 Results and Discussion

In what follows, the molecular origin of shear banding is discussed, starting with the formation of local inhomogeneities in the entanglement network. Further, in Chapter 4, the evolution of local inhomogeneity to the incipient shear banded flow structure is elucidated.

3.4.1 Continuum Observation of Shear Banding Existence

The shear stress and viscosity as a function of *Wi* for the chain lengths of N=250 and 400 are depicted in Figure 3-1-(a,b). Both shear stress versus shear rate flow curves are non-monotonic due to the rapid shear thinning of viscosity with power law exponents $Wi^{-1.042}$ (N=250) and $Wi^{-1.028}$ (N=400). The temporal evolution of the shear stress for a step-strain start up protocol for the aforementioned monodisperse polymer melt with chain length N = 250 (roughly equivalent to $C_{750}H_{1502}$) and 400 (roughly equivalent to $C_{1200}H_{2402}$) as a function of strain or equivalently time at different shear rates for step is shown in Figure 3-2. No stress overshoot is observed for $Wi < 10$. At higher $Wi \geq 10$ a stress overshoot is observed at two strain units ($\gamma \sim 2.0$) consistent with theoretical prediction of DE constitutive model. The time taken for the stress to decline from its maximum transient value to its steady state dubbed "stress relaxation regime" is roughly one disengagement time, τ_d. It should be noted that τ_d refers to the disengagement time at the given shear rate and not the equilibrium disengagement time, τ_{d0}.

Steady shear banding has been observed at $Wi \in [30, 50]$ and $Wi \in [40, 60]$ for N=250 and 400 respectively. Moreover, transient shear banding occurs at Wi= 100 (N=250), 500 and 1000 (N=400). Prototypical shear banded flow structures are shown in Figure 3-3(a-c) at different *Wi* and chain lengths. Figure 4-3(a,b) and 3(c) depict steady and transient shear banding respectively. Analogous characteristics during the first disengagement time is observed for both cases, namely, linear velocity profile at the stress overshoot, followed by emergence of local velocity perturbations at $t \sim 0.4\ \tau_d$. These disturbances are amplified

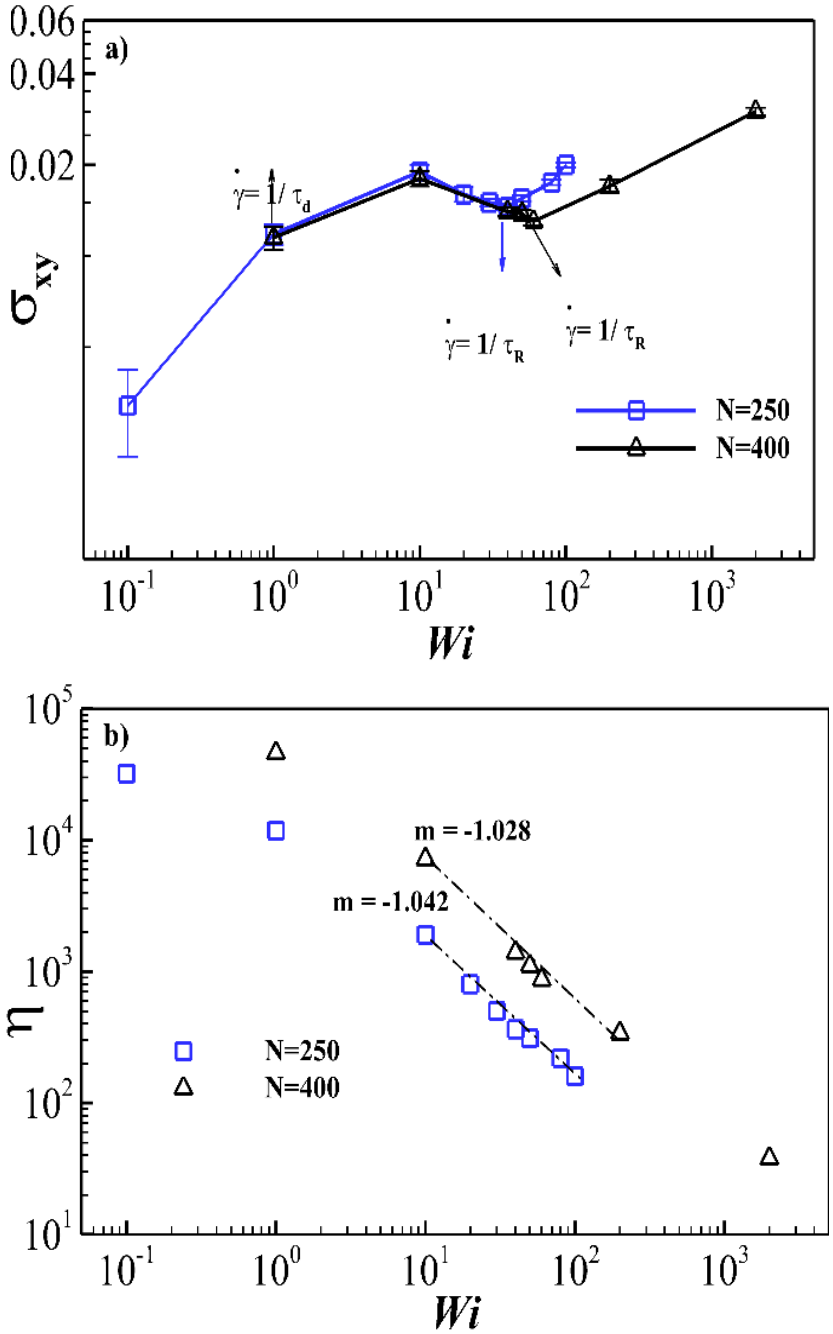

Figure 3-1. (a) Steady shear stress and (b) viscosity as a function of *Wi* for different chain length, i.e. N=250 and 400 beads per chain. Rouse relaxation time, τ_R is determined via $\tau_R = \frac{\tau_d}{3Z}$. Part (a) of this figure appeared in a previous publication [113]. It has been also included to facilitate the discussion.

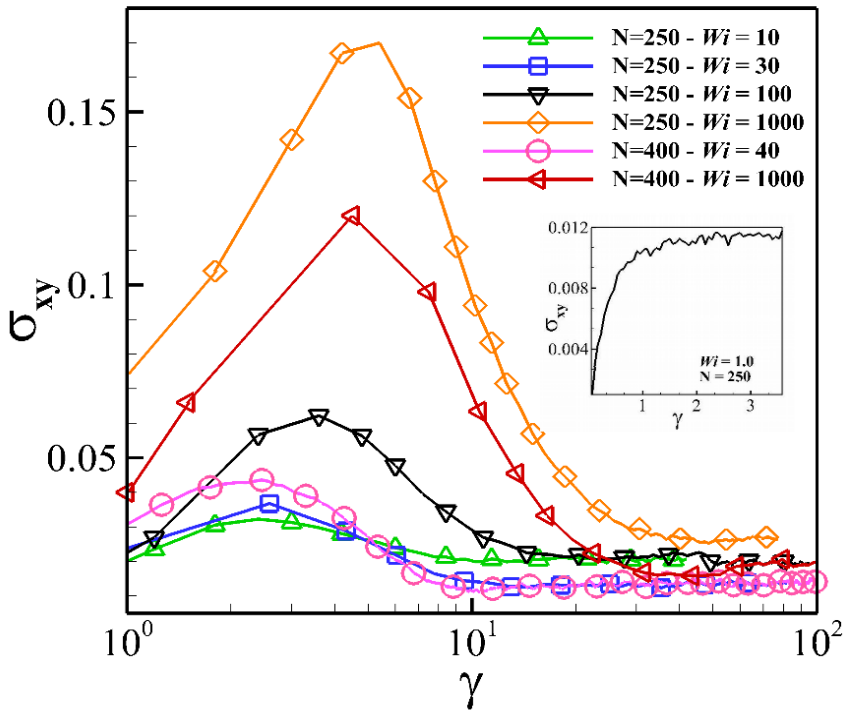

Figure 3-2. Shear stress evolution as a function of strain for different chain length and *Wi*. No stress-overshoot emerges for *Wi*=1, N=250 shown in the inset.

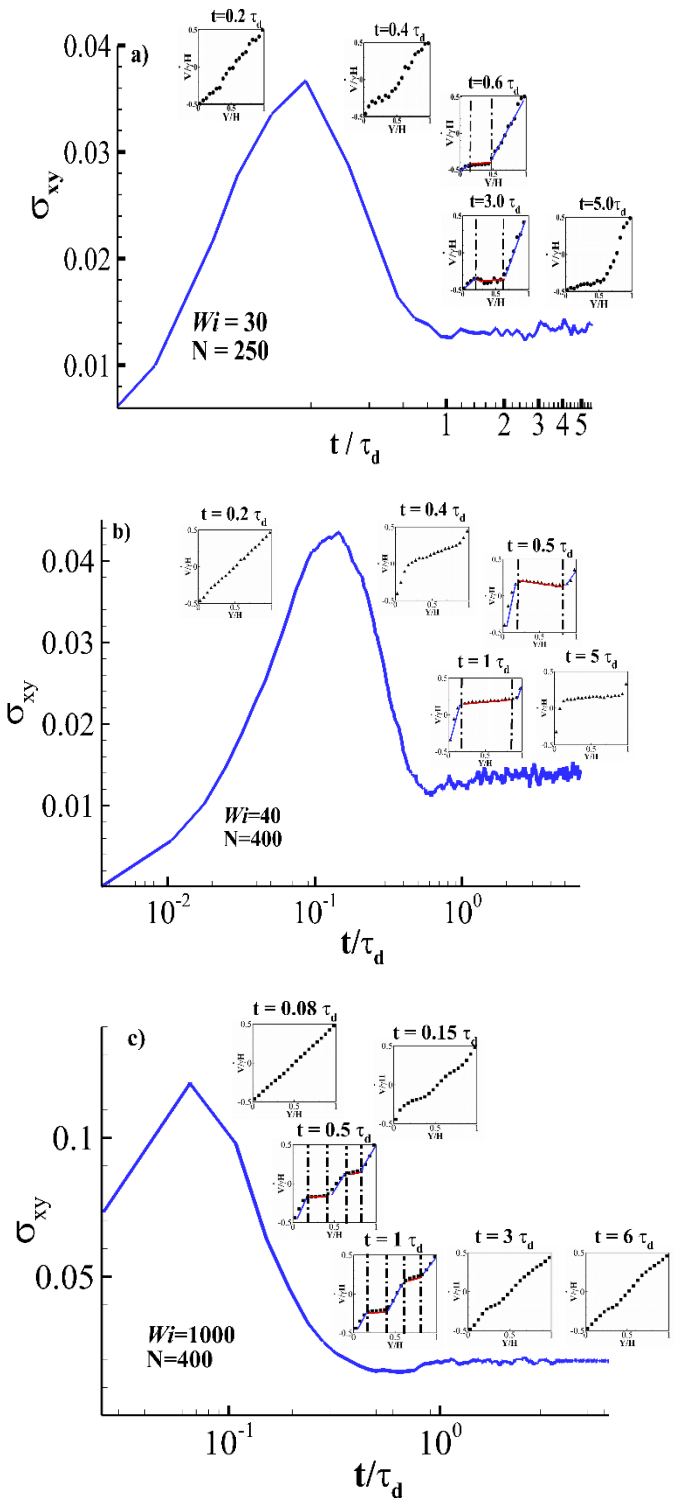

Figure 3-3. Shear stress and velocity profile temporal evolution for (a) steady shear banding at Wi=30, N=250, (b) steady shear banding at Wi=40, N=400 and (c) transient shear banding at Wi=1000, N=400. Time is scaled by the disengagement time at the applied shear rate.Part (a) of this figure appeared in a previous publication [113]. It has been also included to facilitate the discussion.

and lead to the incipient shear banded flow structure at t ~ 0.6 τ_d. Both incipient structures continue to evolve, i.e., the thickness of the fast and slow band change until either a steady shear banded structure is realized at ~5 τ_d or the banded velocity profile returns to its homogeneous linear form after ~ 3 τ_d.

3.4.2 Free - Energy Analysis

Up to this point, we have shown that the incipient banded structures always form in the stress relaxation regime. Moreover, the banded flow structures are realized after localized disturbances have sufficiently evolved in time. Hence, understanding the molecular mechanism that leads to the formation of localized inhomogeneities in the velocity gradient direction in the stress relaxation regime is an important first step in development of a molecular mechanism for shear banding in this class of fluids. To this end, motivated by prior analyses of MG [114] we have examined the temporal evolution of the free energy of the system under a step-strain start-up protocol. Specifically, the Helmholtz free energy change per unit volume is calculated via the formulae,

$$\Delta A = -\frac{1}{2}\,(Q + Q^{+}) : \sigma \qquad (3.1)$$

Where $(Q + Q^{+})/2$ is a strain tensor and σ is the stress tensor. The temporal evolution of the system free energy expressed in kT units as a function of strain is depicted in Figure 3-4. Evidently, the free energy has a positive curvature at small values of γ (up to γ ~ 2.0)

presumably due to the fact that the chains are almost affinely deformed in this region. A negative curvature emerges for $\gamma > 2.0$; hence, an inflection point at $\gamma \sim 2.0$ where the maximum transient stress is observed exists. The inflection point in the free energy suggests the possibility of an instability manifested in form of local inhomogeneities.

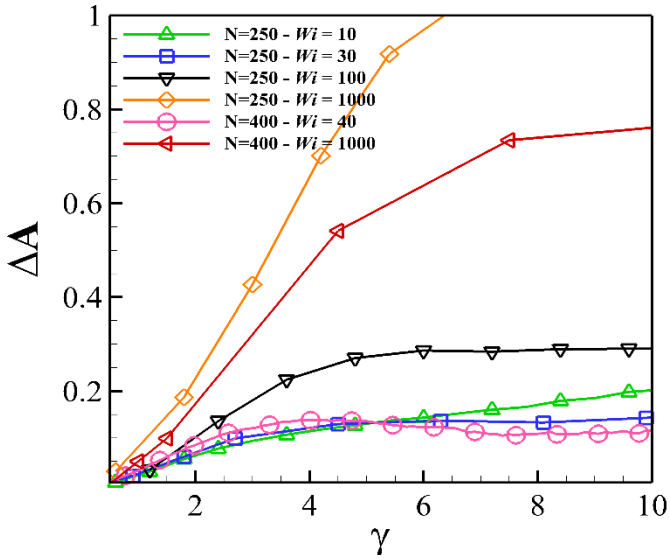

Figure 3-4. Free energy change per unit volume for different chain length and *Wi*.

3.4.3 Molecularly based Criteria for Formation of Localized Inhomogeneity

To understand the molecular of origin of formation of local inhomogeneity, individual chain dynamics during the stress relaxation process has been extensively examined. Overall, the chains relax their stress in two steps; in the first step, tension is relaxed by

segmental stretch relaxation, a very fast process; in the second step, chains relax their orientation. Specifically, the flow-induced anisotropic segmental configuration observed in stretched and flow aligned chains is relaxed to isotropic equilibrium like chain structures (coil) via a rotation/retraction cycle, composed of various folded configurations as depicted in Figure 3-5. As the shear rate increases, *Wi* > 10, the entanglement density drops leading

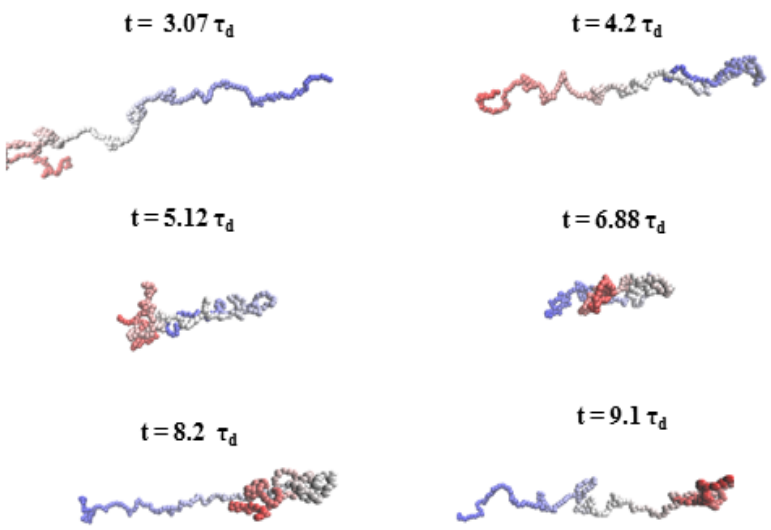

Figure 3-5. Configuration snapshots of a randomly chosen single chain at various incremental times at *Wi* = 40, N=400.

to tube dilation which in turn enables the aforementioned rotation/retraction cycle that is the predominate chain orientation relaxation mechanism. However the rotation time scale is much longer than the reptation time scale, i.e., an order of magnitude larger than τ_d, especially at smaller *Wi* (Please refer to Figure 2-8, 9 and 2-14 in the former chapter). Therefore, based on these observations, we propose that the large discrepancy between the

segmental stress/stretch (fast) and segmental orientation relaxation time (slow particularly compared to the time for the deformation rate to reach its steady state value) scales leads to local inhomogeneity in the entanglement network. Specifically, the combination of flow induced chain disentanglement and insufficient time for orientation relaxation leads to inhomogeneous entanglement density and a commensurate local variation in fluid properties in the velocity gradient direction that cause a flow transition, i.e., formation of deformation inhomogeneity that leads to the incipient shear banded flow structure. The effect of local inhomogeneity on the spatially inhomogeneous chain deformation is fully discussed in the next chapter.

To elucidate the aforementioned molecular mechanism for formation of local inhomogeneities, the chain orientation relaxation is examined via the primitive path segmental orientation distribution function (see Figure 3-6). To quantify the segments that possess isotropic or anisotropic orientation, the following procedure has been used. Fraction of chain segments holding orientation angle (with respect to the flow direction) between $-5\langle\theta\rangle$ and $5\langle\theta\rangle$ are considered to be the flow-induced anisotropic fraction, λ, of the chain segments. Here, $\langle \theta \rangle$ is the average orientation angle at the applied shear rate. The orientation angle criteria has been defined as $\pm 5\langle\theta\rangle$ to take into consideration the relative isotropy at each shear rate since the chains are more aligned as the shear rate increases (see Figure 2-10 of the former chapter). Hence, this relative measure of orientation angle has been used to differentiate between isotropic and anisotropic configurations at different flow strength. Specifically, this particular choice was motivated by the ratio of the isotropic orientation angle at equilibrium, 45° to the average orientation

angle at *Wi* =10, $\langle\theta\rangle|_{Wi=10} \sim 9^{o}$. The $\langle\theta\rangle$ at *Wi* =10 was chosen since at *Wi* > 10, chain alignment is significantly enhanced and orientation relaxation plays a central role in the chain overall relaxation process. On the other hand, the (1-λ) fraction with orientation angle larger than $5\langle\theta\rangle$ and smaller than $-5\langle\theta\rangle$, compose the isotropic fraction of the chain segments. Hence, the fraction (1-λ is evaluated by calculating the area under the primitive path segmental orientation distribution function for orientation angles larger than $5\langle\theta\rangle$ and smaller than $-5\langle\theta\rangle$). As *Wi* increases, chains are generally more aligned and thus λ would increase slightly. However, the increase in anisotropic fraction, λ does not imply that orientation relaxation is less effective. In fact, the local minimum in the anisotropic fraction manifested by the negative orientation angle grows as *Wi* is enhanced. The negative maximum appears as a consequence of existence of a large number of folded configurations resulting from the rotation/retraction cycle depicted in Figure 3-5-(b, c, e). Hence, more chains experience the rotation/retraction cycle with increasing *Wi*. In conclusion, If orientation relaxation occurs significantly, i.e., frequently at the given shear rate such as N=250, *Wi*=1000, the homogenous deformation will be preserved. Otherwise, if a large fraction of sub-chains are still anisotropic and orientation hasn't relaxed sufficiently during the stress relaxation period, inhomogeneity forms.

3.4.4 Formation of Localized Inhomogeneity: Mathematical Description

As discussed earlier, the negative curvature in the free energy suggests formation of local inhomogeneities. To quantitatively determine the criteria for formation of local inhomogeneities in the flow, one must consider both the chain relaxation and the system

free energy. As suggested by MG [114], this can be done by utilizing the following simple expression:

$$\lambda \frac{d^2(\Delta F)}{d\gamma^2}\Big|_{\gamma} + (1-\lambda)\frac{d^2(\Delta F)}{d\gamma^2}\Big|_{0} < 0 \qquad (3.2)$$

The first term in this expression is the contribution of the anisotropic chain segments to the overall balance. The magnitude of this term determines whether local inhomogeneities are likely to occur as $\frac{d^2A}{d\gamma^2}\Big|_{\gamma}$ is the negative free energy curvature. The second term signifies the isotropic contribution as $\frac{d^2A}{d\gamma^2}\Big|_{0}$ is the large positive free energy curvature at the origin. Hence, if a very large anisotropic fraction, λ exists, the above expression becomes negative and local inhomogeneous chain deformation will occur. Otherwise, the expression becomes positive, thus no inhomogeneity and shear banding would exist. The values of free energy curvatures as well as λ fraction for different chain length and *Wi* are reported in Table 3-1. The aforementioned analysis is consistent with the aforementioned proposed mechanism, namely, during stress relaxation if orientation relaxation occurs locally due the low frequency of the retraction/rotation cycle, local inhomogeneity a prerequisite for shear banding is created. Otherwise, homogenous shear prevails.

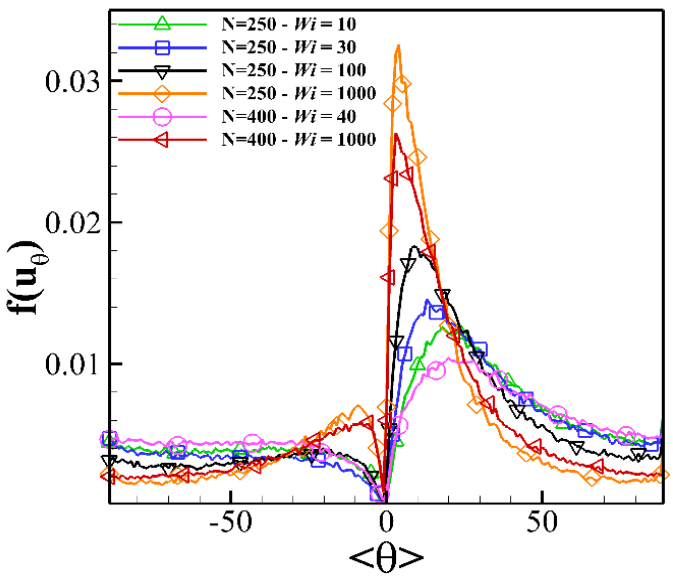

Figure 3-6. Primitive path segmental orientation distribution function at various *Wi* and chain length

Table 3-1.Calculated free energy curvatures at the origin and strain unit γ corresponding to stress overshoot as well as anisotropic fraction λ obtained from the area under the figure 3-6 curves for different step-strain simulations. Shear banding exists if equation-(3.2) becomes negative.

Step-strain	**γ**	$\frac{d^2A}{d\gamma^2}\|_0$	$\frac{d^2A}{d\gamma^2}\|_\gamma$	**λ**	**Equation –(3.2) sign**	**Shear banding**
***Wi* = 10, N=250**	2.0	0.09	- 0.04	0.6	> 0	No
***Wi* = 30, N=250**	2.05	0.092	- 0.06	0.62	< 0	Yes
***Wi*=1000,N=250**	4.5	0.1	- 0.07	0.57	> 0	No
***Wi* = 40, N=400**	2.04	0.08	- 0.06	0.56	<0	Yes

3.4.5 Effect of Deformation Ramping Rate on Shear Banding Occurrence

The inflection point corresponding to the stress-overshoot indicates the possibility of inhomogeneity; if the orientation relaxation occurs at a slow rate, i.e. only a few chain segments could relax their orientation prior to the steady state, thus local inhomogeneity originates. Motivated by this postulate, we have performed number of simulations by varying the time taken for the deformation rate to achieve its steady value to give orientation enough time to relax. The following results demonstrate the interrelation between chain orientation relaxation, presence of stress overshoot and formation of shear banded flow structure and corroborate the aforementioned mechanism discussed in preceding sub-sections.

Four different start-up simulations at *Wi* =30 are studied, step-strain start-up and three others are identified by the time over which the shear rate is ramped up to reach its final steady value; ramp-time = 2, 10 and 20 τ_d , i.e. it will take 2, 10 and 20 disengagement time to reach the final shear rate. Figure 3-7-(a,b) shows the shear stress evolution and free energy change per unit volume as a function of strain (time) for different ramp-times. The step-strain start-up shows a clear stress-overshoot. As the rate of ramping is decreased, the stress-overshoot is diminished and eventually, at ramp-time = 20 τ_d, it becomes negligible. As expected, the stress overshoot (the corresponding inflection point) appears at approximately 2 strain units and the steady stress value is identical for all cases. However, their corresponding velocity profiles shown in the inset at different times are significantly different for various ramp-times. Shear banding is observed for step-strain and fast start-

up (ramp-time=2 τ_d), while the linear velocity profile is maintained at all times for slow rate ramping, i.e. ramp-time = 10 and 20 τ_d. This finding clearly indicates that the temporal evolution of the velocity profile is a very sensitive function of the time scale over which the deformation rate is increased from zero to a given steady state value. Thus, shear banding is not a unique response of the flow at a specific shear rate even when the shear rate is in the region where the steady shear stress is a slight decreasing function of shear rate; rather its existence depends on the relaxation behavior of the entangled network. Our findings are in excellent agreement with Wang and coworkers' observations of monodisperse entangled DNA (Z=60) [115] and high molecular weight poly-disperse Poly-Butadiene solutions [116]. They have shown in both studies that shear banding can be eliminated if the shear rate is ramped up gradually, i.e. increasing the ramp-time. In the monodisperse entangled DNA experiment [115], the ramp-time = 12.82 τ_{d0} where shear banding is prohibited, τ_{d0} is the terminal relaxation time.

As the ramping rate decreases, the rotational time scale is reduced from 10.62 (step-strain) to 10.1 (ramp-time = 2 τ_d), 9.6 (ramp-time = 10 τ_d) and 7.4 (ramp-time = 20 τ_d). Therefore, the rotational frequency increases and orientation relaxation occurs more significantly before reaching the steady state. Also, we can express the characteristic behavior with a dimension-less number defined as r = τ_{rot}/ ramp-time = 5.05 (ramp-time = 2 τ_d), 0.96 (ramp-time = 10 τ_d) and 0.37 (ramp-time = 20 τ_d). If r > 1, local inhomogeneity exists, otherwise, orientation finds sufficient time to relax prior to the steady state, chains disentanglement occurs globally and homogeneous shear prevails. Moreover, the primitive path segmental orientation distribution function is depicted in

Figure 3-8. The isotropic fraction, (1-λ) increases as the ramp-time increases indicating that rotation takes place more effectively. On the other hand, in the anisotropic faction of the distribution function, the global maximum associated with the positive orientation angle declines and the local maximum corresponding to negative orientation angle grows as the ramp-time increases. As mentioned in earlier in sub-section 3.4.3, the positive maximum specifies the fraction of the chains segments that are well-oriented and stretched in the direction of the flow, while the negative maximum defines the chains segments with orientation along the vorticity direction leading to the formation of folded configuration. Thus, the significant drop of the positive maximum and considerable grow of negative maximum in the anisotropic fraction reveals that rotation cycle is accessible by more chains if the ramp-time is increased. The values of λ and free energy curvature for different start-up simulations are shown in Table 3-2 and their values fulfill the equation 3.2. Ultimately, as the ramp-time increases from step-strain to 20 τ_d, the flow-induced chain disentanglement occurs at a commensurate time scale as the rotation/retraction (see Figure 3-9-a) process leading to homogenous chain entanglement density distribution, i.e. homogenous chain deformation along the velocity gradient direction shown in Figure 3-9-b.

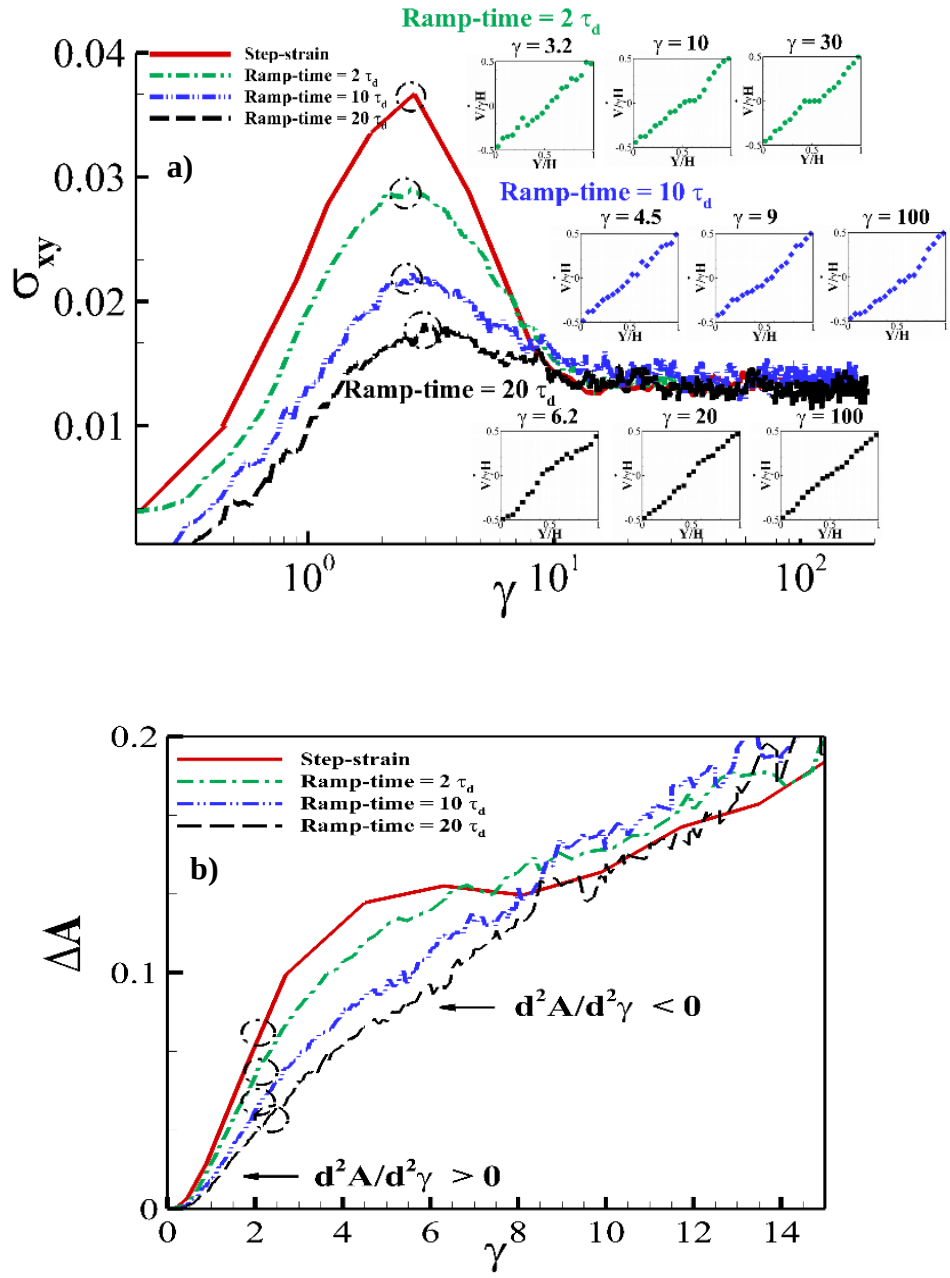

Figure 3-7. (a) Shear stress evolution as a function of strain and velocity profiles at various strain units shown in the figure inset and (b) free energy vs strain for different ramp-time simulations.

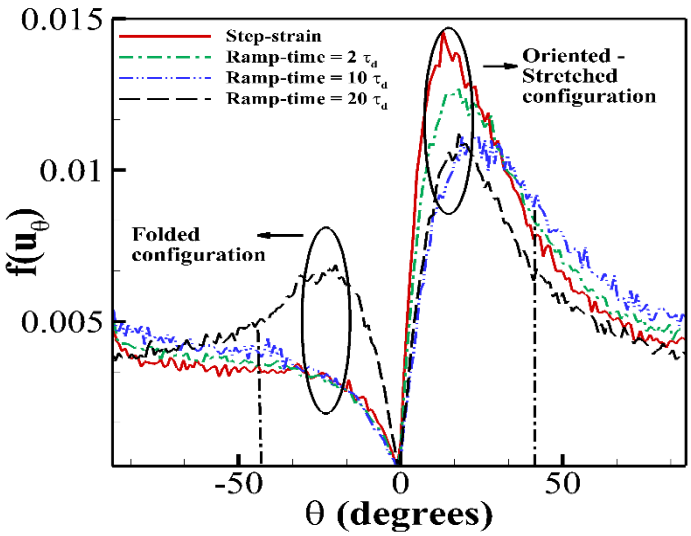

Figure 3-8. Primitive path segmental orientation distribution at various ramp times.

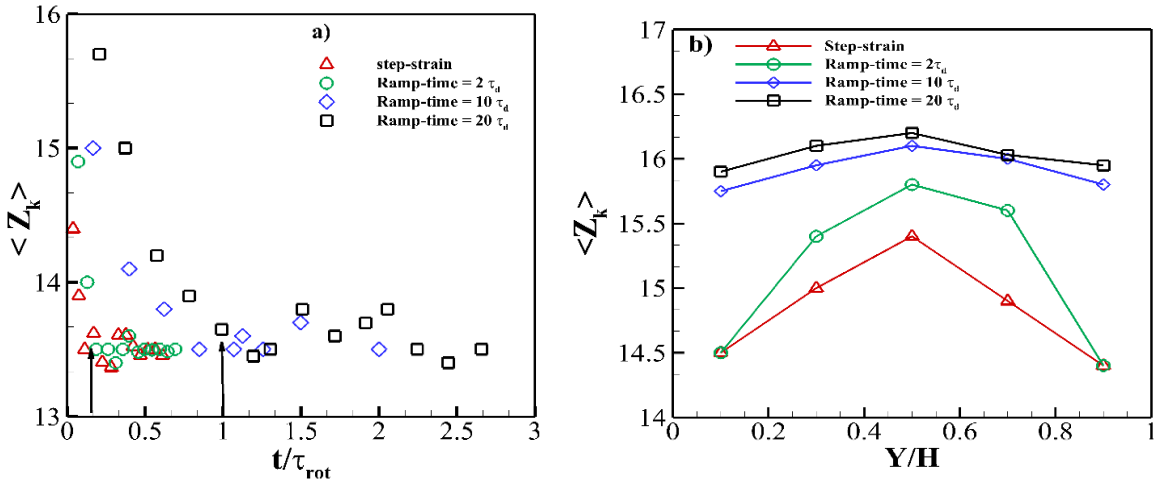

Figure 3-9. Average number of entanglements (a) as a function of time and (b) along the velocity gradient direction Y, at different ramp times. Y is scaled by the simulation box length, H.

Table 3-2. Calculated free energy curvatures at the origin and strain unit γ corresponding to stress overshoot as well as anisotropic fraction λ obtained from the area under the figure 3-8 curves for different start-up simulations. Shear banding exists if equation-(3.2) becomes negative.

Start-up (*Wi* =30)	γ	$\frac{d^2A}{d\gamma^2}\|_0$	$\frac{d^2A}{d\gamma^2}\|_\gamma$	λ	**Equation -1 sign**	**Shear banding**
Step-strain	2.05	0.091	- 0.06	0.62	< 0	Yes
Ramp-speed=2 τ_d	2.1	0.051	- 0.039	0.585	< 0	Yes
Ramp-speed=1 τ_d	2.1	0.0246	- 0.015	0.521	> 0	No
Ramp-speed=20 τ_d	2.2	0.015	- 0.006	0.591	> 0	No

In this section, we have elaborated the effect of rate of ramp up on the formation of local inhomogeneity and shear banding. The molecular level results show that no shear banding has been observed for the slow ramping, ramp-time = 10, 20 τ_d, however shear banded structures emerge for the case of fast start-up simulations, step-strain and ramp-time = 2 τ_d. The mechanism is as follows, if the chains segments have enough time to relax their orientation at the same time scale of stretch relaxation, rotation takes place globally, thus no inhomogeneity would arise. Otherwise, inhomogeneous deformation and further locally inhomogeneous entanglement density will exist along the velocity gradient direction leading to shear banding.

3.5 Conclusion

Motivated by the MG [114] postulate, we have investigated the stress relaxation and free energy analysis in details. Thus, step-strain and start-up simulations in entangled

polymer melts with different entanglement densities and ramp-times were performed. It is shown that the stress overshoot corresponds to the inflection point in the free energy suggesting the possibility of inhomogeneity. By further analyzing the stress relaxation process, it becomes discernible that orientation relaxation characteristic is the cause for the formation of local inhomogeneity. If rotation/retraction cycle occurs frequently, i.e. chains segments relax their orientation at the same time scale as stretch relaxation, no inhomogeneity would exist. Otherwise, local inhomogeneous chain deformation and disentanglement forms when rotation time scale is large and orientation does not relax sufficiently prior to the steady state.

In addition, the effect of deformation rate ramp-time on the stress overshoot and shear banding occurrence corroborate our proposed mechanism. As the ramp-time is increased, not only the stretch relaxation is delayed, so is the stress-overshoot diminished and shear banding disappeared. Primarily, with increasing the ramp-time, the chains segments have enough time to relax their orientation before reaching the steady state, rotation takes place globally and thus no inhomogeneity would arise.

Overall, the creation of local inhomogeneity formation, prerequisite for the formation of shear banding has shown to be a function of chain relaxation behavior over time (after stress-overshoot, prior to the steady state). Our findings are in perfect agreement with various step-strain and start-up experiments and consistent with MG postulate [114].

Chapter 4

Molecular Processes Leading to shear Banding

This Chapter is based on the published and submitted papers.

"Molecular Processes Leading to shear Banding in Well Entangled Polymeric Melts," M. Mohagheghi and B. Khomami, *ACS Macro Lett.* **4**, 684-688 (2015).

"Elucidating the Flow-Microstructure Coupling in Highly Entangled Polymer Melts: Part II. Molecular Mechanism of shear Banding," M. Mohagheghi and B. Khomami, *Journal of Rheology*, invited paper, JOR-15-327-SB.

4.1 Introduction

In this chapter, we report simulation results that describe the progression to macroscopic shear banding in well-entangled polymer melts. Specifically, during stress relaxation in a typical start-up setting, spatially inhomogeneous chain disentanglement in the velocity gradient direction acts as an intermediate step between a stress overshoot and the development of a banded velocity profile. We have performed hi-fidelity coarse-grained DPD simulations as described in Chapter 2 in a broad range of system sizes (various box sizes) and two entanglement densities, $\langle Z \rangle = 17$ and 27, to determine the critical conditions for occurrence of both transient and steady shear banding. The development of spatially inhomogeneous chain disentanglement as a result of local inhomogeneous chain deformation and the stability of steady and transient shear banded flows based on the well-known interfacial stability mechanism of stratified polymeric fluids are elucidated.

Overall, the progression to shear banding in highly entangled polymeric fluids based on the one to one correspondence between flow-induced micro-structural evolution and fluid rheological properties is elaborated specifically in section 4.3.

4.2 Local Process of Inhomogeneity Formation: Number of Entanglement Gradient

Here, we discuss the local process for the formation of local inhomogeneity and further in the following section explain its evolution to the incipient shear banded structure.

The local perturbations are observed for the first time at $t = 0.4\ \tau_d$ (see velocity profiles in the inset of Figure 4-1-(a)). In order to study the origin of this perturbations, we have investigated the entanglement network behavior at the step-strain (shear banding is present) and slow (ramp-time= $20\ \tau_d$) start-up (shear banding is absent) of *Wi*=30 over $0.25\ \tau_d \leq t \leq 0.4\ \tau_d$ where the stress-overshoot occurs at $t = 0.2\ \tau_d$. Various number of equal sub-volumes has been examined. Here the three main regions labeled as lower, middle and upper regions are discussed since they provide more meaningful statistical and physical results.

Chains primitive path movements in the upper and lower regions of the box are less restricted and their disengagement from the original tube is much faster as compared to the chains in the middle region. This point is evident from the primitive chain center of mass diffusion coefficient, D_G = 5510, 4910 and 8137 (r_c^2/τ_d) respectively in the lower, middle and upper regions (in step-strain experiment). As shown by Doi and Edwards $D_G \propto \frac{kTa^2}{N^2\xi}$ when the tube diameter gets larger, the chain diffusivity is enhanced. Also, chain disengagement can be triggered by “higher kinetic energy” in the boundary regions. Thus,

the chains in the boundary regions relax their orientation faster and "the chain disentanglement rate" is larger in the aforementioned regions while chains in the middle cannot relax their orientation as rapidly as the higher kinetic energy region. Hence, the local criterion for the formation of inhomogeneity is provided at a time after stress overshoot when the chains in the two adjacent regions disengage and relax their orientation on a different time scale, therefore inhomogeneity forms in deformation and a commensurate interface between the two aforementioned regions is created. To determine the location of inhomogeneity or the interface, we have looked at the number of entanglement points (different from number of entanglement per chain; time averaged over $0.25\ \tau_d \leq t \leq 0.4\ \tau_d$) over the X-Z and X-Y plane. The number of entanglement points in each cell is counted. It is clear from the X-Y contour shown in Figure 4-1(b) that asymmetry in the entanglement distribution exists at y = 8 and 32 r_c (box length in y dimension is 42.0 r_c). These two positions correspond to the locations in Figure 4-1(a) velocity profile inset at $t = 0.4\ \tau_d$ where velocity perturbations are observed. The entanglement distribution for ramp-time = 20 τ_d is shown in Figure 4-1(c) averaged over $3 < \gamma < 5$. The gradient of entanglement along the y direction in the case of ramp-time = 20 τ_d is smaller than the step-strain case as the dense contour lines suggest. The data points in Figure 4-1(b,c) indicate the position and level of each contour. We have checked various points in the vicinity of asymmetry in the entanglement distribution, the $\frac{\Delta Z}{\Delta Y}$ for the case of step-strain is larger than 3 and for the case of slow start-up (ramp-time = 20 τ_d) is smaller than 2. This point indicates that discontinuity in the number of entanglement needs to reach

a critical value, for inhomogeneity in deformation and a commensurate interface to form. The critical value based on our observation is three.

The X-Z entanglement contours for different regions (upper, lower and middle) of the box show similar behavior (see Figure 4-2). However, the number of entanglements is different in each region. Overall, the number of entanglements in the core of each region is highest and disengagement occurs from the tube ends. The orientation relaxation occurs at a higher rate in regions close to the boundaries and thus a discontinuity in chain disentanglement appears in the adjacent high and low kinetic energy regions and an interface between them is formed. Eventually, the lower and upper regions form the fast bands and the middle region becomes the slow band. If we consider the position of the interface at $y = \delta$ (the distance from the center of the box), δ is not randomly determined. Instead it is located between the boundaries and middle of the box and the location is a function of chain length (viscosity and elasticity), and shear rate in the stress relaxation regime. The interface is eventually stabilized when the viscous and elastic forces are balanced. It should be mentioned that in the entanglement network analysis (Figures 4-1and 4-2), the central box and along the adjacent boxes are considered to clearly count the number of entanglement points, the central box dimension is$100 \times 42 \times 42$ (r_c^3).

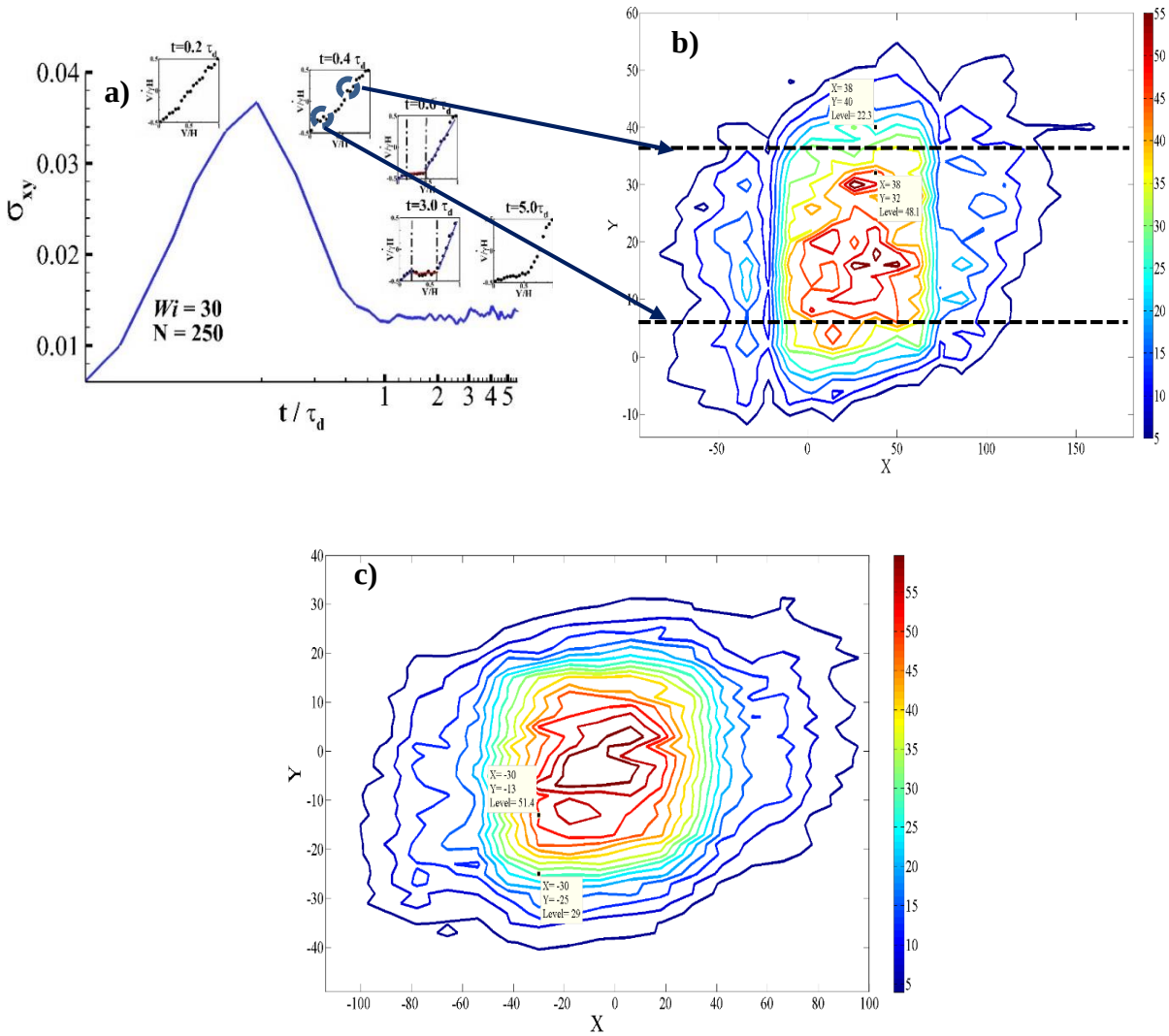

Figure 4-1. (a) Stress and velocity profiles of step-strain at Wi = 30, (b) Step-strain entanglement distribution in X-Y plane, (c) Contour plot of number of entanglements at ramp-speed =20 τd. The dashed lines indicate the interface between the adjacent regions. $\frac{\Delta Z}{\Delta Y} > 3$ and < 2 for step strain and ramp-speed =20 τ_d.

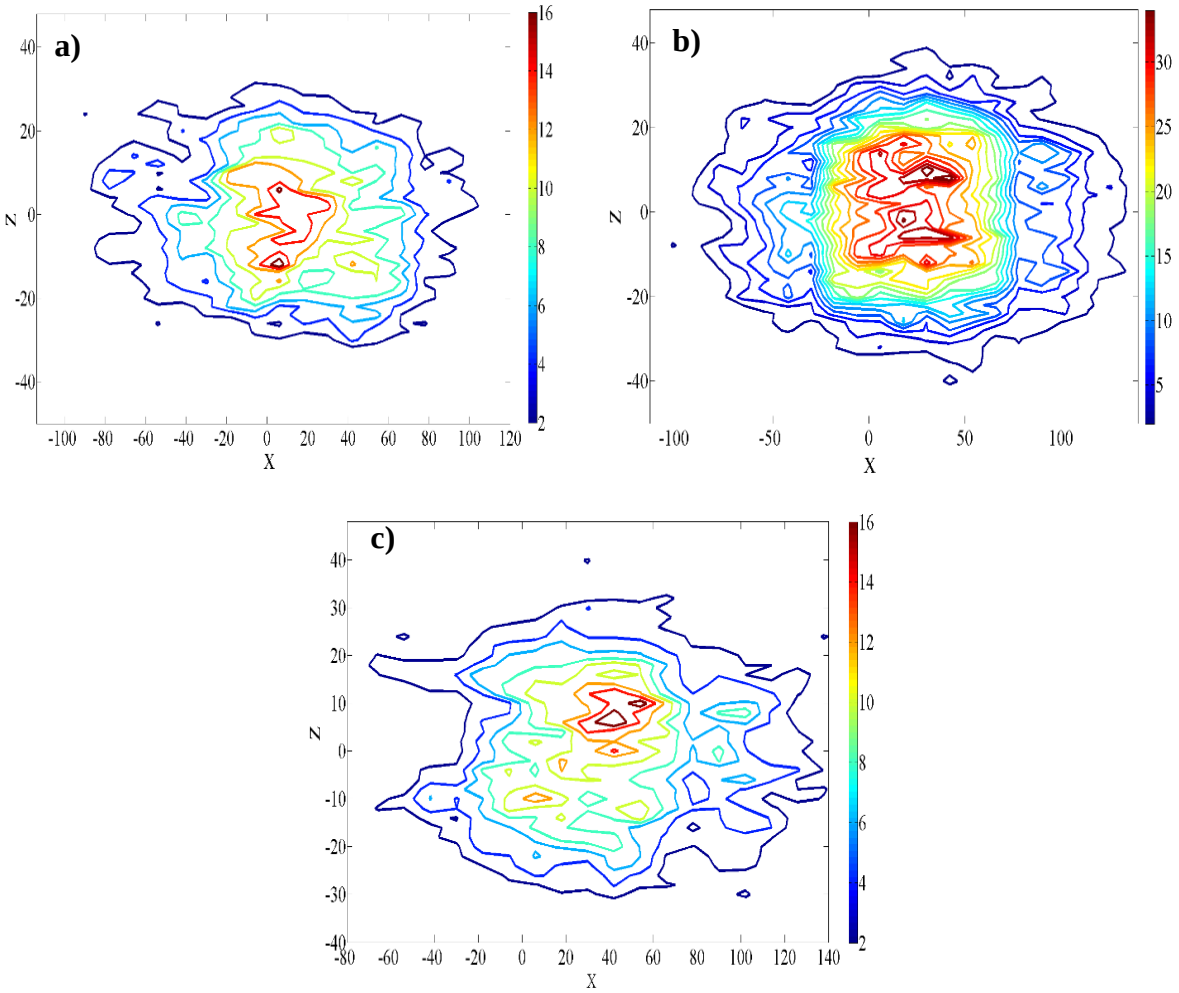

Figure 4-2. Number of entanglement points in the X-Z plane in (a) lower region (future fast band) (b) middle region (future slow band) (c) upper region (future fast band).

In summary, we have postulated in the preceding chapter a universal molecular criterion for the formation of local inhomogeneities in transient shear flows that relies on the large discrepancy between the stress and orientation time scale. In addition, the local process for the formation of shear bands is discussed as the different "chain disentanglement **rate"** between adjacent regions being large enough (here 3) as a result of different relaxation processes. Overall, if the orientation and stress relaxation is largely different, the orientation relaxation occurs "locally" and not globally accessible by all chains, thus the chain disentanglement rate becomes different in the adjacent regions, hence an interface and consequently inhomogeneous deformation is observed.

4.3 Inhomogeneous Chain Deformation and Disentanglement

In what follows, the molecular processes by which local inhomogeneities (discussed in the preceding chapter) created as a consequence of slow orientation relaxation in step-strain start of a planar shear flow evolve into shear banded flows is elucidated. To this end, spatially inhomogeneous chain deformation along the velocity gradient direction, i.e., the average chain extension and orientation angle with respect to the flow direction for three different *Wi* and chain length (N=250 *Wi*=30, N=400 *Wi*=40, N=400 *Wi*=1000), is carefully examined (see Figure 4-3). Evidently, locally inhomogeneous deformation of the entangled network of chains occurs specifically in the vicinity of the stress overshoot $t \geq 0.2\ \tau_d$ and before $t \leq 0.4\ \tau_d$. Chain extension and alignment are more pronounced in the regions (close to the simulation box boundaries) that will eventually be occupied by fast flows (higher shear rates). The growth of the aforementioned spatial inhomogeneity leads to development

of significant inhomogeneous flow induced chain disentanglement along the velocity gradient direction as shown in Figure 4-4.

It should be noted that the averages depicted in this figure were constructed prior to observation of the incipient shear banded flow structure. Clearly, the topological characteristic of the entangled network along the velocity gradient direction is considerably different in absence of shear banding, i.e., homogeneous flow-induced disentanglement is observed in the velocity gradient direction (see results for N=250 at *Wi*=10 and 1000). A detailed examination of the chain entanglement density distribution function shown in Figures 4-5 further confirms this fact. Specifically, It is shown (Figure 4-5-(a-d) for N=400 at *Wi*=40) that the entanglement distribution function in the regions that eventually become slow and fast bands are distinct. This spatial inhomogeneity in the entanglement density distribution function and its average is observed at t ~ 0.3 τ_d (stress overshoot at t = 0.18 τ_d), but long before the incipient shear banded structure is observed at t ~ 0.5 τ_d. Overall, the aforementioned analysis clearly underscores the fact that spatially inhomogeneous flow-induced chain disentanglement occurs before shear banding is observed. Moreover, it is shown that the less entangled chains populate the faster velocity band, and the more entangled chains are within the slower band.

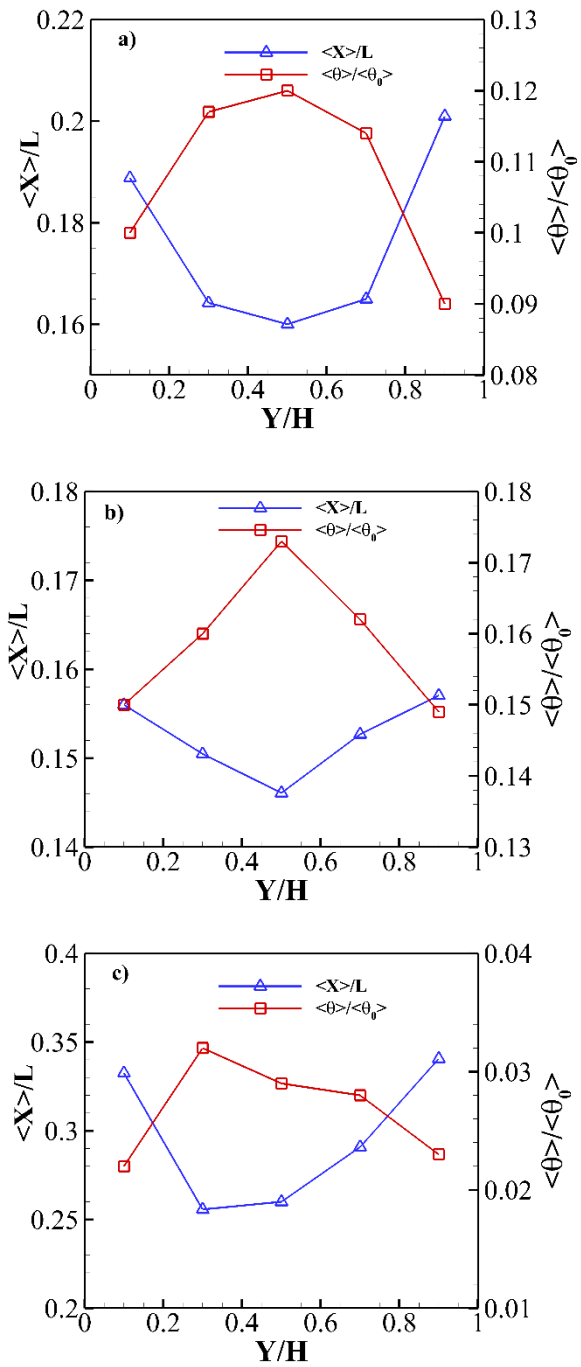

Figure 4-3. Plots of normalized chain end-to-end distance and orientation angle vs velocity gradient direction, Y for a) steady shear banding at Wi=30, N=250, b) steady shear banding at Wi=40, N=400 and c) transient shear banding at Wi=1000, N=400. L is the chain contour length and θ_0 is the orientation angle at equilibrium, i.e. 45°.

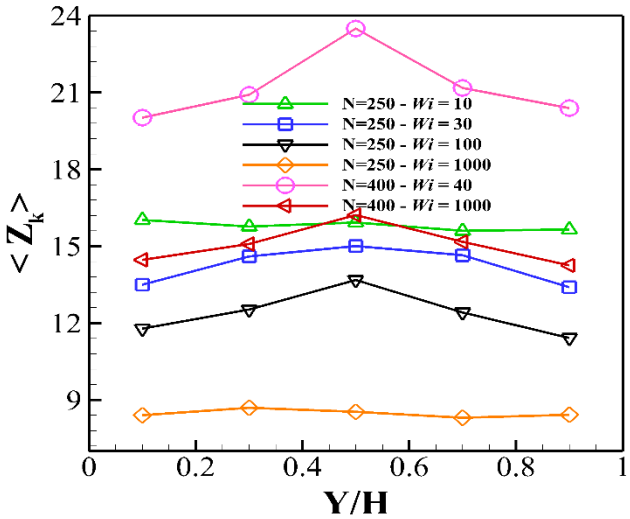

Figure 4-4. Average entanglement density as a function of velocity gradient direction, Y at various *Wi* and chain length. Y is normalized by the box side size, H.

It is a well-known fact in theories of flowing polymeric melts that entanglement density determines the viscoelastic characteristics of the fluid. To this end, it is not surprising to see that the aforementioned localized jump in entanglement density results in a pronounced jump in the first normal stress N1, and localized differences in viscosity along the velocity gradient direction. Figure 4-6 depicts prototypical temporal evolution of first normal stress in the aforementioned regions and its difference between the less elastic (slow band) and more elastic (fast band) bands for steady and transient shear banded flows. In general, due to the increased alignment of the chains in the shear direction during start-up, first normal stress rises in both regions. Moreover, based on a polymer chain configurational analysis, the chains with less entanglement are more aligned in the shear direction as compared to more entangled chains. Hence, the jump across the interface, i.e.,

$\Delta N1$ and the associated viscosity difference grows as a function of time before it reaches its steady state value. Specifically, after the stress overshoot, at around $t = 0.4\ \tau_d$, the localized jump in the entanglement density gives rise to a significant $\Delta N1$ and commensurate perturbations in the velocity profile. $\Delta N1$ is 13% and 33% of the average first normal stress ($\overline{N1}$) for N=250 and 400 beads respectively, and $10\% \times \overline{N1}$ for the transient shear banding case. The aforementioned localized non-uniform viscosity and elasticity difference give rise to a stratified shear flow or in the other words, the incipient shear banded flow.

Overall, the molecular mechanism leading to shear banding in entangled polymeric fluids can be summarized as followed. The inflection point in free energy at the point of maximum transient stress along with the slow orientation relaxation in a prototypical step-strain startup setting derives locally inhomogeneous chain deformation which in turn gives rise to the spatially inhomogeneous flow-induced chain disentanglement and a commensurate localized jump in normal stress and viscosity in the velocity gradient direction that leads to the incipient “stratified flow/ banded flow”.

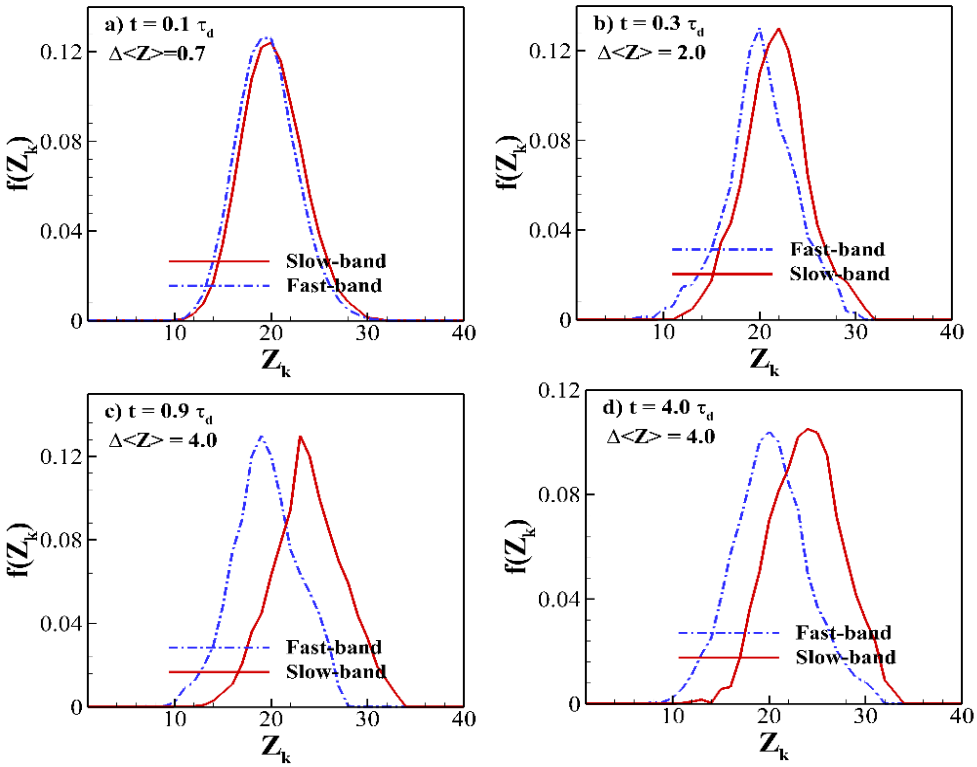

Figure 4-5. (a−d) Entanglement probability distribution function at different times for *Wi* = 40, N=400. The red and dashed blue lines, respectively, show the regions of the flow that are eventually occupied by the slow and fast bands; $\Delta Z = \langle Z \rangle_{\text{slow band}} - \langle Z \rangle_{\text{fast band}}$.

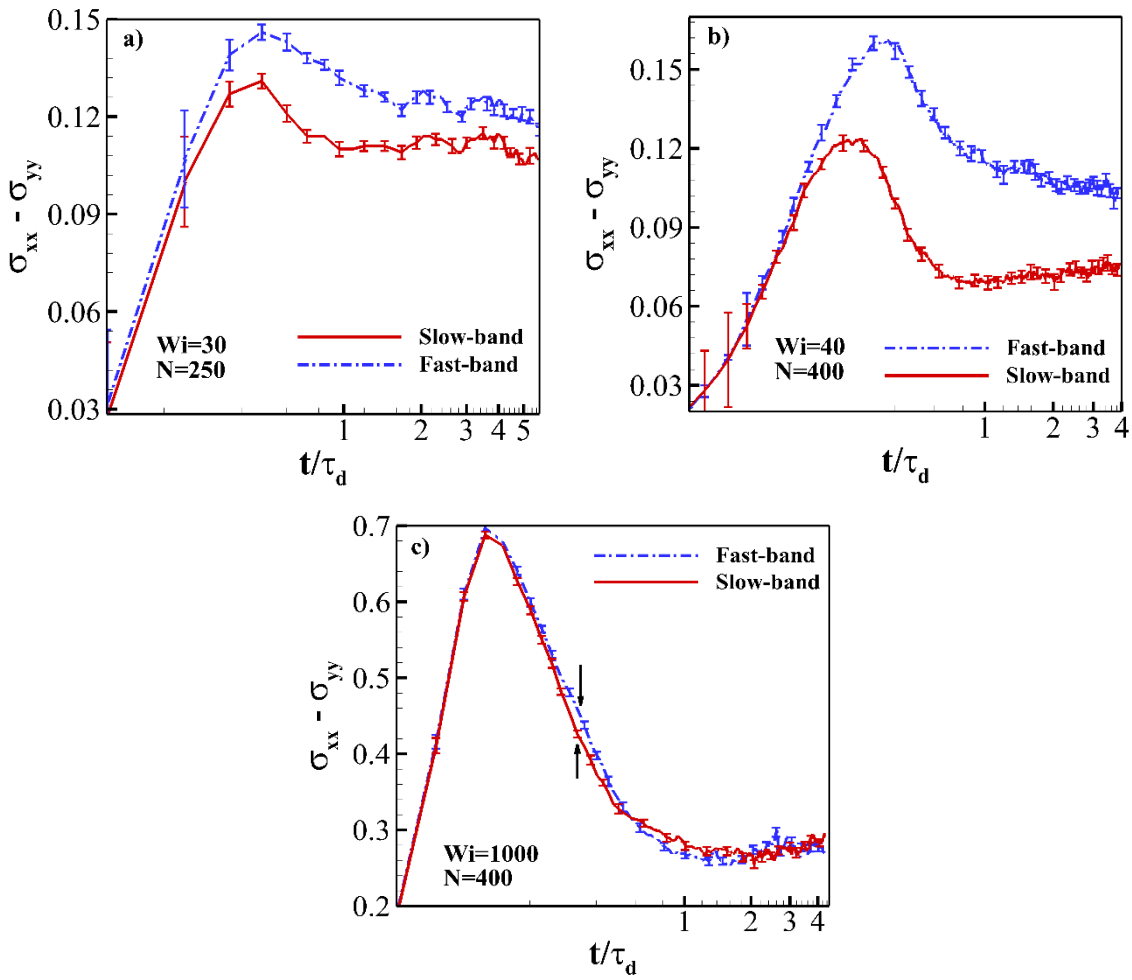

Figure 4-6. Temporal evolution of first normal stress for (a) steady shear banding at *Wi*=30, N=250, (b) steady shear banding at *Wi*=40, N=400 and (c) transient shear banding at *Wi*=1000, N=400. In the case of transient shear banding (c), the difference between the first normal stress in the slow and fast bands disappears at the steady state and hold its outmost value during the stress relaxation as shown by arrows. Time is normalized by the disengagement time at the applied shear rate. Time is scaled by the disengagement time at the applied shear rate.

4.4 Stability of Shear Banded Structures

Here, we propose a rationale for evolution of the incipient shear banded flow to a steady banded flow or to a linear velocity profile (transient shear banding) based on interfacial stability of stratified viscoelastic fluids. Specifically, we examine the interfacial stability of the incipient shear banded flow. To this end, we propose that if the stratified viscoelastic polymeric flow is stable to the interfacial disturbances, the bands will evolve and "steady shear banding" is realized. On the other hand, if the incipient banded flow structure is unstable, then interfacial perturbations grow in time leading to interfacial mixing of the adjacent layers. Thus, the localized jump in the entanglement density and fluid rheological properties gradually disappear (refer to Figure 4-6-(c)) and the stratified flow will revert to a linear velocity profile.

Assuming hydrodynamic modes are supported in our molecular simulations, in the limit of vanishing Reynolds number (Re) and negligible interfacial tension, the parameter space that determines the interfacial stability of stratified flow are stratification of viscosity and elasticity as well as the depth ratio. Specifically, in this class of flows two general role exists [18-20]: (1) when the less viscous fluid is thin, the interface is stable, the so called "thin layer effect" [20], and (2) when more elastic layer is the majority component, elasticity stratification is stabilizing [18]. Hence, one has to determine the relative importance of viscosity and elastic stratification to the overall stability of the interface. Fortunately, Su and Khomami [18, 117] have already performed a comprehensive continuum level study of the interfacial stability of stratified polymeric melts. Specifically, they have demonstrated that for depth ratios ($\varepsilon = d_{\text{more viscous}} / d_{\text{less viscous}}$) larger than 0.5 and

elasticity ratios ($L = N1_{more\ elastic}/N1_{less\ elastic}$) of order one, the viscosity ratio ($R = \eta_{more\ viscous}/\eta_{less\ viscous}$) should be larger than ~6 for the interface to be stable (for more detail, see figure 2-b in reference 113). Otherwise, the incipient stratified flow is short-lived and it returns to homogenous flow. Our observation of a steady and transient shear banded structure evolution is fully consistent with the aforementioned interfacial stability analysis; see Table 4-1 for values of ε, L and R.

Table 4-1. Depth, elasticity and viscosity ratios between the slow and fast bands for different step-strain simulations. The ratios are defined as ε = dmore viscous /dless viscous , EL = N1more elastic/N1less elastic and R = ηmore viscous /ηless viscous. Results are consistent with interfacial stability analysis.

Step-strain	**Depth ratio, ε**	**Elasticity ratio, EL**	**Viscosity ratio, R**	**Shear banding**
Wi=30 , N=250	0.8 <ε< 1	1.17 < EL < 1.3	9.5 < R < 13	Steady
Wi=40 , N=400	1 <ε< 1.8	1.3 < EL < 1.6	11 < R < 43	Steady
Wi=1000 , N=400	0.6 <ε< 0.66	1.06 < EL < 1.1	3.3 < R < 6.13	Transient

Chapter 5

Elucidating the Morphological Complexities of Linear Symmetric Triblock Polymer Thin Films

This Chapter is based on the published paper.

"Elucidating the Morphological Complexities of Linear Symmetric Triblock Polymers Confined between Two Parallel Plates: A Self-Consistent Field Theoretic Approach," M. Mohagheghi and B. Khomami, *Macromolecular theory and Simulation* **24**, 556-565 (2015). Featured on front cover.

5.1 Introduction

BCPs consist of two or more chemically distinct polymer chains (blocks) linked by a covalent bond. This class of soft material readily self-assembles into ordered structures with length scales ranging from 5–100 nm [22]. Size and shape of domains and the overall structural morphology can be controlled by judiciously manipulating the molecular weight and composition of the blocks. This set of attractive properties has led to widespread use of BCPs in many applications including membrane [27-29], photonic crystal [30-32], and several nanofabrication [23-26] applications.

Among the plethora of BCP applications, one that is rapidly approaching commercialization is microelectronic manufacturing. Traditional optical nanolithography, i.e., 30 nm feature size, cannot meet the growing demand for smaller feature sizes with increased surface/volume ratio. This technology gap is driving the need for a viable

technological alternative. Highly controllable, uniform, and inexpensive templates based on BCPs present such an alternative [33]. There is similar impetus in the magnetic recording industry to make smaller, denser, and more regular patterns leading to enhanced quality with increased information storage density.

Development of rational design and optimization strategies to guide specific self-assembled structures based on individual block properties is a critical step in translating bench-top synthesis protocols to large-scale fabrication techniques. To this end, simulation tools such as SCFT, MC, DDFT and DPD have been extensively used to examine bulk morphology development as a function of individual block properties. In addition, the influence of confinement on the morphology development of BCPs has been the topic of many studies [118-127]. In particular, the interplay between bulk and surface effects has been advantageously used to guide morphology development. However, due to the computational cost and large parameter space influencing the triblock phase behavior, most of the aforementioned studies have been limited to diblock copolymers, or two-dimensional [123-125] calculations for triblock polymers in limited range of surface energy. To this end, only a few systematic detailed studies have considered the effect of confinement on the morphology development of triblock copolymers.

In contrast to diblock systems, the phase behavior of ABC triblock terpolymers is much more complex and the parameter space is larger. In general, the parameters are: 1) $\chi_{AB}N$, $\chi_{AC}N$, $\chi_{BC}N$, f_A, f_B where χ_{IJ} is the Flory–Huggins interaction parameter between the monomers of type I and J, N is the degree of polymerization, and f_I is the volume

fraction of type I segments in the system; 2) film thickness, d, and 3) H_I is the interaction between top and bottom surfaces and component I.

To date, Chen and Fredrickson [128] have applied SCFT and strong segregation limit studies (SSL) to investigate the formation of microphases in thin films of cylinder-forming ABC triblock copolymer melts and have shown that the shape and orientation of minor A and C domains can be manipulated by adjusting the wall potentials and film thickness. Ludwigs et al. [127] have also used SCFT to model a system of compositionally asymmetric triblock terpolymers forming core-shell gyroid structure in the bulk phase. Specifically, they observed morphological transition via tuning the interaction parameters between the polymer components and the surfaces at different film thicknesses. Moreover, Pickett and Balazs [125] applied a two dimensional mean field to determine the equilibrium orientation of lamellar planes when triblock copolymer melts were confined between two plates. They considered two wall potentials, neutral and a very repulsive polymer-surface interaction. Their findings indicate that the perpendicular lamella morphology is achieved at the two extreme values of surface energy.

In the present chapter, we have utilized a three dimensional SCFT approach to model symmetric ABC triblock terpolymers confined between two parallel rigid walls. Specifically, extensive simulations have been performed over a broad range of film thickness and surface energy in which walls have identical interactions and are attractive to the middle block, while the interaction parameters between the blocks are taken to be the same, i.e., $\chi_{AB} = \chi_{AC} = \chi_{BC} = \chi$. Moreover, the relative stability of parallel and perpendicular lamella and cylindrical morphology as well as the phase diagram of the

aforementioned triblock system is discussed based on a minimum free energy calculation. It is shown that the $L_{\perp}$ and parallel cylinders, $C_{\parallel}$ are the stable morphologies over a wide range of surface interaction and film thickness. Also, at well-defined film thicknesses and strong surface interaction, metastable structures $C_{\parallel}$ (parallel cylinder) and PL (perforated lamella) coexist, however, perpendicular lamella and cylinder $L_{\perp}$ and $C_{\perp}$ form the stable morphologies. Specifically, to provide a more comprehensive picture of lamella orientation, relevant morphologies formed in diblock thin films are also shown for comparison purposes. In addition, the comparison between simulated triblock equilibrium morphologies and experimental observations is discussed in great details.

Overall, we have demonstrated the influence of film thickness and surface interaction to direct the perpendicular lamella and cylindrical morphology. Thus, a through rationale for realization of this highly sought after structure is provided herein.

The remainder of this chapter is organized as follows. In the following section, we discuss the SCFT numerical approach. In turn, the results of triblock copolymer lamella and cylindrical thin films are presented.

5.2 Self-Consistent-Field Theory

In our computations, we have applied SCFT in real-space following the procedure developed by Drolet and Fredrickson [129, 130] as a screening tool for the self-assembly of ABC linear triblock polymer thin films. In what follows, system parameters, governing equations, and the numerical implementation of SCFT are briefly discussed. If n_C is the number of polymer chains, V is the volume of the system, each polymer is built of N

monomers of type K=A,B,C, and each monomer occupies a volume of $1/\rho_0$, then the dimensionless segment density of type K monomers is given by,

$$\widehat{\emptyset_K}(r)=\frac{N}{\rho_0}\sum_{\alpha=1}^{n_c}\int_0^1 ds\ \delta(r-r_\alpha(s))\theta_K(s) \tag{5.1}$$

where α is the chain index, $0 \le s \le 1$ is the contour parameter along the polymer chain scaled by N, the A block belongs to $0 \le s < f_A$, the B block corresponds to $f_A \le s < f_A + f_B$, and the C block corresponds to $f_A + f_B \le s \le 1$, and

$$\theta_K = \begin{cases} 1 & \textit{if s belongs to block K;} \\ 0 & \textit{otherwise.} \end{cases}$$

The total segment density in the bulk of the system equals ρ_0 and vanishes on the confining walls. Therefore, we assume that dimensionless segment density rises from zero to the bulk value of one from each wall within a healing distance (ξ) which should be much smaller than R_g. Here $R_g = \sqrt{\frac{Na^2}{6}}$ is the unperturbed radius of gyration for an ideal Gaussian chain with N segments. Hence, the dimensionless total segment density is constrained to

$$\emptyset_0(r) = \sum_K \widehat{\emptyset_K}(r) = \emptyset_0(Z) \tag{5.2}$$

Previous studies of diblock copolymer thin films show that the detailed shape of ϕ_0 and wall potential W_{WK} and their change over the healing distance (ξ) do not affect the qualitative behavior of the system. Specific forms of ϕ_0 and W_{WK} adopted along with the film thickness are discussed below.

In mean field theory, each chain has independent statistics in an average chemical potential fields, $\omega_K(r)$, conjugate to average densities, $\phi_K(r)$, of block species K. The free energy per chain in units of k_BT is given by

$$\frac{F}{n_c k_B T} = -\ln\frac{Q}{V} + \frac{1}{V}\int dr \times \left[\sum_K\left(\sum_{M\neq K}\frac{\chi_{KM}N}{2}\emptyset_M - \omega_K + W_{WK} + P\right)\emptyset_K - P\emptyset_0\right] - \sum_K\sum_{M\neq K}\left(\frac{\chi_{MK}N}{2}f_M f_K\right) \quad (5.3)$$

Where Q is the partition function of a single chain in the chemical potential field ω_K and is defined as $Q = \int drq(r,1)$. The end-segment distribution q(r,s) shows the probability that a segment with contour length s is located at position r. Choosing the flexible Gaussian chain model and R_g as the length unit, the distribution q(r,s) satisfies the modified diffusion equation

$$\frac{\partial q(r,s)}{\partial s} = \nabla^2 q(r,s) - \theta_K(s)\omega_K(r)q(r,s) \;\; ; \quad q(r,0) = 1 \quad (5.4)$$

With the Dirichlet boundary condition at the confining walls where q = 0. Furthermore, q_C, the so-called complementary propagator satisfies an equation identical to Eq. 5.4 (with the

right side of the equation multiplied by -1 and the initial condition q_C (r,1) = 1 for all r and vanishes at the confining walls. W_{WK} is the block K-surface interaction, assumed to be short ranged. χ_{KM} is the Flory-Huggins interaction parameter between segments K and M, showing the incompatibility between blocks of the chain. Minimizing the free energy with respect to densities and chemical potential fields leads to the following SCFT equations:

$$\sum_{K\neq M} \chi_{KM} \emptyset_K = \omega_K - W_{WK} - P(r) \tag{5.5}$$

$$\emptyset_K(r) = \frac{V}{Q} \int_0^1 dsq(r,s) q_C(r,s) \theta_K(s) \tag{5.6}$$

P(r) is the Lagrange multiplier, i.e.,

$$\sum_K \emptyset_K(r) = \emptyset_0(Z) \tag{5.7}$$

The numerical implementation of the SCFT is realized as follows. The system is divided to $m \times m \times n$ lattice sites with grid size, $\Delta x = 0.2\ R_g$, on each side and the total number of chain segments is N=100. As mentioned earlier, the specific form of ϕ_0 and W_{WK} do not play a significant role in the qualitative behavior of the system; therefore, for simplicity, we use the following

$$W_{WK} = \begin{cases} H_K & \textit{on the adjacent lattice sites next to the wall;} \\ 0 & \textit{otherwise.} \end{cases}$$

$$\emptyset_0(Z) = \begin{cases} 0 & \textit{on the confining walls;} \\ 1 & \textit{otherwise.} \end{cases}$$

For a given H_K, f_K, and χ_{MK}, we solve the self-consistent equations (5.4–5.7) with the procedure explained further. Specifically, we start by generating random initial chemical potential fields ω_K at every point of the grid. Then for a given ω_K, we set the effective pressure P and solve the modified diffusion equation by the Alternate Direction Implicit (ADI) method for both q and q_C with the periodic boundary conditions in x and y directions and Dirichlet boundary condition on the confining walls, $q = q_C = 0$. In turn, the density profile is obtained through integration of equation 6 and the chemical potential fields ω_K are updated via the steepest descent algorithm until self-consistency is achieved. In all simulations, the surface interaction H_K is homogenous on the confining walls and favors the middle block (B segments). The strength of wall potential H_B varies between zero in the case of neutral walls to -35.0 and $H_A = H_C = 0$ for all runs. It should also be noted that extensive simulations were also performed with a smaller lattice cell size, i.e. $\Delta x=0.15\ R_g$; the results of these simulations were identical to those obtained with cell size, $\Delta x=0.2\ R_g$. Moreover, the box's size in x and y dimensions are optimized, thus the free energy does not change if the size of these sides gets larger, i.e. $\frac{\partial F}{\partial L} = 0$, L = box size in x and y directions. However, the film thickness is a simulation variable affecting the free energy; clearly, the optimal film thickness can be determined from the minima of free energy diagram vs film thickness.

5.3 Parameter Selection

Our overall aim in this study is to provide rational design strategies for the development of perpendicular lamellae and cylindrical morphologies in confined triblock systems. It is a well-known fact that the phase diagram of BCPs is sensitive to the relative order of Flory's χ_{ij} parameters. However, the experimental data for the interaction parameter is very limited, particularly for triblock systems. Moreover, theoretical estimations via different methods including group contribution, random phase approximation (RPA) and Z-effect deviate from the relatively scarce experimental data [131]. Thus, the complications associated with obtaining reliable predictions of Flory parameters over a broad range of chemistries significantly hinders quantitative comparison between experiments and the theory for the most industrially relevant systems (for detailed discussion, see reference 44).To this end, we have chosen Flory parameters in the intermediate segregation limit with equal order ($\chi_{ij}N=35$) to mimic a broad range of chemistries. The choice of surface energies and their relative affinity to each block have also been motivated by the available experimental data. The specific parameters chosen for the diblock and triblock simulations along with prototypical experimental findings are described in the following sections.

5.4 ABC Triblock Copolymer Bulk Phase Self-assembly

Clearly, the triblock terpolymer phase segregation is richer that the diblock melt since its degrees of freedom is larger i.e., bulk degrees of freedom for linear ABC is 5 and 2 for diblocks. The linear ABC terpolymer phase diagram is shown in Figure 5-1 for various

volume fractions of the middle block where the end blocks hold identical volume fractions, $f_A = f_C$. Two cases for the interaction parameters are considered; (a) all Florry-Huggins interactions are the same, $\chi_{AB} = \chi_{BC} = \chi_{AC}$ and (b) the repulsion between the middle-end segments is stronger than the end-end blocks, i.e. $\chi_{AB} = \chi_{BC}$ and $\chi_{AB} / \chi_{AC} = 3$. If all interaction parameters are identical, i.e. $\chi_{AB} N = \chi_{BC} N = \chi_{AC} N = 35$, the morphology formed mainly depends on copolymer compositions. As shown in Figure 5-1, with volume fraction of the middle block f_B increasing, the following ordered morphologies appear successively: LAM $\longrightarrow$ Tetragonal cylinders (TET_2) $\longrightarrow$ Spherical domains. However, in case (b) where $\chi_{AB} N = \chi_{BC} N = 60$ and $\chi_{AC} N = 20$, the interaction energy plays a significant role in determining the equilibrium morphology and more complex structures including perforated lamella (PL) and netwrorks are formed. Clearly, the phase segregation of triblock terpolymer melt is rich, however, we only focus on the case where lamella and cylindrical structure forms and further explore the influence of confinement on the triblock copolymer morphology. Here, $\chi_{AB}N = \chi_{BC}N = \chi_{AC}N = 35$, in the case of lamella structure $f_B = 2f_A = 2f_C = 0.5$, and for cylindrical morphology, $f_B = 0.62$ and $f_A = f_C = 0.19$. Other MC [132], SCFT [133-135] and experimental studies[136, 137] also predict the formation of lamella and cylinder structure for similar set of parameters.

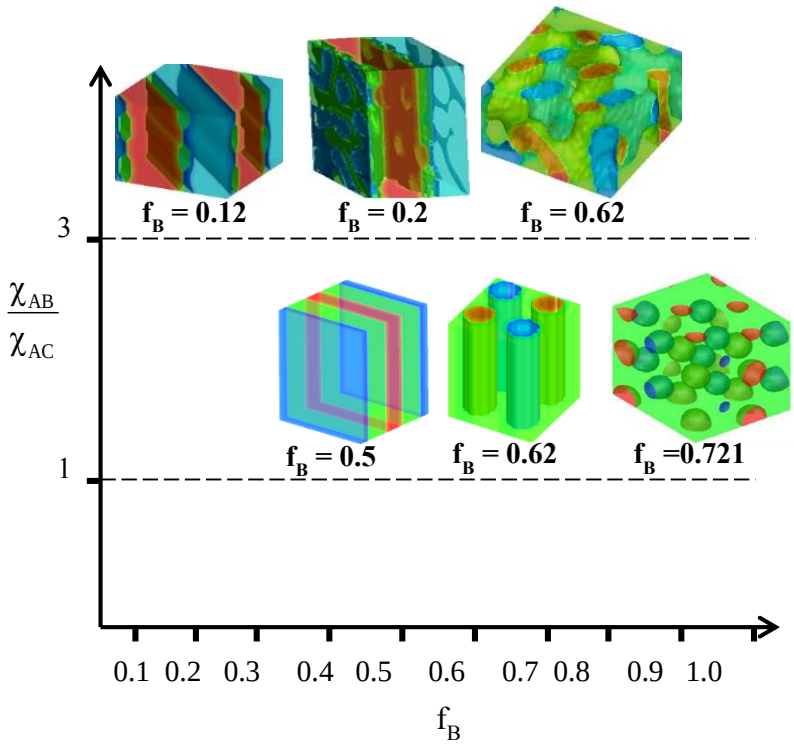

Figure 5-1. Bulk phase diagram of linear ABC triblock terpolymer melt as a function of middle block volume fraction and interaction parameters while keeping the end blocks' volume fractions identical, $f_A = f_C$. In the case $\chi_{AB}/\chi_{AC} = 1$, $\chi_{AB}N = \chi_{BC}N = \chi_{AC}N = 35$ and when $\chi_{AB}/\chi_{AC} = 3$, $\chi_{AB}N = \chi_{BC}N = 60$ and $\chi_{AC}N = 20$. The red, green and blue colors are assigned to A, B and C blocks, respectively.

5.5 ABC Triblock Lamella Thin Film Morphology

The middle block in triblock terpolymers are prone to exhibit a mixture of bridging and looping configurations. Hence, in confined systems with neutral surfaces, the middle block when placed adjacent to the surface cannot effectively bridge due to unfavorable entropic effects. The end blocks on the other hand, hold broader segment distribution close to the surface compared to the middle block, thus they lose less entropy[138]. Therefore, from an entropic point of view, end blocks prefer to be adjacent to the substrate surface(s) thus leading to parallel orientation in the lamella case. Motivated by these facts, we hypothesize that if the middle block B is chosen such that it has the lowest surface energy, this will lead to displacement of the end blocks, A or C from the wall region, thus facilitating formation of perpendicularly orientated lamella.

In order to explore the influence of confinement on the morphology development, the triblock polymers are confined in a channel with rigid parallel wall. The repeating stripes of A, B and C segments can either orient parallel or perpendicular to the walls. We consider the case in which both walls have identical interactions to each block. In turn, the film thickness is varied and the stable morphology is determined based on the free energy calculation. Furthermore, the surface energy interval is divided in to two parts, (a) $-15 \leq H_B \leq 0$ where wall interaction to the middle block is either neutral or weak discussed in sub-section 5.5.2 and (b) strong surface interaction $-35 \leq H_B \leq -20$ presented in sub-section 5.5.3.

5.5.1 AB diblock lamella Thin Film Morphology

A limited number of AB diblock morphologies are shown in this section to facilitate the comparison between triblock and diblock thin film equilibrium configurations. Specifically, the simulations target common experimental settings where the sample is localized between two rigid plates or when the copolymer is spun cast onto a solid substrate (top surface is exposed to air). The SCFT system specifications as well as prototypical experimental conditions are summarized in Tables 5-1 and 5-2, respectively. In particular, three cases were considered: a) two neutral surfaces (H_A= H_B= 0), b) homogenous surfaces where both walls attract the B block and are neutral to A segments, (H_A= 0, H_B=-2), and c) heterogeneous surfaces, where the bottom surface interaction to the B segments is attractive (H_B= -2) and the top surface is neutral to both blocks. The perpendicular lamella is stabilized over a wide range of film thickness, when both surfaces are neutral (see Figure 5-2-(a)). This result is consistent with experimental observation of the symmetric PS-PMMA thin films [139] that has been annealed on ITO substrate. XTEM images reveal that PS-PMMA assembles into perpendicular lamella when spun cast onto neutral substrates (either ITO glass or random copolymer P(S-r-MMA) anchored substrate). For the case of homogeneous surfaces, both perpendicular and parallel orientations exist at different film thicknesses. Symmetric parallel layers where the B block coats both surfaces is the stable morphology only for film thicknesses that are integral multipliers of lamella period (see Fig5-2-(b)). However, the parallel morphology is the preferred orientation over the entire film thickness in case c, i.e., heterogeneous surfaces, even for a very small value of surface energy, H_B= -2. Identical result has been found in the cross-section TEM Images

of PS-PMMA films [140] on the silicon wafer substrate coated with native-oxide layer while air forms the neutral surface at the other interface. The strong interaction between the polar block, PMMA and the substrate directs the parallel orientation. In summary, any surface interaction destabilizes the perpendicular orientation in diblock thin films. Though the neutral substrate can be created experimentally by adjusting either the surface chemistry of the substrate or by carefully tuning the properties of the copolymer components A and B, it is a costly task. Hence, an alternative solution to realize a lateral pattern is to exploit ABC triblocks thin films. In the next section, we show if the middle block B is chosen appropriately, the perpendicular orientation can be stabilized.

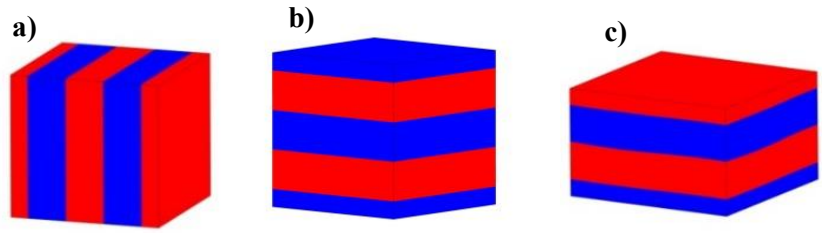

Figure 5-2. Equilibrium lamellar morphology of AB diblock copolymer melt confined between (a) two neutral substrates, (b) two homogenous surfaces: both surfaces prefer B segments, (c) Heterogeneous surfaces: bottom substrate favors B block while top surface is neutral to both blocks. A and B blocks are depicted by red and blue colors, respectively.

It is worth noting that the film thicknesses reported in Table 5-2 correspond to the optimal film thickness of each morphology. In the other words, we gradually increase the film thickness until the minimum free energy does not change, thus the free energy become independent of the film thickness and the reported morphologies are stable.

Table 5-1. Molecular Parameters for Prototypical Diblock Experiments. ([a,b]Data taken from references 139 and 140, respectively.)

Polymer	**M_W (g/mol)**	**f_{PS}**	**Substrate**	**d (nm)**	**Lamella orientation**
PS-PMMA[a]	—	0.5	ITO glass	< 300	⊥
PS-PMMA[b]	25000-26000	0.52	Sio_x	135, 375	‖

Table 5-2.Summary of parameters used for thin film SCFT calculations of AB diblocks. Effective film thicknesses (d) used for parallel and perpendicular orientations; correspond to optimal film thicknesses.

substrate	**f_A**	**χN**	**d (R_g)**	**Δx**	**Δs**	**Lamella orientation**
Neutral	0.5	25	8	0.2	0.005	⊥
Homogeneous	0.5	25	8	0.2	0.005	‖
Heterogeneous	0.5	25	6	0.2	0.005	‖

5.5.2 Directed Self-assembly with Weak Surface Interaction

$-15 \leq H_B \leq 0$: The relative stability of parallel and perpendicular morphologies as shown in Figure 5-3 are examined as a function of film thickness based on the excess free energy calculation, i.e., the energy costs to deviate from the bulk behavior (excess free energy = $\frac{(F-F_B)d}{nk_BT}$). Unlike study by Pickett and Balazs [125] where they set the potentials to only change in one direction; either normal or parallel to the walls, we start initially from three dimensional chemical potential fields corresponding to lamella morphology and calculate the free energy until convergence is achieved. Thus, based on the calculated free energy, relative stability of parallel to perpendicular morphology is evaluated. Figure 5-3 depicts the minimum free energy for the aforementioned microphases as a function of film thickness d with neutral walls; film thickness varies from $0.5L_0$ to $2L_0$ and for films with less than $0.5L_0$ thickness, disorder morphologies exist. The dashed parabolas correspond to parallel orientated films with confinement dimension equal to 0.5, 1, 1.5, and 2 times the bulk lamellar period. The solid horizontal line corresponds to the perpendicular orientation, which has a lower energy than the parallel cases. It should be noted that even if we start from random initial conditions at different film thicknesses, the perpendicular morphology is the stable structure with the same free energy as shown in Figure 5-3. Thus, we conclude that for neutral walls, the vertically oriented films form the stable structures and parallel configurations are the metastable morphologies at film thicknesses equal to integer or half-integer multipliers of bulk lamella period, i.e. 0.5, 1, 1.5 and 2 L_0. This result is similar to diblocks where perpendicular orientation is the stable morphology at all film

thicknesses for neutral walls. Identical to our finding, Müller et al. [141] have experimentally shown that the lamella exhibits an orientation perpendicular to the substrate over a broad range of film thicknesses, i.e., $0.01L_0$ to $4L_0$ when the symmetric P(pMS-b-Sd8-b-pMS) with $\chi N=29$ is spun coated onto the neutral Si(100) surfaces. On the other hand, when the attractive surface-middle block interaction, H_B is progressively increased from 0 to -15, the curves corresponding to the parallel phase energy move upward, while, the energy associated with the perpendicular morphology does not change significantly. Hence, the minimum free energy difference between parallel and perpendicular orientations, i.e., $\varepsilon = min(\frac{(F_{||}-F_{\perp})d}{nk_BT})$ also marked in Figure 5-3, grows as a function of surface interaction (see Figure 5-4). Therefore, the relative stability of perpendicularly oriented films is enhanced by preferential surface interaction. This finding is in contradiction to diblock structures where the perpendicular orientation is only stable for integer multipliers of L_0 for homogeneous surfaces as mentioned in the AB diblock section, case (b). In this range of wall potential, lamella morphologies with a wetting B-layer close to the wall do not provide stable structures. This is due to the fact that the surface interaction in this region cannot overcome the unfavorable entropic effects required for the looping configuration of the B block.

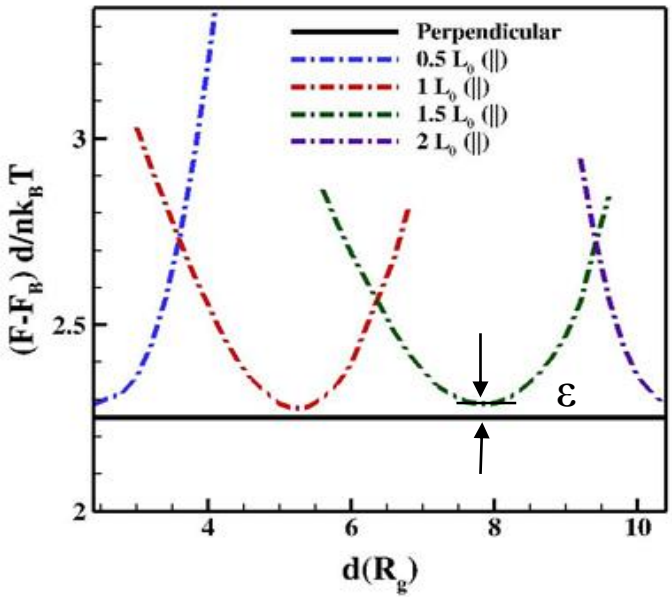

Figure 5-3. Excess free energy per unit area as a function of film thickness (d) for neutral wall. solid line: Perpendicular morphology, dashed curves: Parallel morphologies with 0.5, 1, 1.5,2 lamella layers from left to right respectively.

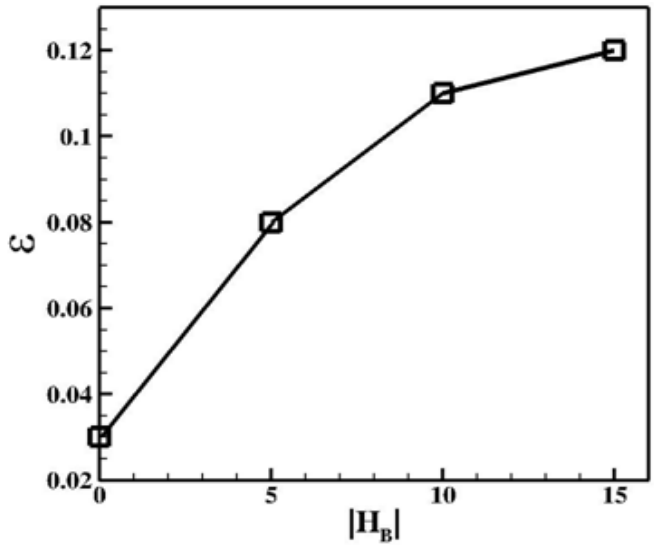

Figure 5-4. Minimum energy difference (ε) vs. wall potential (|HB|).

5.5.3 Directed Self-assembly with Strong Surface Interaction

$-35 \leq H_B \leq -20$: When the surface interaction is strong, surface wetting by the middle block is expected at all film thicknesses and a host of stable and metastable morphologies are observed as will be discussed shortly. We start from random initial chemical potential fields and various morphologies including parallel cylinders, perforated lamella and perpendicular lamella are obtained as a function of film thickness.

Parallel cylinders, $C_{||}$: The B block forms a thin confined layer near the walls at d < 3.2 Rg and minor A and C segments form cylinders oriented parallel with respect to the walls in the center of the film. The $C_{||}$ density profile and free energy of this configuration are shown in Figure 5-5-(a) and as a solid line in Figure 5-6, respectively. In addition, parallel cylinders in the matrix of the middle block also exist in the vicinity of d = 8.0 Rg as shown in Figure 5-5-(b). However, in the case of d > 3.2 Rg, this is a metastable morphology with its free energy slightly larger than the perpendicular lamella.

Perpendicular Lamella, $L_{\perp}$: As the film thickness increases, d > 3.2 Rg, the perpendicular lamella is the stable morphology. As shown in Figure 5-5-(c), the middle block B wets both surfaces and connects the two end caps of B and C segments and all the three vertical stripes of A, B and C blocks create the perpendicular lamella in the center of the film. This result is consistent with Elbs et al. [142] experimental observations in which they showed that P(S-b-2VP-b-tBMA) terpolymers form perpendicular lamella near the free surface and the middle block, i.e., P2VP coats the Sio_x substrate due to its strong interaction with the surface. The corresponding free energy of this morphology as a

function of film thickness is shown in Figure 5-6 as dashed line. Our findings are not consistent with those of Pickett and Balazs with strong surface interaction at large film thicknesses. Their specific choice of initial potential fields, slightly different volume fractions and two dimensional nature of their calculations is the main cause of the inconsistency.

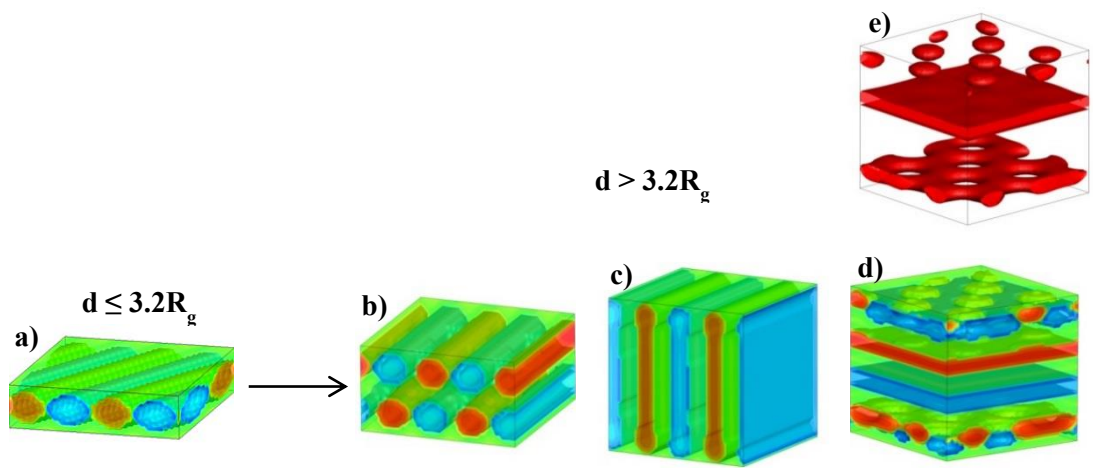

Figure 5-5. Density profile of triblock films. (a) $C_{||}$ morphology in which Red-blue domains represent A-C repeated morphology at d < 3.2 R_g, (b) Metastable $C_{||}$ at larger film thicknesses, (c) Stable perpendicular morphology showing the presence of all three A-B-C components in the middle of the film, (d) Metastable PL with parallel configuration in the bulk, (e) density profile for the A segments (regions where C_A > 0.7). A, B and C blocks are depicted by red, green and blue respectively.

Perforated lamella, PL: This metastable configuration appears at d > 3.2 Rg. As demonstrated in Figure 5-5-(d), parallel layers are in the bulk and the B block wets both the top and bottom walls. A perforated layer occurs close to the walls in which one of the end blocks segregates into regions with elliptic cross sections and the other end forms the

matrix, to better visualize this morphology, the density profile of the A segment (regions where concentration of A is more than 70%) is shown in Figure 5-5-(e).

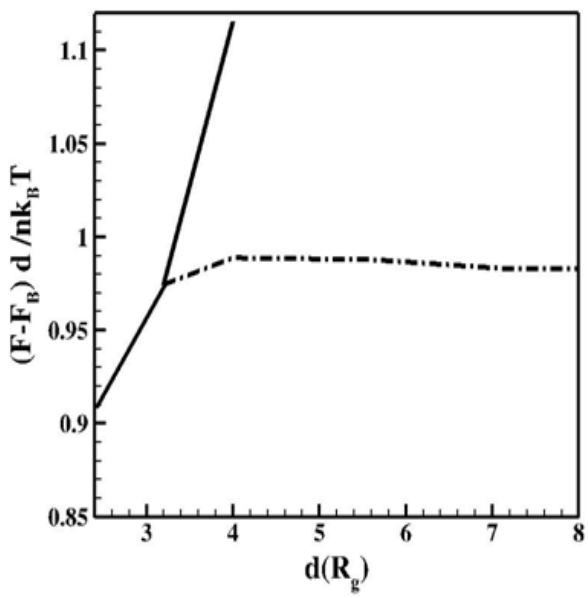

Figure 5-6. Excess free energy per unit area as a function of film thickness, d for wall potential, H_B= -20. **solid curve**: A and C blocks are present in the center of the film, **dashed line**: all three A-B-C blocks form perpendicular lamella in the center of the film.

The equilibrium morphologies of linear ABC triblock polymers have been discussed in earlier sections. In summary, the phase diagram for a linear triblock terpolymer melt is shown in Figure 5-7 as a function of film thickness and surface energy; along the stable structures, metastable morphologies are also depicted in the figure. The information for the aforementioned triblock experiments is briefly summarized in Table 5-3. Overall, it is shown that the perpendicular morphology is stable over a wide range of film thickness and

surface energies if the wall potentials are chosen such that they attract the middle block. Only at small film thicknesses and strong surface interaction, the parallel cylinders is the stable configuration.

5.6 ABC Tetragonal Cylinder Thin Film Morphology

We now focus on the case where A and C blocks form cylinders in the matrix of middle B block, and the system is confined between two hard, flat parallel plates. We will first analyze the relative stability of parallel and perpendicular morphologies in the neutral wall case. Due to the broad practical applications of perpendicular morphology, we will then suggest a strategy to stabilize this orientation.

When both substrates are neutral, there are two possible parallel arrangements, as shown in Figure 5-8-(a) and 5-8-(b).

The parallel orientation is preferred to the perpendicular one due to the negative line tension between the A-B, B-C interfaces and the confining walls. We hypothesize that if wall potentials are chosen to prefer B segments, parallel morphology I is less favorable due to the high elastic energy cost. Therefore, only perpendicular morphology and parallel morphology II are formed. Hence, preferential wetting can stabilize the perpendicular orientation. We choose $f_A = f_B = 0.19$ and identical Flory–Huggins interactions between blocks χ_{AB} N= χ_{BC} N = χ_{AC} N=35.0 to study the stability of the proposed morphologies.

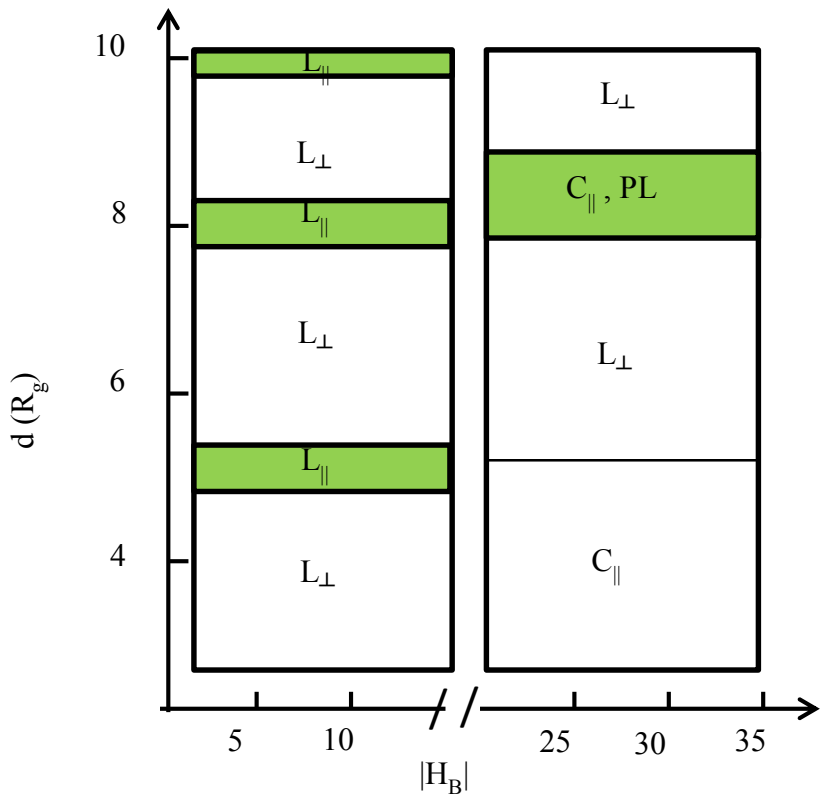

Figure 5-7. Influence of confinement, surface field and film thickness on linear triblock terpolymer morphologies. Both walls attract the middle block B while the end blocks' volume fractions are identical, $f_A = f_C$ and interaction parameters are the same, χ_{AB} N= χ_{BC} N= χ_{AC} N =35. The green rectangles demonstrate the metastable structures at certain film thicknesses

Table 5-3. Molecular Parameters for Prototypical Triblock Experiments. ([a,b]Data taken from references 141 and 142, respectively.)

Polymer	M_W (g/mol)	$f_{middle\ block}$	d (nm)	χN	substrate	Lamella orientation
P(pMS-b-Sd8-b-pMS) [a]	280000	0.51	0.54-216	29	Si	⊥
P(S-b-2VP-b-tBMA) [b]	110000	0.24	25	__	Sio_2	⊥

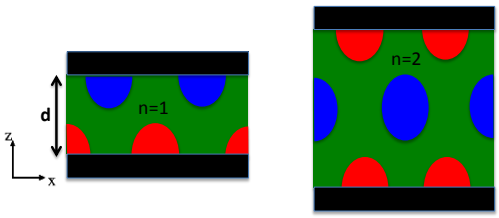

Figure 5-8. (a) Arrangement I: Cylinders represents minor A and C domains have elliptical cross sections. The system is translationally invariant in the y direction. n shows the number of layers in the z direction. In this arrangement, the same minor blocks (A or C) occupy the same row.

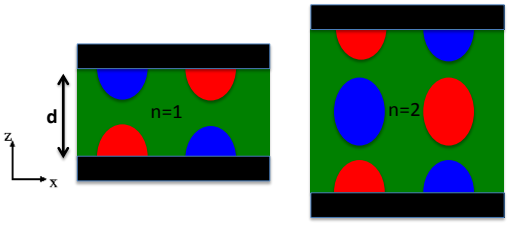

Figure 5-8. (b) Arrangement II: Cylinders represents minor A and C domains have elliptical cross-sections. The system is translationally invariant in the y direction. n shows the number of layers along the z direction. In this arrangement, both minor blocks (A and C) occupy the same row.

5.6.1 Directed Self-assembly with Neutral Wall

The SCFT free energies for all the aforementioned morphologies are plotted in Figure 5-9. The vertical axis corresponds to the excess free energy, the horizontal one is the film thickness in units of Rg. Parallel morphologies with various numbers of layers, and arrangements have lower free energies for a broad range of film thickness varying from $2.4R_g$ to $8R_g$. Next, we examine the condition leading to a stable perpendicular morphology.

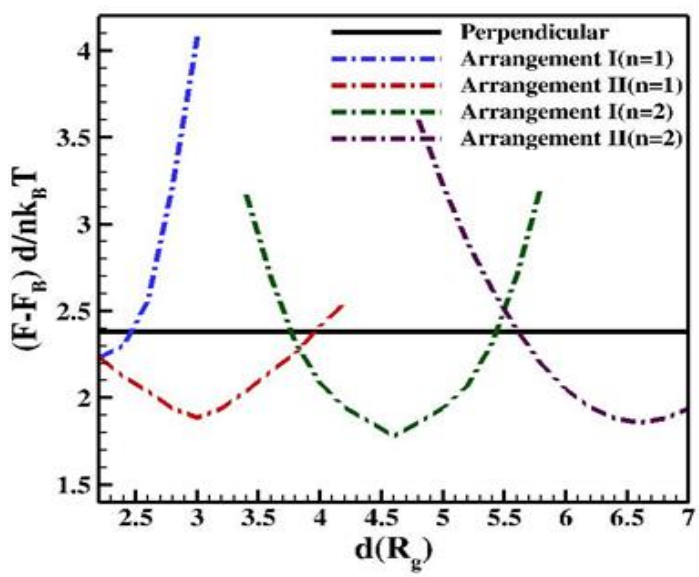

Figure 5-9. Excess free energy per unit area as a function of film thickness (d) for the neutral wall. solid line: Perpendicular morphology, dashed curves: Parallel morphologies labeled with the number of layers and type of arrangement.

5.6.2 Directed Self-assembly with Strong Surface Interaction

If the wall potentials are chosen such that the walls are in contact only with B segments, the parallel morphology II can be excluded and hence, the perpendicular morphology becomes stable for a broad range of film thicknesses. Figure 5-10 shows the free energy as a function of film thickness for H_B = -35.0 and $H_A = H_C = 0$.

These findings are consistent with an earlier study by Chen and Fredrickson [128]. It should be noted that the in-plane pattern of the film (XY plane) is tetragonal; in diblock thin films, a hexagonal pattern is observed [121], however. We also emphasize that the cylindrical morphologies associated with the lowest free energy have elliptical cross sections.

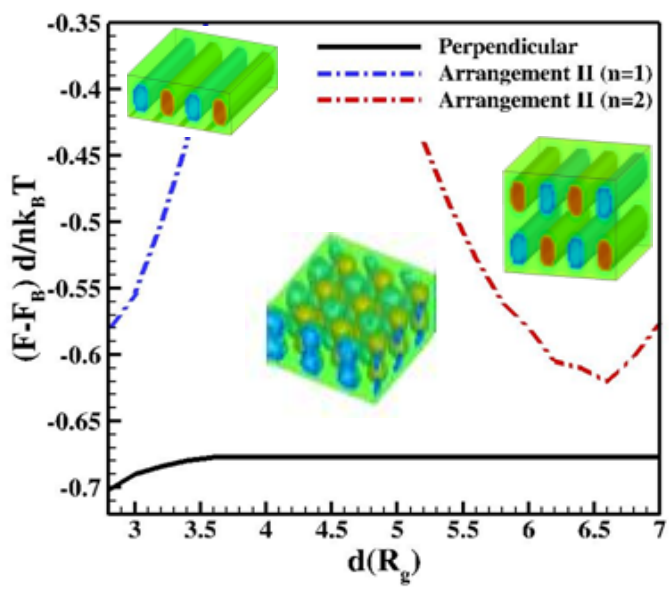

Figure 5-10. Excess free energy per unit area as a function of film thickness (d) for strong wall potential, HB= -35.0. solid line: Perpendicular morphology, dashed curves: Parallel morphologies labeled with the number of layers and type of arrangement.

5.7 Conclusion

Using 3D self-consistent theory, extensive calculations have performed on the self-assembly of symmetric triblock terpolymer melts confined between two parallel plates with homogeneous surfaces. The aforementioned results reveal that if wall potentials are strong and attractive to the middle block, perpendicular orientation is stabilized for both lamella and cylindrical structures for a wide range of film thickness. The observed metastable structures in the case of stable lamella morphology (perforated lamella, parallel cylinders) are not accessible in the bulk morphology of these systems. In fact, we identified this deviation from the bulk structure, both in the vicinity of surfaces and in the thin films of copolymers as a result of confinement effects. Also, in the case of triblock copolymer melts, the targeted perpendicular morphology is stabilized and can be controlled over long length scales by judicious manipulation of surface energy and film thickness. However, in the case of diblocks, the perpendicular morphology is destabilized in the presence of any surface interaction. This result shows that triblock copolymers are better candidate than diblocks for nano-lithographic fabrication. Overall, our findings demonstrate that the rational design of desired structures is viable through the proper choice of chain architecture, surface energy and film thickness.

Chapter 6

Conclusions

6.1 Entangled Polymeric Flow Behavior and Shear Banding Mechanism

Before the completion of this thesis, a number of important issues were subject of intense debate in the rheology community, namely precise determination of flow-microstructure coupling and occurrence of shear banding in flow of entangled polymeric fluids. In this work, I have developed a mesoscpic level, DPD simulation technique that allows high fidelity simulations of polymeric melts in a prototypical unidirectional flow (flow between two parallel plates), which has served as a paradigm for investigation of hydrodynamics and flow transitions in the complex fluids. The principal findings of this work can be used by both academic and industrial scientists/engineers to rationally design polymer processing operations. The aforementioned simulation technique has been used to elucidate the chain relaxation mechanism, flow-microstructure coupling, flow-induced chain disentanglement and shear banding in entangled polymeric fluids. It has been shown that vorticity excursion plays a significant role in orientational relaxation of macromolecules and the entangled network dynamics of these class of fluids. Also, the onset of shear banding depends on the shape of time-dependent rheological response function as well as flow relaxation behavior and is independent of fluid's constitutive law and internal state variables which has been traditionally believed to be the mechanism that gives rise to this phenomenon. Specifically, for the very first time, large scale DPD simulations (1374 chains corresponding to 549600 interacting beads) have been used to

investigate the molecular origin of the non-linear flow response of entangled polymeric fluids under flow conditions.

It has been shown through flow-microstructure coupling that 3 different regimes exists in the aforementioned class of flows. In weak flows or in the linear regime where shear rate is $\dot{\gamma} \leq \tau_d^{-1}$, reptation is the dominant relaxation mechanism. Beyond the linear regime, i.e., the non-linear viscoelastic regime, $\tau_d^{-1} \leq \dot{\gamma} \leq \tau_R^{-1}$, a variety of structural, rheological and topological properties are found to display significant deviations from their corresponding equilibrium behaviors; e.g., non-Gaussian shape of the probability distribution function P(|R|) of the magnitude |R| of the chain end-to-end vector, shear-thinning behavior of viscosity, and the rapid drop in the number of entanglements per chain. In fact, significant chain alignment and the onset of chain extension lead to flow-induced chain disentanglement and a commensurate tube dilation that leads to onset of vorticity excursion. Particularly, the shear thinning behavior and the notable decrease in the entanglement density with flow strength coincides with the onset of vorticity excursion, i.e. rotation/retraction cycle. Moreover, the wide (non-Gaussian) end-to-end distribution of polymer chain results from the broad configurationl diversity emerging from the structures in the rotation/retraction process. In the retraction/rotation cycle, the flow-induced aligned chain retracts from a stretched anisotropic configuration to an equilibrium-like structure (coil) and expands once more to assume a stretched configuration. In this regime, stress becomes nearly constant due to what is commonly referred to as convective constraint release, CCR. The third region appears at very large *Wi* where the entanglement network collapses and chains do not experience much resistance. In this regime, a peak

corresponding to chain sizes smaller than the equilibrium R_g of the polymer molecule appears in the chain end-to-end probability distribution function which indicates the existence of highly compact configuration. In addition, another peak corresponding to highly stretched structures exists in the chain end-to-end probability distribution function. The observation of two peaks in the probability distribution function is a clear hallmark of rapid vorticity excursions. Thus, the flow behaves similar to a semi-dilute polymer solution under theta solvent conditions, hence Rouse dynamics is the dominant chain relaxation mechanism. Therefore, 3 main relaxation time scales exists in the entangled liquids, Rouse time τ_R, reptation $\tau_{d,}$ and rotation (orientation) time scale τ_{rot}. The results of this study have provided the details of flow-microstructure coupling and the commensurate chain relaxation mechanism needed in modern tube constitutive models to rationally include CCR in macroscale.

In turn, the aforementioned DPD methodology was used to study non-linear phenomenon of shear banding. Specifically, steady shear banding was observed in the $\tau_d^{-1} \leq \dot{\gamma} \leq \tau_R^{-1}$, where the shear stress is a slightly decreasing function of shear rate. However, transient shear banding was observed at $\dot{\gamma} > \tau_R^{-1}$, where the flow curve is an increasing function of shear rate. In addition, excessive shear thinning behavior of viscosity of highly entangled polymeric liquids gives rise to a non-monotonic flow curve. The stress-overshoot that appears in start-up flows at 2 strain units for $Wi > 10$ has been shown to correspond to the inflection point in the free energy calculated via Doi-Edwards expression. It should be noted that the inflection point in the free energy indicates the possibility of strain rate inhomogeneity in the flow.

After the stress overshoot, i.e. during the stress relaxation regime (where the stress decays to its steady state value), chains mainly relax their stress in two steps; in the first step, tension is relaxed by segmental stretch relaxation, a very fast process; in the second step, chains relax their orientation which is a very slow process, i.e. an order of magnitude longer timescale is associated with the orientation relaxation mechanism than stretch relaxation. Specifically, the flow-induced anisotropic segmental configuration observed in stretched and flow aligned chains is relaxed to isotropic equilibrium-like chain structures (coil) via a rotation/retraction cycle, composed of various folded, half-dumbbell and dumb-bell configurations. It is shown that large discrepancy between the segmental stress/stretch (fast) and segmental orientation relaxation time scales (slow particularly compared to the time for the deformation rate to reach its steady state value) leads to local inhomogeneity in the entanglement network. Specifically, the combination of flow induced chain disentanglement and insufficient time for orientation relaxation leads to inhomogeneous entanglement density and a commensurate local variations in fluid properties in the velocity gradient direction that cause a flow transition, i.e., formation of deformation inhomogeneity. Hence, locally inhomogeneous chain deformation, which in turn gives rise to spatially inhomogeneous flow-induced chain disentanglement and a commensurate localized jump in normal stress and viscosity in the velocity gradient direction leads to the incipient “stratified flow/ banded flow”.

To further scrutinize the aforementioned molecular criterion for creation of local inhomogeneities, the time scale for ramping up the deformation rate from zero to its steady state value was adjusted such that chain stretch is delayed and orientation relaxation has

sufficient time to occur, hence, obviating the formation of the incipient shear banded structure. Indeed, as deformation rate ramp-time is increased from 2 to 10, and finally to $20\,\tau_d$, the stress-over shoot diminishes, velocity profile changes from a banded flow to a linear velocity profile and the retraction/rotation time scale is reduced from 10.1 to 9.2, and $7.4\,\tau_d$, respectively. Thus, the ratio between the retraction/rotation time scale to deformation rate ramp-times of 2, 10 and $20\,\tau_d$, i.e., $r = \frac{\tau_{rot}}{\text{ramp}-\text{time}}$ is decreased from 5.05 to 0.96, and 0.37, respectively. This decline in the ratio clearly shows that retraction/rotation cycle becomes more frequent and occurs globally prior to the system reaching its steady state value; hence, the main driving force for the formation of "local inhomogeneity" is suppressed and shear banding is eliminated. Hence, shear banding is not a unique response of entangled polymeric fluids to a specific shear rate, rather, it depends on the relaxation behavior of entangled network that is intimately related to r.

The stability of shear banded structures is rationalized based on interfacial stability analysis of stratified viscoelastic flows. When the stratified viscoelastic polymeric flow is stable to the interfacial disturbances, the bands will evolve and "steady shear banding" is realized. On the other hand, if the incipient banded flow structure is unstable, then interfacial perturbations grow in time leading to interfacial mixing of the adjacent layers. The stability of interface is determined based on the elasticity, viscosity and depth ratio. Specifically, it has been demonstrated that for depth ratios ($\varepsilon = d_{\text{more viscous}} / d_{\text{less viscous}}$) larger than 0.5 and elasticity ratios ($EL = N1_{\text{more elastic}} / N1_{\text{less elastic}}$) of order one, the viscosity ratio ($R = \eta_{\text{more viscous}} / \eta_{\text{less viscous}}$) should be larger than ~6 for the interface to be stable and thus the shear banded structure becomes steady.

6.2 Block Copolymer Directed Self-assembly

Using SCFT based simulations, it has been shown that there are a variety of 3-dimensional morphologies that can be produced from the self-assembly of triblock ABC terpolymer melts in bulk that possess the desired characteristics for potential application in nanolithography. The targeted morphologies were perpendicular lamella and cylinders, composed of two easily degradable blocks formed within a surrounding non-degradable matrix phase. The orientation and shape of morphologies can be tuned via varying the volume fraction of block polymer distinct segments, the interaction energy between the blocks, film thickness and surface energy between the blocks and the wall/surface. As a general guideline, the perpendicular morphology is stable in both lamella and cylindrical case if the surface interaction between the wall and the middle block, B is attractive and large. In this case, the strong surface energy between the block and the wall will compensate the entropic penalty for the loop configuration of the middle block. The middle block forms the matrix, wets the surface and the end blocks, A and C will form perpendicular morphologies. However, there are some exceptions to this general rule.

The perpendicular lamella self-assembly where A and C are the minor blocks with volume fraction of $f_A = f_C = 0.25$, is stable for neutral walls due to the negative line tension between the surface and the interface of A-B and B-C block copolymer microphases. The perpendicular orientation remains the stable morphology at intermediate surface interaction (walls attracts the middle block and are neutral to the end blocks). On the other hand, the parallel orientation becomes metastable at film thicknesses commensurate to the lamella bulk period. The aforementioned result for ABC triblock copolymer self-assembly

is in contrast with diblock copolymer melt confined between two plates. The perpendicular orientation is destabilized at integer multiplier of lamella period in the presence of any wall potential. Therefore, there is a clear advantage in utilizing the ABC triblock terpolymer melt to fabricate lithographic patterns.

Complicated morphologies including tetragonal horizontal cylinder and perforated lamella exist when surface interaction becomes large. At small film thickness, the tetragonal horizontal cylinder is the stable morphology. As the film thickness increases, the perpendicular morphology becomes stable and cylindrical and/or perforated lamella are the metastable structures. Overall, the perpendicular lamella occupies the majority of phase diagram if the walls attract the middle block and the volume fraction of end blocks are identical and equal to 0.25.

The parallel tetragonal cylinder is stable at all film thicknesses in the presence of neutral walls and identical end block volume fraction $f_A = f_C = 0.19$. The perpendicular cylinder becomes the stable morphology at large surface interaction where the middle block loops, forms a layer close to the substrates and the A and C blocks self-assemble into perpendicular cylinders in the matrix of B block.

Overall, triblock ABC can provide richer and more tunable structures due to their larger parameter space. Hence, they possess distinct advantage over diblocks as candidates for template production needed for a variety of applications.

List of References

1. Bird, R.B., et al., *Dynamics of Polymeric Liquids, Volume 2: Kinetic Theory*. 1987: Wiley.

2. Larson, R.G. and H. Brenner, *Constitutive Equations for Polymer Melts and Solutions: Butterworths Series in Chemical Engineering*. 2013: Elsevier Science.

3. de Gennes, P.G., *Reptation of a Polymer Chain in the Presence of Fixed Obstacles.* The Journal of Chemical Physics, 1971. **55**(2): p. 572-579.

4. Doi, M. and S.F. Edwards, *The Theory of Polymer Dynamics*. 1988: Clarendon Press.

5. Larson, R.G., et al., *Definitions of entanglement spacing and time constants in the tube model.* Journal of Rheology (1978-present), 2003. **47**(3): p. 809-818.

6. Rubinstein, M. and R.H. Colby, *Polymer Physics*. 2003: OUP Oxford.

7. Likhtman, A.E. and R.S. Graham, *Simple constitutive equation for linear polymer melts derived from molecular theory: Rolie–Poly equation.* Journal of Non-Newtonian Fluid Mechanics, 2003. **114**(1): p. 1-12.

8. Banchio, A.J. and J.F. Brady, *Accelerated Stokesian dynamics: Brownian motion.* The Journal of Chemical Physics, 2003. **118**(22): p. 10323-10332.

9. Sierou, A. and J.F. Brady, *Accelerated Stokesian Dynamics simulations.* Journal of Fluid Mechanics, 2001. **448**: p. 115-146.

10. Jain, A., et al., *Optimization of a Brownian-dynamics algorithm for semidilute polymer solutions.* Physical Review E, 2012. **85**(6): p. 066703.

11. Saadat, A. and B. Khomami, *Matrix-free Brownian dynamics simulation technique for semidilute polymeric solutions.* Physical Review E, 2015. **92**(3): p. 033307.

12. Rouse, P.E., *A Theory of the Linear Viscoelastic Properties of Dilute Solutions of Coiling Polymers.* The Journal of Chemical Physics, 1953. **21**(7): p. 1272-1280.

13. Zimm, B.H., *Dynamics of Polymer Molecules in Dilute Solution: Viscoelasticity, Flow Birefringence and Dielectric Loss.* The Journal of Chemical Physics, 1956. **24**(2): p. 269-278.

14. Robertson, R.M. and D.E. Smith, *Direct Measurement of the Intermolecular Forces Confining a Single Molecule in an Entangled Polymer Solution.* Physical Review Letters, 2007. **99**(12): p. 126001.

15. Baig, C., V.G. Mavrantzas, and M. Kröger, *Flow Effects on Melt Structure and Entanglement Network of Linear Polymers: Results from a Nonequilibrium Molecular Dynamics Simulation Study of a Polyethylene Melt in Steady Shear.* Macromolecules, 2010. **43**(16): p. 6886-6902.

16. Nafar Sefiddashti, M.H., B.J. Edwards, and B. Khomami, *Individual chain dynamics of a polyethylene melt undergoing steady shear flow.* Journal of Rheology (1978-present), 2015. **59**(1): p. 119-153.

17. Doi, M. and S.F. Edwards, *Dynamics of concentrated polymer systems. Part 4.-Rheological properties.* Journal of the Chemical Society, Faraday Transactions 2: Molecular and Chemical Physics, 1979. **75**(0): p. 38-54.

18. Su, Y.Y. and B. Khomami, *Purely elastic interfacial instabilities in superposed flow of polymeric fluids.* Rheologica Acta, 1992. **31**(5): p. 413-420.

19. Su, Y.Y. and B. Khomami, *Interfacial stability of multilayer viscoelastic fluids in slit and converging channel die geometries.* Journal of Rheology (1978-present), 1992. **36**(2): p. 357-387.

20. Ganpule, H.K. and B. Khomami, *A theoretical investigation of interfacial instabilities in the three layer superposed channel flow of viscoelastic fluids.* Journal of Non-Newtonian Fluid Mechanics, 1998. **79**(2–3): p. 315-360.

21. Renardy, Y., *Stability of the interface in two-layer couette flow of upper convected maxwell liquids.* Journal of Non-Newtonian Fluid Mechanics, 1988. **28**(1): p. 99-115.

22. Bates, F.S. and G.H. Fredrickson, *Block Copolymers---Designer Soft Materials.* Physics Today, 1999. **52**(2): p. 32-38.

23. Urbas, A.M., et al., *Acoustic Excitations in a Self-Assembled Block Copolymer Photonic Crystal.* Physical Review Letters, 2003. **90**(10): p. 108302.

24. Park, M., et al., *Large area dense nanoscale patterning of arbitrary surfaces.* Applied Physics Letters, 2001. **79**(2): p. 257-259.

25. Cheng, J.Y., et al., *Formation of a Cobalt Magnetic Dot Array via Block Copolymer Lithography.* Advanced Materials, 2001. **13**(15): p. 1174-1178.

26. Thurn-Albrecht, T., et al., *Ultrahigh-Density Nanowire Arrays Grown in Self-Assembled Diblock Copolymer Templates.* Science, 2000. **290**(5499): p. 2126-2129.

27. Hashimoto, T., K. Tsutsumi, and Y. Funaki, *Nanoprocessing Based on Bicontinuous Microdomains of Block Copolymers: Nanochannels Coated with Metals.* Langmuir, 1997. **13**(26): p. 6869-6872.

28. Zhao, D., et al., *Triblock Copolymer Syntheses of Mesoporous Silica with Periodic 50 to 300 Angstrom Pores.* Science, 1998. **279**(5350): p. 548-552.

29. Cha, J.N., et al., *Biomimetic synthesis of ordered silica structures mediated by block copolypeptides.* Nature, 2000. **403**(6767): p. 289-292.

30. Lopes, W.A. and H.M. Jaeger, *Hierarchical self-assembly of metal nanostructures on diblock copolymer scaffolds.* Nature, 2001. **414**(6865): p. 735-738.

31. Bockstaller, M.R., et al., *Size-Selective Organization of Enthalpic Compatibilized Nanocrystals in Ternary Block Copolymer/Particle Mixtures.* Journal of the American Chemical Society, 2003. **125**(18): p. 5276-5277.

32. Maldovan, M., et al., *Photonic properties of bicontinuous cubic microphases.* Physical Review B, 2002. **65**(16): p. 165123.

33. Galatsis, K., et al., *Patterning and Templating for Nanoelectronics.* Advanced Materials, 2010. **22**(6): p. 769-778.

34. Park, S., et al., *Preparation of Metallic Line Patterns from Functional Block Copolymers.* Small, 2009. **5**(11): p. 1343-1348.

35. Zhao, Y., et al., *Small-molecule-directed nanoparticle assembly towards stimuli-responsive nanocomposites.* Nat Mater, 2009. **8**(12): p. 979-985.

36. Chuang, V.P., et al., *Templated Self-Assembly of Square Symmetry Arrays from an ABC Triblock Terpolymer.* Nano Letters, 2009. **9**(12): p. 4364-4369.

37. Son, J.G., et al., *Hierarchical Nanostructures by Sequential Self-Assembly of Styrene-Dimethylsiloxane Block Copolymers of Different Periods.* Advanced Materials, 2011. **23**(5): p. 634-639.

38. Ruiz, R., et al., *Density Multiplication and Improved Lithography by Directed Block Copolymer Assembly.* Science, 2008. **321**(5891): p. 936-939.

39. Liu, G., et al., *Integration of Density Multiplication in the Formation of Device-Oriented Structures by Directed Assembly of Block Copolymer–Homopolymer Blends.* Advanced Functional Materials, 2010. **20**(8): p. 1251-1257.

40. Liu, C.-C., et al., *Chemical Patterns for Directed Self-Assembly of Lamellae-Forming Block Copolymers with Density Multiplication of Features.* Macromolecules, 2013. **46**(4): p. 1415-1424.

41. Bita, I., et al., *Graphoepitaxy of Self-Assembled Block Copolymers on Two-Dimensional Periodic Patterned Templates.* Science, 2008. **321**(5891): p. 939-943.

42. Ross, C.A., et al. *Fabrication of patterned media for high density magnetic storage*. 1999. AVS.

43. Daoulas, K.C., et al., *Fabrication of Complex Three-Dimensional Nanostructures from Self-Assembling Block Copolymer Materials on Two-Dimensional Chemically Patterned Templates with Mismatched Symmetry.* Physical Review Letters, 2006. **96**(3): p. 036104.

44. Daoulas, K.C., et al., *Directed assembly of copolymer materials on patterned substrates: Balance of simple symmetries in complex structures.* Journal of Polymer Science Part B: Polymer Physics, 2006. **44**(18): p. 2589-2604.

45. Bang, J., et al., *Defect-Free Nanoporous Thin Films from ABC Triblock Copolymers.* Journal of the American Chemical Society, 2006. **128**(23): p. 7622-7629.

46. Ye, X., B.J. Edwards, and B. Khomami, *Elucidating the Formation of Block Copolymer Nanostructures on Patterned Surfaces: A Self-Consistent Field Theory Study.* Macromolecules, 2010. **43**(23): p. 9594-9597.

47. Ramírez-Hernández, A., et al., *Symmetric Diblock Copolymers Confined by Two Nanopatterned Surfaces.* Macromolecules, 2012. **45**(5): p. 2588-2596.

48. Ouk Kim, S., et al., *Epitaxial self-assembly of block copolymers on lithographically defined nanopatterned substrates.* Nature, 2003. **424**(6947): p. 411-414.

49. Luo, M. and T.H. Epps, *Directed Block Copolymer Thin Film Self-Assembly: Emerging Trends in Nanopattern Fabrication.* Macromolecules, 2013. **46**(19): p. 7567-7579.

50. Kim, M., et al., *Interplay of surface chemical composition and film thickness on graphoepitaxial assembly of asymmetric block copolymers.* Soft Matter, 2013. **9**(26): p. 6135-6141.

51. Ye, X., B.J. Edwards, and B. Khomami, *Morphology Tailoring of Thin Film Block Copolymers on Patterned Substrates.* Macromolecular Rapid Communications, 2012. **33**(5): p. 392-395.

52. McLeish, T.C.B., *Tube theory of entangled polymer dynamics.* Advances in Physics, 2002. **51**(6): p. 1379-1527.

53. Dambal, A., A. Kushwaha, and E.S.G. Shaqfeh, *Slip-Link Simulations of Entangled, Finitely Extensible, Wormlike Chains in Shear Flow.* Macromolecules, 2009. **42**(18): p. 7168-7183.

54. Kushwaha, A. and E.S.G. Shaqfeh, *Slip-link simulations of entangled polymers in planar extensional flow: Disentanglement modified extensional thinning.* Journal of Rheology (1978-present), 2011. **55**(3): p. 463-483.

55. Hoogerbrugge, P.J. and J.M.V.A. Koelman, *Simulating Microscopic Hydrodynamic Phenomena with Dissipative Particle Dynamics.* EPL (Europhysics Letters), 1992. **19**(3): p. 155.

56. Español, P. and P. Warren, *Statistical Mechanics of Dissipative Particle Dynamics.* EPL (Europhysics Letters), 1995. **30**(4): p. 191.

57. Verlet, L., *Computer "Experiments" on Classical Fluids. I. Thermodynamical Properties of Lennard-Jones Molecules.* Physical Review, 1967. **159**(1): p. 98-103.

58. Sirk, T.W., et al., *An enhanced entangled polymer model for dissipative particle dynamics.* The Journal of Chemical Physics, 2012. **136**(13): p. -.

59. Kumar, S. and R.G. Larson, *Brownian dynamics simulations of flexible polymers with spring–spring repulsions.* The Journal of Chemical Physics, 2001. **114**(15): p. 6937-6941.

60. Padding, J.T. and W.J. Briels, *Uncrossability constraints in mesoscopic polymer melt simulations: Non-Rouse behavior of C120H242.* The Journal of Chemical Physics, 2001. **115**(6): p. 2846-2859.

61. Nikunen, P., I. Vattulainen, and M. Karttunen, *Reptational dynamics in dissipative particle dynamics simulations of polymer melts.* Physical Review E, 2007. **75**(3): p. 036713.

62. Groot, R.D. and P.B. Warren, *Dissipative particle dynamics: Bridging the gap between atomistic and mesoscopic simulation.* The Journal of Chemical Physics, 1997. **107**(11): p. 4423-4435.

63. Shanbhag, S. and M. Kröger, *Primitive Path Networks Generated by Annealing and Geometrical Methods: Insights into Differences.* Macromolecules, 2007. **40**(8): p. 2897-2903.

64. Kröger, M., *Shortest multiple disconnected path for the analysis of entanglements in two- and three-dimensional polymeric systems.* Computer Physics Communications, 2005. **168**(3): p. 209-232.

65. Karayiannis, N.C. and M. Kröger, *Combined Molecular Algorithms for the Generation, Equilibration and Topological Analysis of Entangled Polymers: Methodology and Performance.* International Journal of Molecular Sciences, 2009. **10**(11): p. 5054-5089.

66. Thompson, A.P., S.J. Plimpton, and W. Mattson, *General formulation of pressure and stress tensor for arbitrary many-body interaction potentials under periodic boundary conditions.* The Journal of Chemical Physics, 2009. **131**(15): p. 154107.

67. Spenley, N.A., *Scaling laws for polymers in dissipative particle dynamics.* EPL (Europhysics Letters), 2000. **49**(4): p. 534.

68. Kremer, K. and G.S. Grest, *Dynamics of entangled linear polymer melts: A molecular-dynamics simulation.* The Journal of Chemical Physics, 1990. **92**(8): p. 5057-5086.

69. Doi, M., *Explanation for the 3.4 power law of viscosity of polymeric liquids on the basis of the tube model.* Journal of Polymer Science: Polymer Letters Edition, 1981. **19**(5): p. 265-273.

70. Colby, R.H., L.J. Fetters, and W.W. Graessley, *The melt viscosity-molecular weight relationship for linear polymers.* Macromolecules, 1987. **20**(9): p. 2226-2237.

71. Milner, S.T. and T.C.B. McLeish, *Reptation and Contour-Length Fluctuations in Melts of Linear Polymers.* Physical Review Letters, 1998. **81**(3): p. 725-728.

72. Pearson, D.S., et al., *Viscosity and self-diffusion coefficient of linear polyethylene.* Macromolecules, 1987. **20**(5): p. 1133-1141.

73. Pütz, M., K. Kremer, and G.S. Grest, *What is the entanglement length in a polymer melt?* EPL (Europhysics Letters), 2000. **49**(6): p. 735.

74. Padding, J.T. and W.J. Briels, *Time and length scales of polymer melts studied by coarse-grained molecular dynamics simulations.* The Journal of Chemical Physics, 2002. **117**(2): p. 925-943.

75. Larson, R.G., *The Structure and Rheology of Complex Fluids*. 1999: OUP USA.

76. Nafar Sefiddashti, M.H., B.J. Edwards, and B. Khomami, *Individual chain dynamics of a polyethylene melt undergoing steady shear flow.* Journal of Rheology, 2015. **59**(1): p. 119-153.

77. Everaers, R., *Topological versus rheological entanglement length in primitive-path analysis protocols, tube models, and slip-link models.* Physical Review E, 2012. **86**(2): p. 022801.

78. Mead, D.W., R.G. Larson, and M. Doi, *A Molecular Theory for Fast Flows of Entangled Polymers.* Macromolecules, 1998. **31**(22): p. 7895-7914.

79. Marrucci, G., *Dynamics of entanglements: A nonlinear model consistent with the Cox-Merz rule.* Journal of Non-Newtonian Fluid Mechanics, 1996. **62**(2–3): p. 279-289.

80. Ianniruberto, G. and G. Marrucci, *On compatibility of the Cox-Merz rule with the model of Doi and Edwards.* Journal of Non-Newtonian Fluid Mechanics, 1996. **65**(2–3): p. 241-246.

81. Marrucci, G. and G. Ianniruberto, *Effect of flow on topological interactions in polymers.* Macromolecular Symposia, 1997. **117**(1): p. 233-240.

82. Ganpule, H.K. and B. Khomami, *An investigation of interfacial instabilities in the superposed channel flow of viscoelastic fluids1.* Journal of Non-Newtonian Fluid Mechanics, 1999. **81**(1–2): p. 27-69.

83. Cates, M.E., *Nonlinear viscoelasticity of wormlike micelles (and other reversibly breakable polymers).* The Journal of Physical Chemistry, 1990. **94**(1): p. 371-375.

84. Cates, M.E. and S.M. Fielding, *Rheology of giant micelles.* Advances in Physics, 2006. **55**(7-8): p. 799-879.

85. Spenley, N.A., M.E. Cates, and T.C.B. McLeish, *Nonlinear rheology of wormlike micelles.* Physical Review Letters, 1993. **71**(6): p. 939-942.

86. Rehage, H. and H. Hoffmann, *Rheological properties of viscoelastic surfactant systems.* The Journal of Physical Chemistry, 1988. **92**(16): p. 4712-4719.

87. Shikata, T., et al., *Nonlinear viscoelastic behavior of aqueous detergent solutions.* Journal of Non-Newtonian Fluid Mechanics, 1988. **28**(2): p. 171-182.

88. Osaki, K. and M. Kurata, *Experimental Appraisal of the Doi-Edwards Theory for Polymer Rheology Based on the Data for Polystyrene Solutions.* Macromolecules, 1980. **13**(3): p. 671-676.

89. Vrentas, C.M. and W.W. Graessley, *Study of Shear Stress Relaxation in Well-Characterized Polymer Liquids.* Journal of Rheology, 1982. **26**(4): p. 359-371.

90. Marrucci, G. and N. Grizzuti, *The Free Energy Function of the Doi-Edwards Theory: Analysis of the Instabilities in Stress Relaxation.* Journal of Rheology, 1983. **27**(5): p. 433-450.

91. Morrison, F.A. and R.G. Larson, *A study of shear-stress relaxation anomalies in binary mixtures of monodisperse polystyrenes.* Journal of Polymer Science Part B: Polymer Physics, 1992. **30**(9): p. 943-950.

92. Venerus, D.C., *A critical evaluation of step strain flows of entangled linear polymer liquids.* Journal of Rheology, 2005. **49**(1): p. 277-295.

93. Venerus, D.C. and R. Nair, *Stress relaxation dynamics of an entangled polystyrene solution following step strain flow.* Journal of Rheology, 2006. **50**(1): p. 59-75.

94. Tapadia, P. and S.-Q. Wang, *Direct Visualization of Continuous Simple Shear in Non-Newtonian Polymeric Fluids.* Physical Review Letters, 2006. **96**(1): p. 016001.

95. Wang, S.-Q., et al., *Nonquiescent Relaxation in Entangled Polymer Liquids after Step Shear.* Physical Review Letters, 2006. **97**(18): p. 187801.

96. Hu, Y.T., et al., *Is the constitutive relation for entangled polymers monotonic?* Journal of Rheology, 2007. **51**(2): p. 275-295.

97. Boukany, P.E., Y.T. Hu, and S.-Q. Wang, *Observations of Wall Slip and Shear Banding in an Entangled DNA Solution.* Macromolecules, 2008. **41**(7): p. 2644-2650.

98. Ravindranath, S. and S.-Q. Wang, *Large amplitude oscillatory shear behavior of entangled polymer solutions: Particle tracking velocimetric investigation.* Journal of Rheology, 2008. **52**(2): p. 341-358.

99. Ravindranath, S., et al., *Banding in Simple Steady Shear of Entangled Polymer Solutions.* Macromolecules, 2008. **41**(7): p. 2663-2670.

100. Boukany, P.E. and S.-Q. Wang, *Exploring the transition from wall slip to bulk shearing banding in well-entangled DNA solutions.* Soft Matter, 2009. **5**(4): p. 780-789.

101. Boukany, P.E., S.-Q. Wang, and X. Wang, *Step Shear of Entangled Linear Polymer Melts: New Experimental Evidence for Elastic Yielding.* Macromolecules, 2009. **42**(16): p. 6261-6269.

102. Boukany, P.E. and S.-Q. Wang, *Shear banding or not in entangled DNA solutions depending on the level of entanglement.* Journal of Rheology, 2009. **53**(1): p. 73-83.

103. Tapadia, P., S. Ravindranath, and S.-Q. Wang, *Banding in Entangled Polymer Fluids under Oscillatory Shearing.* Physical Review Letters, 2006. **96**(19): p. 196001.

104. Ravindranath, S. and S.-Q. Wang, *What Are the Origins of Stress Relaxation Behaviors in Step Shear of Entangled Polymer Solutions?* Macromolecules, 2007. **40**(22): p. 8031-8039.

105. Sui, C. and G. McKenna, *Instability of entangled polymers in cone and plate rheometry.* Rheologica Acta, 2007. **46**(6): p. 877-888.

106. Adams, J.M., S.M. Fielding, and P.D. Olmsted, *Transient shear banding in entangled polymers: A study using the Rolie-Poly model.* Journal of Rheology, 2011. **55**(5): p. 1007-1032.

107. Adams, J.M. and P.D. Olmsted, *Nonmonotonic Models are Not Necessary to Obtain Shear Banding Phenomena in Entangled Polymer Solutions.* Physical Review Letters, 2009. **102**(6): p. 067801.

108. Fielding, S.M. and P.D. Olmsted, *Kinetics of the shear banding instability in startup flows.* Physical Review E, 2003. **68**(3): p. 036313.

109. Olmsted, P., *Perspectives on shear banding in complex fluids.* Rheologica Acta, 2008. **47**(3): p. 283-300.

110. Olmsted, P.D., O. Radulescu, and C.-Y.D. Lu, *Johnson–Segalman model with a diffusion term in cylindrical Couette flow.* Journal of Rheology, 2000. **44**(2): p. 257-275.

111. Cromer, M., et al., *Shear banding in polymer solutions.* Physics of Fluids, 2013. **25**(5): p. 051703.

112. Cao, J. and A.E. Likhtman, *Shear Banding in Molecular Dynamics of Polymer Melts.* Physical Review Letters, 2012. **108**(2): p. 028302.

113. Mohagheghi, M. and B. Khomami, *Molecular Processes Leading to Shear Banding in Well Entangled Polymeric Melts.* ACS Macro Letters, 2015. **4**(7): p. 684-688.

114. Marrucci, G. and N. Grizzuti, *The Free Energy Function of the Doi-Edwards Theory: Analysis of the Instabilities in Stress Relaxation.* Journal of Rheology (1978-present), 1983. **27**(5): p. 433-450.

115. Boukany, P.E. and S.-Q. Wang, *Shear Banding or Not in Entangled DNA Solutions.* Macromolecules, 2010. **43**(17): p. 6950-6952.

116. Cheng, S. and S.-Q. Wang, *Is shear banding a metastable property of well-entangled polymer solutions?* Journal of Rheology, 2012. **56**(6): p. 1413-1428.

117. Su, Y.Y. and B. Khomami, *Interfacial stability of multilayer viscoelastic fluids in slit and converging channel die geometries.* Journal of Rheology, 1992. **36**(2): p. 357-387.

118. Matsen, M.W., *Thin films of block copolymer.* The Journal of Chemical Physics, 1997. **106**(18): p. 7781-7791.

119. Turner, M.S., *Equilibrium properties of a diblock copolymer lamellar phase confined between flat plates.* Physical Review Letters, 1992. **69**(12): p. 1788-1791.

120. Pereira, G.G. and D.R.M. Williams, *Diblock Copolymer Thin Films on Heterogeneous Striped Surfaces: Commensurate, Incommensurate and Inverted Lamellae.* Physical Review Letters, 1998. **80**(13): p. 2849-2852.

121. Pereira, G.G., *Cylindrical phase of block copolymers: Stability of circular configuration to elliptical distortions and thin film morphologies.* Physical Review E, 2001. **63**(6): p. 061809.

122. Wang, Q., P.F. Nealey, and J.J. de Pablo, *Monte Carlo Simulations of Asymmetric Diblock Copolymer Thin Films Confined between Two Homogeneous Surfaces.* Macromolecules, 2001. **34**(10): p. 3458-3470.

123. Suh, K.Y., Y.S. Kim, and H.H. Lee, *Parallel and vertical morphologies in block copolymers of cylindrical domain.* The Journal of Chemical Physics, 1998. **108**(3): p. 1253-1256.

124. Pickett, G.T. and A.C. Balazs, *Equilibrium Orientation of Confined Diblock Copolymer Films.* Macromolecules, 1997. **30**(10): p. 3097-3103.

125. Pickett, G.T. and A.C. Balazs, *Equilibrium behavior of confined triblock copolymer films.* Macromolecular Theory and Simulations, 1998. **7**(2): p. 249-255.

126. Horvat, A., et al., *Phase behavior in thin films of cylinder-forming ABA block copolymers: Mesoscale modeling.* The Journal of Chemical Physics, 2004. **120**(2): p. 1117-1126.

127. Ludwigs, S., et al., *Phase Behavior of ABC Triblock Terpolymers in Thin Films: Mesoscale Simulations.* Macromolecules, 2005. **38**(5): p. 1859-1867.

128. Chen, H.-Y. and G.H. Fredrickson, *Morphologies of ABC triblock copolymer thin films.* The Journal of Chemical Physics, 2002. **116**(3): p. 1137-1146.

129. Drolet, F. and G.H. Fredrickson, *Combinatorial Screening of Complex Block Copolymer Assembly with Self-Consistent Field Theory.* Physical Review Letters, 1999. **83**(21): p. 4317-4320.

130. Drolet, F. and G.H. Fredrickson, *Optimizing Chain Bridging in Complex Block Copolymers.* Macromolecules, 2001. **34**(15): p. 5317-5324.

131. Kumar, R., et al., *Morphologies of ABC Triblock Terpolymer Melts Containing Poly(Cyclohexadiene): Effects of Conformational Asymmetry.* Langmuir, 2012. **29**(6): p. 1995-2006.

132. Nagpal, U., et al., *Morphologies of Linear Triblock Copolymers from Monte Carlo Simulations.* Macromolecules, 2011. **44**(13): p. 5490-5497.

133. Tang, P., et al., *Morphology and Phase Diagram of Complex Block Copolymers: ABC Star Triblock Copolymers.* The Journal of Physical Chemistry B, 2004. **108**(24): p. 8434-8438.

134. Tang, P., et al., *Morphology and phase diagram of complex block copolymers: ABC linear triblock copolymers.* Physical Review E, 2004. **69**(3): p. 031803.

135. Sun, M., et al., *Morphology and phase diagram of ABC linear triblock copolymers: Parallel real-space self-consistent-field-theory simulation.* Physical Review E, 2008. **77**(1): p. 016701.

136. Mogi, Y., et al., *Preparation and morphology of triblock copolymers of the ABC type.* Macromolecules, 1992. **25**(20): p. 5408-5411.

137. Stadler, R., et al., *Morphology and Thermodynamics of Symmetric Poly(A-block-B-block-C) Triblock Copolymers.* Macromolecules, 1995. **28**(9): p. 3080-3097.

138. Matsen, M.W., *Architectural Effect on the Surface Tension of an ABA Triblock Copolymer Melt.* Macromolecules, 2009. **43**(3): p. 1671-1674.

139. Sohn, B.H. and S.H. Yun, *Perpendicular lamellae induced at the interface of neutral self-assembled monolayers in thin diblock copolymer films.* Polymer, 2002. **43**(8): p. 2507-2512.

140. Sivaniah, E., et al., *Observation of Perpendicular Orientation in Symmetric Diblock Copolymer Thin Films on Rough Substrates.* Macromolecules, 2003. **36**(16): p. 5894-5896.

141. Müller-Buschbaum, P., et al., *Surface versus Confinement Induced Morphology Transition in Triblock Copolymer Films: A Grazing Incidence Small Angle Neutron Scattering Investigation.* Langmuir, 2006. **22**(22): p. 9295-9303.

142. Elbs, H., et al., *Microdomain Morphology of Thin ABC Triblock Copolymer Films.* Macromolecules, 1999. **32**(4): p. 1204-1211.

Vita

Mouge Mohagheghi was born in Tehran, Iran, in 1987. In 2009, she received her B.Sc. in chemical engineering from Sharif University of Technology, Tehran, Iran, Magna Cum Laude. Later, she attended the University of Tennessee, Department of Chemical and Biomolecular Engineering and joined Dr. Khomami's research group (MRAIL) in 2010 to pursue her doctoral degree in chemical engineering. Her doctoral research has mainly focused on the design and development of computational models and simulations to elucidate the underlying physics and mechanism of flow-microstructure coupling in entangled polymeric melts. Her doctoral research work has resulted in five published and submitted papers. She also received her M.Sc. in chemical engineering and a graduate minor in computational science in 2013. Mouge will continue her professional career as the modeling and simulation research engineer at Procter & Gamble research and development cooperation.